IMAGERY

VISIBLE/INFRARED IMAGER/RADIOMETER SUITE ALGORITHM THEORETICAL BASIS DOCUMENT

Version 3: May 2000

Ken Jensen
Duane Apling
Igor Appel
Keith Hutchison
Richard Julian
North Larsen
Wenli Yang

RAYTHEON SYSTEMS COMPANY
Information Technology and Scientific Services
4400 Forbes Boulevard
Lanham, MD 20706

SBRS Document #: Y2466

EDRs: IMAGERY

Doc No: Y2466

Version: 3

Revision: 0

	Function	Name	Signature	Date
Prepared by	EDR Developer	K. JENSEN		
Approved by	Relevant IPT Lead	K. JENSEN		
Approved by	Chief Scientist	P. ARDANUY		
Released by	Program Manager	H. BLOOM		

TABLE OF CONTENTS

Raytheon

Raytheon

LIST OF FIGURES

Raytheon

LIST OF TABLES

Raytheon

GLOSSARY OF ACRONYMS

AFWA	Air Force Weather Agency
AMSR	Advanced Microwave Scanning Radiometer
ARM	Arctic Radiation Measurements
ATBD	Algorithm Theoretical Basis Document
AVHRR	Advanced Very High Resolution Radiometer
BRDF	Bidirectional Reflectance Distribution Function
CCD	Charge Coupled Device
CGTA	Cloud Ground Truth Analysis
CI	Cirrus
CMIS	Conical Scanning Microwave Imager/Sounder
CNC	Cloud-No Cloud
CRT	Cathode Ray Tube
CU	Cumulus
DMSP	Defense Meteorological Satellite Program
DNB	Daytime Nighttime Band
DOD	Department of Defense
DTED	Digital Terrain Elevation Data
DV	Daytime Visible
EDR	Environmental Data Record
FIRE-ACE	First ISCCP Regional Experiment – Arctic Cloud Experiment
FIVLYR	Five-Layer
GOES	Geostationary Operational Environmental Satellite
HRCP	High-Resolution Cloud Prognosis
HSR	Horizontal Spatial Resolution
IDPS	Interface Data Processor Segment
IR	Infrared
ISCCP	International Satellite Cloud Climatology Project
LLV	Low Light Level Visible
LUT	Look Up Table
LWIR	Long-Wave Infrared
MAS	MODIS Airborne Simulator
MESMA	Multiple Endmember Spectral Mixture Analysis
MODIS	Moderate Resolution Imaging Spectroradiometer
MODTRAN	Moderate Resolution Model for LOWTRAN7
MTF	Modulation Transfer Function
MWIR	Mid-Wave Infrared

NASA	National Aeronautics and Space Administration
NOAA	National Oceanographic and Atmospheric Administration
NPOESS	National Polar-Orbiting Operational Environmental Satellite System
NPP	NPOESS Preparatory Program
NV	Nighttime Visible Imagery
QC	Quality Control
RDR	Raw Data Record
RGB	Red-Green-Blue
RMS	Root Mean Square
RMSE	Root Mean Square Error
RTNEPH	Real Time NEPH Analysis
SDHS	Satellite Data Handling System
SDR	Sensor Data Record
SERCAA	Support of Environmental Requirements for Cloud Analysis and Archive
SHEBA	Surface Heat Budget of the Arctic Ocean
SMA	Spectral Mixture Analysis
SNR	Signal-to-Noise Ratio
SOC	Satellite Operations Command
SRD	Sensor Requirements Document
ST	Stratus
TBD	To Be Determined
TBR	To Be Reviewed
TDI	Time Delay and Integration
TIROS	Television Infrared Observation Satellite
TOA	Top of Atmosphere
TRONEW	New Tropical Model
VIIRS	Visible/Infrared Imager/Radiometer Suite
VIR	Visible-Infrared
VMCD	VIIRS Manually-Generated Cloud Data

Raytheon

ABSTRACT

This Imagery Algorithm Theoretical Basis Document describes the background, theory, and analysis of the algorithmic process required to create Imagery Environmental Data Records (EDRs) from the sensor Raw Data Records (RDRs) of the Visible/Infrared Imager/Radiometer Suite (VIIRS). The process has been developed to satisfy the requirements of the VIIRS Sensor Requirements Document (SRD), Version Two, Revision a. This document is version 3 of the Imagery ATBD. It is intended to completely supersede previous versions.

The document covers all VIIRS imagery processing. In particular, it describes algorithms for producing four imagery products: the Imagery Sensor Data Records (SDRs), the Near Constant Contrast (NCC) Visible Imagery, Manually Generated Cloud Data, and Sea Ice Data.

Four imagery bands are specified. The Daytime/Nightime Visible Band (DNB), Daytime Visible Band (DV), and Long-Wave Infrared Band (LWIR) are explicitly required. The Mid-Wave Infrared Band (MWIR) had been added as a result of flowdown of the Imagery Application-Related requirements. For each spectral band for which imagery is provided, the Imagery EDR includes the following two data products, both generated by ground processing of VIIRS data:

(a) a two-dimensional array of locally averaged absolute in-band radiances at the top of the atmosphere, measured in the direction of the viewing instrument, and

(b) the corresponding array of equivalent blackbody temperatures (EBBT) if the band is primarily emissive, or the corresponding array of top-of-the-atmosphere (TOA) reflectances if the band is primarily reflective during daytime.

The VIIRS Imagery EDR benefits from true multi-spectral capability and compatibility with OLS heritage. The radiometric performance of the bands exceeds the specification for Measurement Uncertainty with margins that allow the performance of the Application-Related Products to meet or approach objective requirements.

Imagery SDRs are computed from the RDRs, as part of the Build-SDR module, which applies geo-location, gridding, and calibration to the RDRs. The functionality of the Build-SDR module will allow it to produce SDRs which fully meet the explicit imagery requirements. These SDRs are therefore the basic Imagery EDR product. All Imagery SDR products shall be calibrated, geolocated, corrected for Earth curvature and satellite motion, and reported for a set of earth locations forming an approximately rectangular lattice. The lattice spacing will be 742 +/- 5% meters for the DNB, and approximately equivalent to the HSR for the other imagery bands.

DNB data is taken by a sensitive, very-wide-dynamic range Charge-Coupled Device (CCD) detector in the main VIIRS Sensor. To encompass the extreme radiometric dynamic range of day and night scenes, the DNB CCD includes four regions of light-sensitive photosites with three different sensitivities. The three regions are designed so that before a more sensitive region saturates, the next less sensitive region will have received a signal sufficient to produce an acceptable SNR. Analog signals from all three regions are converted into digital form and processed digitally to select the signal from the region offering the best SNR for each pixel. The

CCD design allows any number of subpixel elements to be aggregated into single pixels as they are read from the CCD. In the VIIRS sensor this capability will be used to generate pixels with near-rectangular sample spacing on the ground. At nadir, SNR performance of the DNB over the specified measurement range (4.E-9 – 3.E-2 W/cm^2/sr) is 30 TO 1000. SNR greater than 3 is achieved at a radiance as low as 3.2E-10 W/cm^2/sr. At edge of scan, SNR performance of the DNB over the specified measurement range (4.E-9 – 3.E-2 W/cm^2/sr) is 7 to 250. SNR greater than 3 is achieved at a radiance as low as 1.8E-9 W/cm^2/sr. SNR greater than 10 is achieved at the minimum radiance for almost the entire scan.

NCC Visible Imagery is derived from the broad day/night band near the terminator region. Due to the significant change in solar irradiance across the terminator, a three stage CCD sensor is designed to record the radiance in this region. The individuals detectors in the three portions of the CCD are used to record day time, day/night crossing time, and night time radiance, respectively. The SDR for this band consists of a single set of data which contains all three stages in all illumination conditions. Due to the switch of gain across the day/night transition aera, the digital numbers present artificial boundaries. The NCC algorithm takes the SDR and converts the DN values back to radiance based on coefficients for each stage. The radiance values cover a very large dynamic range, from 4E-9 to 3E-2 Wcm-2sr-1. The algorithm removes path radiance and normalizes the path-removed radiance values according to an empirical function between the TOA radiance and solar/lunar angles for a reference surface with constant albedo.

Manual cloud analysis is based upon the contrast, measured in brightness temperatures or albedo, between the cloud and the surrounding cloud-free background. In infrared imagery, cloud detection is enhanced not only by temperature contrasts between the features but also by observing the features in spectral bands where their emissivity contrasts exist. In visible and near-infrared imagery, cloud detection relies on contrasts in the reflectivities of the features while at mid-infrared wavelengths, e.g. 3-5 microns, both temperature and reflected solar energy can be exploited in the manual cloud analysis process. Image enhancement techniques such as histogram equalization and thresholding enable the analyst to delineate individual features. False-colored compositing of multispectral images facilitates manual interpretation of the clouds and background features by assigning colors to those pixels with different multispectral responses. Using these tools, the analyst can systematically and quickly identify and classify the various clouds in the imagery.

The VIIRS SRD requires that the content and quality of the Imagery EDR be adequate to allow for specified requirements on sea ice edge location and sea ice concentration to be met. Sea ice data may be generated interactively by a trained analyst viewing unprocessed or processed imagery at a computer workstation, or automatically via an algorithm. The revised requirements for sea ice data could not be met if sea ice data are generated manually by an ice analyst. Our approach can be used to develop operational algorithms to retrieve sea ice data automatically on a global basis. This capability will be of great value to operational ice centers in the NPOESS era.

The algorithms of ice concentration and ice edge location retrieval have changed since the version 2 ATBD, due to new requirements.

Raytheon

Ice concentration is defined as the fraction of a given area of sea water covered by ice. It is typically derived from imagery and reported on ice charts for areas between contours generated by an analyst. But for the purpose of verifying the measurement uncertainty requirement, ice concentration is reported as a gridded product for areas of size limited by the Horizontal Cell Size requirement and separation limited by the Horizontal Reporting Interval requirement. We retrieve ice concentration operationally from an automated algorithm. The algorithm includes the derivation of ice fraction for imagery pixels, using tie point analysis of ice surface temperature and/or surface reflectances. Operational capability is achieved by the use of local search windows to derive ice and water tie points. Ice concentration is retrieved as a gridded product at imagery resolution with measurement uncertainty better than 0.1 in most cases.

The sea ice edge is defined as the boundary between ice-covered sea water (ice concentration > 0.1) and sea water not covered by ice (ice concentration ≤ 0.1). An automated algorithm produces ice edge location as a contour on a map (an ice edge image, or "isoline") and also as a set of latitude/longitude coordinates. The coordinates are determined at subpixel resolution by interpolation of the ice concentration map in the vicinity of the ice edge isoline. The ice edge is located in most cases with a measurement uncertainty of less than 0.3 km at nadir. This estimate of algorithm quality performance corresponds to the case of compacted ice edge. The ice edge location and ice concentration retrieved by our automated algorithms will be archived as a part of the VIIRS Imagery EDR product, for use by analysts at national ice centers.

Optimized parameters of a search window and band weight reduce tie point errors and provide a seamless day/night transition for the Imagery/Sea Ice products.

1.0   INTRODUCTION

1.1   PURPOSE

This Visible/Infrared Imager/Radiometer Suite (VIIRS) Imagery Algorithm Theoretical Basis Document (ATBD) describes the processing steps required to transform all VIIRS Imagery Raw Data Records (RDR) generated by the VIIRS sensor into Imagery Environmental Data Records (EDRs).

The NPOESS VIIRS SRD identifies three classes of imagery:

  (a)   explicit imagery requirements, which includes at least one daytime visible, one nighttime visible, and one infrared imagery channel

  (b)   applications-related imagery requirements, which are imagery channels needed to satisfy threshold requirements for Manually-Generated Cloud Data and Sea Ice Data, and

  (c)   derived imagery requirements, which are contractor-derived and based on requirements for other EDRs supported by the imagery.

The Imagery algorithm consists of four major processing functions:

(1)   generation of the imagery SDRs.

(2)   creation of Near Constant Contrast (NCC) visible imagery from the daytime/nighttime visible imagery SDR.

(3)   manual generation of cloud data products

(4)   generation of sea ice data by an automated algorithm.

1.2   SCOPE

All aspects of VIIRS imagery processing are described in this ATBD, including the explicit Imagery SDRs, the NCC visible imagery, and the two classes of application-related products (ARPs) — manually generated cloud data, and sea ice data.

This section of the ATBD introduces the Imagery algorithm. Section 2 provides an overview of the Imagery EDR requirement, specifications, and retrieval strategy. Section 3 describes the algorithm's functions in detail, including the theoretical basis, mathematical description, and performance analysis. Section 4 states the assumption and limitations on which the algorithm is based, and Section 5 provides references for the publications cited in this document.

Our specification and performance for the VIIRS Imagery EDR and Applications Related Requirements based on Imagery are achieved with the 9 EDR products listed in Table 1.

Table 1. Imagery EDR Products

EDR Product	VIIRS Band(s)	Resolution
* Daytime Visible (DV), TOA Radiance, TOA Reflectance	0.645 microns	0.4 km (at nadir), 0.8 km (at 3000 km swath)
* Daytime/Nighttime Visible (DNB), TOA Radiance, TOA Reflectance	0.5 – 0.9 microns	0.74 km **
* NCC Visible Imagery	0.5 – 0.9 microns	0.74 km **
* Mid Wave IR (MWIR), TOA Radiance, Equivalent Blackbody Temperature	3.74 microns	DV Resolution
* Long Wave IR (LWIR), TOA Radiance, Equivalent Blackbody Temperature	11.45 microns	DV Resolution
*** Manually Generated Cloud Cover	DV, MWIR, LWIR	1.2 km (at nadir), 2.4 km (at 3000 km swath)
*** Manually Generated Cloud Type	DV, MWIR, LWIR	1.2 km (at nadir), 2.4 km (at 3000 km swath)
*** Sea Ice Concentration	DV, LWIR	DV Resolution
*** Sea Ice Edge Location	DV, LWIR	Sub-DV Resolution

*   Explicit Imagery EDR Requirement

**   Constant to within 5% in both directions within a swath

*** Imagery Application-Related Requirement

1.3   VIIRS DOCUMENTS

This document contains references to other Raytheon VIIRS documents, designated by a document number, which is given in italicized brackets. The VIIRS documents cited in this document are :

[SS 154640-001]   VIIRS System Specification

[PS 154640-101]   VIIRS Sensor Specification

[TP 154640-001]   VIIRS System Verification and Validation Plan Document

[Y2477]   Snow/Ice Module Software Architecture Document

[Y2478]   Build-RDR Module Software Architecture Document

[Y2479]   Build-SDR Module Software Architecture Document

[Y3261]   RDR to SDR Conversion ATBD

Raytheon

[Y2401]   Snow Cover/Depth ATBD

[Y2404]   Fresh Water Ice ATBD

[Y2405]   Ice Surface Temperature ATBD

[Y2409]   Sea Ice Age / Ice Edge Motion ATBD

[Y2411]   Atmospheric Correction over Land ATBD

[Y2412]   Cloud Mask ATBD

[Y4963]   VIIRS Imagery TIM, March 8, 2000

1.4 REVISIONS

This is the third version of this document, dated May 2000. The first two versions were developed in response to VIIRS Sensor Requirements Document (SRD), revision 1, dated August 3, 1998. The first version was dated October 1998. The second version was dated June 1999. The third version has been developed in response to VIIRS Sensor Requirements Document (SRD), Version 2, Revision a, dated 04 November 1999.

Changes since version 2 are largely in response to revisions in the new SRD. They include:

- Modification of the process flow

- Additional development of an algorithm for producing the NCC imagery

- Performance summary for meeting manual cloud detection thresholds and objectives

- Identification of cloud type classifications that meet system level thresholds and objectives

- Plans for developing a VIIRS users guide for manual cloud identification and typing

- Development of scene-specific tie point analysis of reflectance and/or surface temperature for the automated sea ice concentration algorithm

- Development of an automated algorithm to retrieve ice edge location

- Reporting of ice edge location as an ice edge map and a set of latitude/longitude coordinates

- Additional sea ice test results, from an expanded test data set

- A revised sea ice specification, with supporting error analysis and error budget

2.0   EXPERIMENT OVERVIEW

2.1   EDR DEFINITION

Imagery requirements fall into three classes:

(a) explicit requirements on the EDR content, quality, reporting frequency, and timeliness.

(b) Requirements to be derived based on specific applications utilizing the imagery EDR, such as manual generation of cloud and sea ice data.

(c) Requirements to be derived from requirements for other EDRs supported by the imagery.

2.2   EXPLICIT IMAGERY REQUIREMENTS

For each spectral band for which imagery is provided, the Imagery EDR includes the following two data products, both generated by ground processing of VIIRS data:

1. a two-dimensional array of locally averaged absolute in-band radiances at the top of the atmosphere, measured in the direction of the viewing instrument, and

2. the corresponding array of equivalent blackbody temperatures (EBBT) if the band is primarily emissive, or the corresponding array of top-of-the-atmosphere (TOA) reflectances if the band is primarily reflective during daytime.

The radiances, EBBTs, and reflectances are reported for a set of earth locations forming an approximately rectangular lattice, with the spacing between locations constrained by the Horizontal Reporting Interval (HRI) requirement. The form of the spatial weighting function that determines the local averaging of the absolute TOA radiance is constrained by the Horizontal Spatial Resolution (HSR) requirement. The number of spectral bands, band limit values, measurement ranges, and measurement uncertainty (or accuracy and precision) requirements are to be derived based on the application-related requirements and on the requirements of other EDRs supported by the imagery.

The Imagery EDR must satisfy the following additional requirements:

1) Every spectral band deemed to be essential to meet the application-related threshold requirements shall meet all of the explicit imagery requirements. Spectral bands used to improve performance toward objective levels need not meet the explicit imagery requirements.

2) At a minimum, at least one daytime visible, one daytime/nighttime visible, and one IR channel shall meet the explicit imagery requirements.

3) Every spectral band essential to meeting the application-related threshold requirements shall have the same nominal pixel HSR and HIS design values, or better than nominal values by an integral factor, and pixels in any two of these bands shall be co-registered to within 20% of the nominal pixel HSR. This requirement does not apply to the daytime/nighttime visible band.

The explicit requirements and specifications are summarized in Table 2.

Table 2. Explicit Requirements for the VIIRS Imagery EDR

Para. No	Parameter	Thresholds	Objectives	Specification Value
	a. Horizontal Spatial Resolution (HSR)			
V40.2.3.1-2	1. At nadir	0.4 km	(TBD)	0.4 km
V40.2.3.1-3	2. Worst case	0.8 km	0.1 km	0.8 km
V40.2.3.1-6	5. Daytime/Nighttime Visible, worst case	2.6 km	0.65 km	0.8 km
V40.2.3.1-7	b. Horizontal Reporting Interval	Derived (gapless or near gapless coverage required)	Derived (gapless or near gapless coverage required)	Imagery HSR * (Approximately rectangular lattice)
	c. Horizontal Coverage	Global	Global	Global
	d. Measurement Range			
V40.2.3.1-11	1. Daytime/Nighttime visible	4E-9 - 3E-2 W/cm2-sr in 0.4-1.0 um band, or equivalent in another band	Includes threshold range	4E-9 - 3E-2 W/(cm2-sr) in 0.4-1.0 µm band
V40.2.3.1-12	2. Other bands			
	Daytime Visible	Derived	Derived	5 to 468 W/(m2-sr-µm)
	Mid-Wave Infrared	Derived	Derived	210 K to 353 K
	Long-Wave Infrared	Derived	Derived	210 K to 340 K
V40.2.3.1-13	Measurement Uncertainty			
	Daytime/Nighttime Visible	Derived	Derived	6.5E-10 W/(cm2-sr) @ L = 4.E-09 W/(cm2-sr) (edge of scan)
	Daytime Visible	Derived	Derived	SNR = 130.7 @ Ltyp = 22 W/(m2-sr-µm) (edge of scan), Accuracy = 2%
	Mid-Wave Infrared	Derived	Derived	NEdT = 2.5 K @ Ttyp = 270K (edge of scan), Accuracy = 0.5%
	Long-Wave Infrared	Derived	Derived	NEdT = 1.5 K @ Ttyp = 210K (edge of scan), Accuracy = 0.5%
	f. Mapping Uncertainty			
V40.2.3.1-14	1. At nadir	3 km	1 km (TBD)	
V40.2.3.1-15	2. Worst case	4 km	1 km (TBD)	
V40.2.3.1-16	Minimum Swath Width (All other EDR thresholds met)	3000 km (TBR = 3000 km)	3000 km (TBD)	3000 km

* For Daytime/Nighttime Visible Band, HRI = 742 m., constant to within 5% in both directions within a swath

A schematic comparison of the VIIRS bands listed in Table 2 with the OLS and AVHRR bandsets is shown as Figure 1.
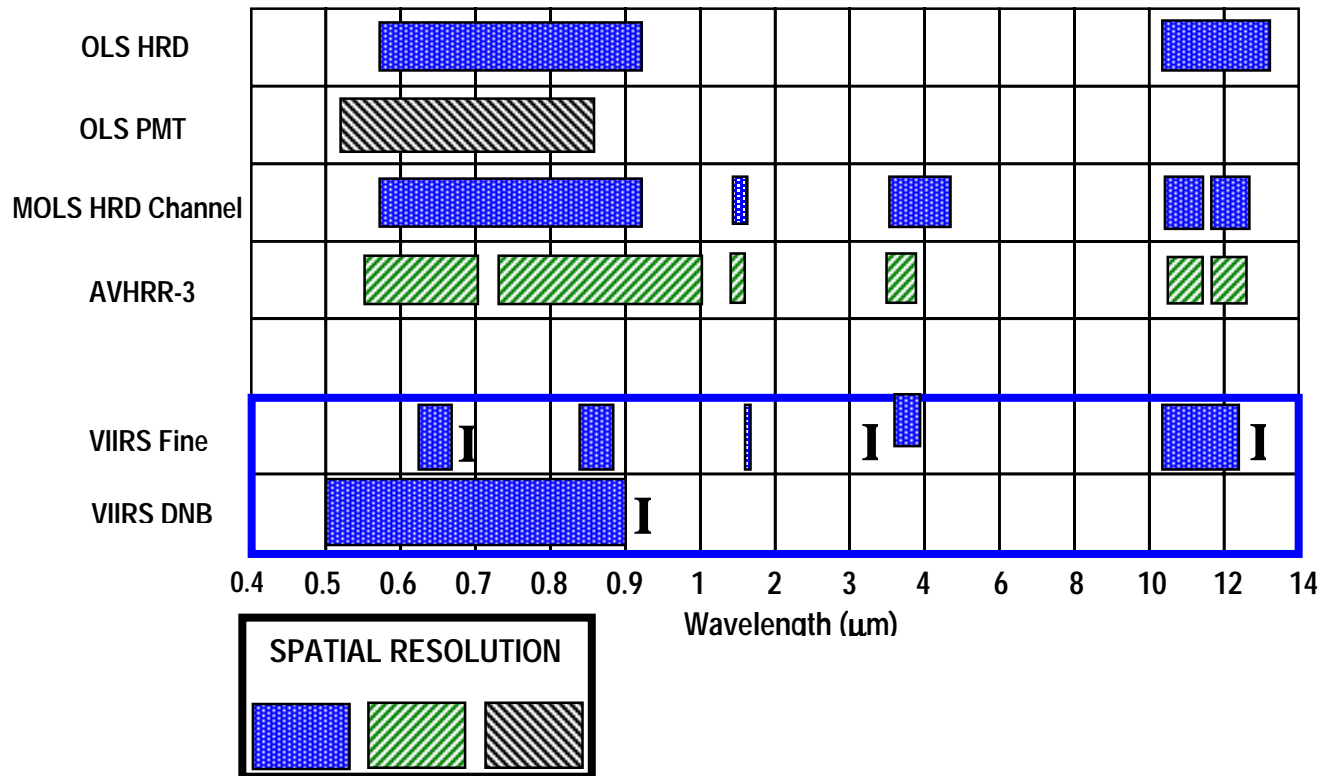
Figure 1. Comparison of the VIIRS band set for Imagery with OLS and AVHRR-3.

VIIRS bands marked "I" are required for imagery thresholds. The legend indicates the spatial resolution of the band sets. OLS PMT channel bands are at coarse resolution (grey). AVHRR-3 bands are at moderate resolution (green). The other band sets are at fine resolution (blue). The VIIRS Imagery EDR benefits from true multi-spectral capability and compatibility with OLS heritage.

2.2.1 Operational Benefits

Important operational benefits of Visible-Infrared imagery are outlined by Mannen (1996). These include general forecasting, ice/ocean analysis, weapons systems support, safety of operations, hazard identification/warnings, and navigation/trafficability.

2.3 NEAR CONSTANT CONTRAST (NCC) VISIBLE IMAGERY

The Imagery EDR includes a daytime/nighttime visible imagery product that maintains apparent contrast under daytime, nighttime, and terminator region illumination conditions. This product, referred to as the Near Constant Contrast (NCC) visible imagery, is to be derived from the daytime/nighttime visible band (DNB) in addition to the calibrated DNB radiances and reflectances. Data from the daytime/nighttime band will be transmitted in the real-time Low Rate Data data stream, and the NCC visible imagery will be made available to users in near real time

following the ground processing needed for its generation. In addition to derived requirements for this product, NCC visible imagery is subject to the following five explicit requirements:

1) The NCC visible imagery shall minimize the apparent transition across the terminator when it is viewed on a graphical display system. This means, in particular, that from the perspective of a human analyst viewing the imagery, the apparent image contrast is maintained across the imagery, and that there are no spatial or other artifacts which adversely affect the utility of the imagery.

2) The HSR of the NCC visible imagery shall meet the HSR requirement of the daytime/nighttime visible band.

3) The HRI of the NCC visible imagery shall be constant to within 5% of its nominal value in both the in-track and cross-track directions within a swath. This requirement does not apply to the horizontal sampling performed by the VIIRS instrument, and may be met by resampling the measured data.

4) The nominal value of the HRI of the NCC visible imagery shall provide gapless or near gapless coverage based on the minimum HSR in either the in-track or cross-track directions across the imagery swath.

5) The NCC visible imagery shall be geolocated by ground processing to meet the mapping uncertainty requirement.

2.4 APPLICATION-RELATED REQUIREMENTS

The content and quality of the imagery shall be adequate to allow certain application-related requirements to be met. These requirements determine the derived requirements of Horizontal Reporting Interval, Measurement Range, and Measurement Uncertainty for the VIIRS imagery bands.

The content of the application-related data products (ARPs) is not part of the content of the imagery EDR, and there is no system requirement to develop algorithms to produce them. However, there was a need for requirements flowdown to explicit imagery requirements which was best met by the development of algorithms to simulate the system performance in producing the ARPs. As a result, we are able to document the theoretical basis and performance of these algorithms as an added benefit of our system solution to the VIIRS requirements.

The application-related requirements apply to manually generated cloud data and to sea ice data

Manually generated cloud data are estimates of cloud cover and cloud type generated by a trained human analyst viewing the unprocessed and/or processed imagery derived from the unprocessed imagery, e.g., by data fusion, spatial rescaling, image enhancement, etc. Data products include cloud cover and cloud type.

Raytheon

Sea ice data may be generated interactively by a trained human analyst viewing unprocessed or processed imagery at a computer workstation, or automatically via an algorithm. Data products include ice edge location and ice concentration. In addition, analysts will attempt to determine the thickness and size of leads and polynyas based on the imagery.

2.4.1 Requirements for Cloud Cover

Cloud cover is defined as the fraction of a given area, i.e., of a horizontal cell, on the Earth's surface for which a locally normal line segment, extending between two given altitudes, intersects a detectable cloud. A detectable cloud is defined in the SRD Glossary as "an aqueous aerosol having a vertical extinction optical depth exceeding 0.03 (TBR) in the visible or a contrast with the background exceeding 0.02 (TBR) in the visible." For manual analyses, cloud cover is estimated for a single atmospheric layer. Specifically, the minimum and maximum altitudes of this layer are defined to be the surface of the Earth and the altitude where the pressure is 0.1 mb. Haze, smoke, dust, and rain are not to be considered clouds. For the purpose of validating this requirement, cloud cover estimates are to be generated by a trained human analyst viewing unprocessed and/or processed imagery for contiguous square areas having side length equal to the horizontal cell size specified below.

The SRD requirements for manual analysis of cloud cover are summarized in Table 3.

Table 3. Specifications for the VIIRS Cloud Cover Imagery ARP

Para. No.		Thresholds	Objectives	Specification Value
V40.2.3.2-1.1-6	a. Horizontal Cell Size	3 (TBR) times the Imagery HSR	2 times the Imagery HSR	3 times the Imagery HSR
V40.2.3.2-1.1-3	b. Horizontal Reporting Interval	Horizontal Cell Size	Horizontal Cell Size	Horizontal Cell Size
V40.2.3.2-1.1-4	c. Measurement Range	0 - 1, 0.1 increments	0 - 1, 0.1 increments	0 - 1, 0.1 increments
V40.2.3.2-1.1-5	d. Measurement Uncertainty	0.1	0.1	0.1

2.4.2 Requirements for Cloud Type:

Cloud types are defined as follows:

(1)   Altocumulus (AC)

(2)   Altocumulus Castellanus (ACCAS)

(3)   Altocumulus (Standing lenticular) (ACSL)

(4)   Altostratus (AS)

(5)   Cirrocumulus (CC)

(6)   Cirrocumulus (Standing lenticular) (CCSL)

(7)   Cirrostratus (CS)

(8)   Cirrus (CI)

(9)   Cumulonimbus (CB)

(10)   Cumulus (CU)

(11)   Cumulus Fractus (CUFRA)

(12)   Towering Cumulus (TCU)

(13)   Stratus Fractus (STFRA)

(14)   Nimbostratus (NS)

(15)   Stratocumulus (SC)

(16)   Stratocumulus (Standing lenticular) (SCSL)

(17)   Stratus (ST)

The Cumulonimbus mama (Mammatocumulus) (CBMAM) cloud type requirement has been deleted from the SRD. Cloud typing not only entails a capability to distinguish between clouds of different type, but also a capability to distinguish clouds from other features, such as snow, cold water, cold land, haze, smoke, dust, etc. Therefore, the following additional types are defined:

(18)   Obscured/not cloudy

(19)   Clear

A given area is classified as "obscured/not cloudy" if there are no detectable clouds within the atmosphere overlying the area and if the average vertical LOS extinction optical thickness of the atmosphere overlying the area is $> = 0.03$ in the 0.4-0.7 μm band. A given area is classified as "clear" if there are no detectable clouds, as defined above, overlying the area and if the average vertical LOS extinction optical thickness of the atmosphere overlying the area is < 0.03) in the 0.4-0.7 μm band. Note that other EDRs require the type of non-cloud obscuration to be discerned and identified, e.g., smoke, dust, sand, ash, etc.

For the purpose of validating this requirement, typing is to be performed by a trained human analyst viewing unprocessed and/or processed imagery for contiguous square areas having side length equal to the horizontal cell size specified below. The probability of correct typing is defined as the probability that a cell reported as being of type x is in fact of type x, where x is any of the types specified above.

The SRD requirements for manual analysis of cloud type are summarized in Table 4.

Raytheon

Table 4. Specifications for the VIIRS Cloud Type Imagery ARP

Para. No.		Thresholds	Objectives	Specification Value
V40.2.3.2.1.2-7	a. Horizontal Cell Size	(TBD) times Imagery HSR	(TBD) times Imagery HSR	3 times Imagery HSR
V40.2.3.2.1.2-3	b. Horizontal Reporting Interval	Horizontal Cell Size	Horizontal Cell Size	Horizontal Cell Size
V40.2.3.2.1.2-4	c. Measurement Range	Clear,obscured/not cloudy,ST,CU,CI	Clear,obscured/not cloudy, all17 cloud types	Clear,obscured/ not cloudy, ST,CU,CI plus 10 cloud types (total = 13 cloud types)
V40.2.3.2.1.2-8	d. Probability of Correct Typing	85% at (TBS) % confidence level	90% at (TBS) % confidence level	85%

2.4.3 Operational Objectives of Manually-Generated Cloud Data

2.4.3.1 Introduction

Historically, imagery-based cloud cover analysis at the Air Force Weather Agency (AFWA) supported Air Force Precedence 1-1 Programs. The required cloud analyses had to be performed upon receipt of Defense Meteorological Satellite Program (DMSP) data in minimum time. The sequence of steps in the cloud analysis and forecast process included:

1) Data ingestion functions:

   a) Processing imagery by the satellite processing mainframe computer

   b) Processing the imagery into the Satellite Data Handling System (SDHS)

Generation of Automated Cloud Analysis

   c) Generation of cloud analysis by the Automated Real Time NEPH analysis (RTNEPH) Model

   d) Manual Quality Control (QC) of the RTNEPH analyses (called "RTNEPH Bogus")

2) Generation of Automated Cloud Forecasts

   e) FIVLYR (Five-Layer) long range forecast model (+03 to +33 hours)

   f) TRONEW (New Tropical Model) 24-hour tropical model (broadly based upon persistence)

   g) HRCP (High-Resolution Cloud Prognosis) short range model

   h) Manual QC of Forecast Products (called "Forecast Bogus")

The entire process was nominally accomplished within a 55 minute timeline. The clock was started when the DMSP spacecraft reached a command readout site and began replaying recorded data. Data ingestion typically required 2-3 minutes. Automated cloud analysis was accomplished in another 5 minutes. Preparation for the RTNEPH Bogus occasionally began prior to data readout (e.g., pre-mapping grid coordinates to satellite image space).   The manual QC (Bogus)

process was allocated 15 minutes, with generally two quarter orbits of data being processed in parallel. At Bogus completion, approximately +22 minutes, RTNEPH edits were sent to the satellite processing mainframe to update the RTNEPH database. This database was used to initialize the various forecast models. Output cloud cover forecasts were displayed on the SDHS over the DMSP imagery alongside ancillary forecast aids (e.g., height, temperature, and moisture fields) and reviewed for correctness by forecasters. Forecast edits were retransmitted to the satellite processing mainframe for database update and final forecast product generation.

2.4.3.2 Weakness in the Current QC System

The RTNEPH Bogus on the SDHS is still accomplished by displaying only two DMSP channels of smooth (1.5 nautical miles) broadband infrared and visual imagery for a quarter-orbit of data simultaneously on two monitors at 1024x1024 resolution in the nominal satellite projection. As many as four sets of these displays are 'scanned' in sequence from the northernmost to the southernmost sections of the quarter-orbit. A third monitor displays a 4:1 reduced view of the entire quarter orbit to provide the analyst with an overview of the entire scene. On the high resolution monitors, digits are displayed over the imagery at RTNEPH grid point locations to represent the automated cloud cover analysis. Only total cloud amount, in eighths, is displayed. All other parameters are currently ignored. Cloud cover of zero eighths is not displayed to emphasize distinctiveness of clear-cloud regions. Because digits are spaced closely in image space (typically no more than 16 pixels from center to center), a special character set is used to display digits with a minimum number of pixels. Additionally, the capability to toggle digits on or off rapidly is available.

Analysts use a multiple monitor slaved draw mode with a digitizing tablet to circumscribe cloud edits around sets of digits which are deemed unrepresentative of the true cloud field. Each single cloud edit label takes the form of a closed curve and may include up to three pairs of cloud amount and cloud type; one each for low, middle and/or high clouds. For example, one Bogus label might include 3 eighths of cumulus, 5 eighths of altocumulus, and 6 eighths of cirrus. More typical an edit label involves only a single cloud layer. Analysts generally estimate lower altitude cloud amounts based on their meteorological understanding of the situation. The RTNEPH bogus edit post-processor uses cloud type labels to assign default cloud base and top altitudes.

The imagery is pre-processed to maximize the dynamic range of pixel brightnesses using local histogram frequency equalization. This technique allows analysts to discriminate clouds from the known (learned by experience and through studying detailed maps) physiographic background. For example, using only DMSP data, low cloud at night are readily discriminated from cold background terrain (so called black-stratus) by the obscuration of terrain features such as low ridgelines, valleys, and rivers. However, the value of these precise cloud edge specifications is generally lost when analyses are ingested into the lower (25 nm) resolution RTNEPH grid.

After a review of the displayed 1024x1024 frame for the quarter orbit is complete, another analyst performs a "quick" review of the edits; then, QC of the next frame of the quarter orbit begins. The QC time schedule only allows the analyst approximately 2-3 minutes per 1024x1024 frame to ensure that a single quarter-orbit is processed within the required timeline. At the end

of the allotted time or when the quarter orbit is completely reviewed, all edits are concatenated and shipped to the satellite processing mainframe to update the database. A hardcopy of the edits is generated and filed for subsequent review. Given the typical 15 minute time budget to review and correct a quarter orbit cloud analysis, the analysts typically are reviewing and correcting 1.5 million square kilometers per minute.

2.4.3.3   Manually-Generated Products During the NPOESS Era

The integration of NPOESS data in general, and VIIRS data in particular, will significantly improve the cloud analysis and forecast system at AFWA. While no attempt is made, at this point, to define an architecture for using these data in AFWA or any other Government facility, there are obvious benefits from using VIIRS in the automated cloud analysis and forecast system at AFWA. These enhancements include:

1. The use of VIIRS imagery will significantly improve the quality of automated cloud analyses which will result in fewer operations being needed to perform the QC, Bogus function. Earlier studies quantified the accuracy of the cloud forecast system at AFWA and recommended further improvements in the cloud analysis and forecast system (Hutchison and Janota, 1989; Hutchison et al., 1990). Recommended enhancements were made to the cloud forecast models and subsequently the time required to perform QC on the automated cloud forecasts became negligible. These studies also stated that "After the recommended enhancements to cloud forecast models were made, the next major step necessary to improve the cloud forecast accuracy was to upgrade the cloud analysis model." Subsequently, the SERCAA Program was undertaken to improve automated cloud analyses; however, these algorithms must continue to rely upon existing meteorological satellite DMSP, TIROS, and GOES data which have inadequate spectral data for generating highly accurate, global cloud analyses. Therefore, significant improvement in cloud detection accuracy will be possible with the added spectral data acquired by VIIRS, as discussed in the VIIRS Cloud Mask ATBD *[Y2412],* and improved automated cloud analyses will result after the cloud forecast system in AFWA is upgraded to process these NPOESS data.

2. The use of VIIRS imagery and imagery assist channels will provide analysts with the capability to more readily distinguish between clouds and cloud-free surfaces, using color composites, which will significantly improve the speed and the accuracy of the QC, Bogus process. As noted earlier, RTNEPH Bogus on the SDHS is accomplished by displaying only two DMSP/AVHRR channels simultaneously on two monitors to view clouds in a gray-scale image. During the NPOESS era, at a minimum, it is recommended that all current SDHS terminals be upgraded to display VIIRS imagery as color composites (i.e. different VIIRS imagery channels, imagery assist channels, channel differences, and/or channel ratios assigned to each gun of a color display) to exploit the unique spectral signatures of cloud and backgrounds and enhance the analysts capability to quickly and accurately perform the QC process on automated cloud analyses. As experience is gained in using and interpreting these color composites, it may be possible to automate the cloud analysis specification to the point that only

occasional manual tunings will be required. Examples of VIIRS color composite are shown in Section 3.4.

3. During the NPOESS era, it is recommended that enhanced software be provided to avoid the need for analysts to estimate lower altitude cloud amounts based solely on their meteorological understanding of the situation. This should be readily achieved using VIIRS automated cloud products, such as the improved cloud height EDR, cloud base EDR, and Raytheon's multilayered cloud EDR with physiographic maps available in SDHS-type terminals. These maps should also include VIIRS-derived land classification (forests, deserts, grasslands, etc.), terrain elevation, all land/water boundaries (rivers, in-land lakes, etc), and major roadways.

4. During the NPOESS era, significant improvements will be realized in the retrieval of atmospheric profiles. While it is uncertain how these profiles might be used in weather centrals, (e.g. where numerical weather prediction models generate fields which may be used in the automated cloud analysis), these profiles will have value for automated cloud analyses at locations that do not run numerical models, e.g. field sites.

5. The quality of manually generated cloud products will always depend on the ability of the analyst. Our flowdown of requirements and assessment of performance has been made under the assumption that the analysts in the NPOESS era will have the benefit of training that includes VIIRS-specific instruction. The current DMSP OLS and TIROS AVHRR sensors have limited spectral content compared to the VIIRS sensor designed by Raytheon. While MODIS will provide the research community with a significantly enhanced capability, the operational community will not fully realize the value of these data until the launch of the NPOESS VIIRS sensor. In the interim, research scientists will continue to improve the algorithm technology and MODIS-derived environmental data products (EDRs). Thus, it becomes essential that the algorithm technology and user knowledge be brought forward together in order to fully realize the value of true multi-spectral VIIRS measurements. We have included an outline of a suggested VIIRS User's Guide for cloud analysts as an Appendix to this document.

Stratus/fog/snow discrimination is an important operational benefit of manual cloud analysis (COBRA, IORD Refs). Stratus detection, a threshold requirement for Cloud Type, is discussed in Section xxxx. Stratus/snow discrimination is also discussed in Section xxxx. Fog detection is not a VIIRS requirement, so we do not have a specification or performance analysis for it. However, fog is physically equivalent to a low-lying stratus cloud. An analyst can discriminate fog from stratus with the assistance of the VIIRS cloud top EDRs (Cloud Top Temperature, Cloud Top Pressure, Cloud Top Height), which can be available as VIIRS ancillary data for the VIIRS Imagery Cloud Data.

2.4.4 Requirements for Ice Edge Location

An ice edge is defined as the boundary between ice-covered sea water (ice concentration > 0.1) and sea water not covered by ice (ice concentration < 0.1). The ice edge generally occurs between the ice free ocean and the contiguous pack ice, although complex patterns of ice concentration may be found, defying such simple interpretations. The advance and retreat of the ice edge during the annual cycle creates a seasonally migrating marginal zone between the open

ocean and the contiguous pack ice. This zone influences atmospheric and oceanic circulation, affecting the development of local and regional weather patterns. In addition, the ice edge can move tens of kilometers per day, significantly disrupting operational activities on the sea surface. Ice edge boundaries are used for navigational planning, and so must be available in a short time. The value of an automated retrieval is indicated by the fact that changes in boundaries are typically on short time scales.

An ice edge is typically provided as a contour on a map or in digital form as a set of latitude/longitude coordinates. The ice edge location error is defined as the distance between the estimated location of an ice edge and the nearest location of a true ice edge.

Our automated algorithm produces ice edge location as a contour on a map (an ice edge image) and also as a set of latitude/longitude coordinates. The coordinates are derived at subpixel resolution from interpolation of the ice concentration map.

The requirements for sea ice edge location are summarized in Table 5.

Table 5. Specifications for the VIIRS Ice Edge Location Imagery ARP

Para. No		Thresholds	Objectives	Specification Value
V40.2.3.2.2.1-1	a. Horizontal Coverage	North of 36 deg north latitude, south of 50 deg south latitude for sea ice.	North of 36 deg north latitude, south of 50 deg south latitude for sea ice.	North of 36 deg north latitude, south of 50 deg south latitude for sea ice.
V40.2.3.2.2.1-2	b. Measurement Range	Any latitude, longitude within coverage domain	Any latitude, longitude within coverage domain	Any latitude, longitude within coverage domain
V40.2.3.2.2.1-3	Measurement Uncertainty	(TBD)	(TBD)	0.4 km at nadir 1.0 km worst case

Ice edge locations from passive microwave have uncertainties of approximately 10 km. VIIRS imagery retrieval of ice edge location represents a significant improvement over passive microwave.

2.4.5 Requirements for Ice Concentration

Ice concentration is defined as the fraction of a given area of sea water covered by ice. It is typically derived from imagery and reported on ocean geographical charts for areas between contours generated by an analyst. For the purpose of verifying the measurement uncertainty requirement, ice concentration is reported as a gridded product for areas of size limited by the HCS requirement and separation limited by the HRI requirement.

The various sea ice centers produce ice concentration products. The advent of a series of visible-infrared sensors with automated cloud masking capability, including AVHRR-3, MODIS, and GLI, is raising expectations in the sea ice operational community.

Requirement to measurement uncertainty, included in the version two, revision a, of the Sensor Requirements Document could not be met if sea ice data are manually generated by ice analyst. We developed algorithms that can be used in operational environment to retrieve sea ice data automatically.

In the expectation that automated ice concentration retrievals from visible-infrared radiometry will be a developing capability over the next decade, we are providing an automated algorithm to retrieve ice concentration from VIIRS imagery bands.

The algorithm includes the derivation of ice fraction for imagery horizontal cells, using tie point analysis of ice surface temperature and/or surface reflectances. Ice concentration is retrieved as a gridded product for imagery resolution with measurement uncertainty better than 0.1 in most cases. The algorithm is described in Section 3.5.

The SRD requirements for sea ice concentration are summarized in Table 6.

Table 6. Specifications for the VIIRS Ice Concentration Imagery ARP

Para. No		Thresholds	Objectives	Specification Value
V40.2.3.2.2.2-4	d. Horizontal Cell Size (at nadir)	2 km	1 km	0.8 km
V40.2.3.2.2.2-5	e. Horizontal Reporting Interval	(TBD)	(TBD)	Imagery HSR (0.4 km at nadir, 0.8 km worst case)
V40.2.3.2.2.2-1	a. Horizontal Coverage	North of 36 deg north latitude, south of 50 deg south latitude for sea ice	North of 36 deg north latitude, south of 50 deg south latitude for sea ice	North of 36 deg north latitude, south of 50 deg south latitude for sea ice
V40.2.3.2.2.2-2	b. Measurement Range	0 - 1, 0.1 increments	0 - 1, 0.1 increments	0 – 1 full continuous range
V40.2.3.2.2.2-3	c. Measurement Uncertainty	0.1	0.1	0.1

2.4.6 Operational Objectives of Sea Ice Data

We use automated algorithms, described in Section 3.5 of this document, to derive sea ice edge location and sea ice concentration. Analysts at ice centers will be able to use our sea ice retrieval, either as a standalone product, or as a time-saving starting point for manual analysis. Both options are intended to allow for the processing of larger amounts of data, by relieving the load on the analysts. The development of fully automated algorithms is critical to the plans of operational ice centers in the NPOESS era. For example, the National Ice Center (NIC) will be responsible for the development of a global, daily strategic ice product. During an IPO sponsored visit to NIC, we were told that the role of automated algorithms in the creation of this product will be "huge". We envision an operational process whereby analysts assimilate our ice product with other data sources at ice centers.

Operational sea ice products are needed for surface and sub-surface navigation in polar regions, and for commercial navigation in coastal zones and fisheries during ice seasons.

The polar oceans comprise approximately 6.5 percent of the Earth's surface, and are covered by sea ice at some time during the course of the annual cycle. At its maximum extent, sea ice blankets ~19 x 10^6 km^2 of the Southern Hemisphere and ~14 x 10^6 km^2 of the Northern Hemisphere. In the Arctic, nearly half of the late-winter maximum of sea ice cover survives the summer melt season and is classified as old ice. The net export of multiyear sea ice through the Fram Strait is balanced by production of multi-year ice in the Arctic basin. In the Antarctic, more than 90 percent of the sea ice found at the time of maximum extent in the late austral winter is formed, grows, and completely melts during the annual cycle, and as such is classified as first year ice.

Remote sensing of long-term trends in the extent of the polar sea ice pack can be a valuable indicator of global climate change. This is particularly true for polar regions, which are believed to be sensitive to global warming, and are too remote for comprehensive *in situ* monitoring.

Linear discontinuities in ice cover (leads, cracks) are typical features of its structure for the winter time. These features are important, influencing thermodynamic and dynamic processes in ice cover as well as tactical operations of vessels and submarines. In particular, a system of leads can be used for effective navigation in high latitudes. In addition, information on discontinuities in ice cover can be used to verify numerical models of ice cover. Operational preparation of ice charts with information on lead distribution presents evident scientific and operational interest. Although they are smaller than polynyas, leads are usually more important in the energy balance of polar regions, because they are much more numerous.

Formation of each individual discontinuity, its size, and its location, are random. But all discontinuities together as a statistical ensemble are not random and can be described mathematically. A statistical description of leads incorporates the following set of characteristics:

- relative area (lead fraction)

- distribution of orientation

- distribution of length

- distribution of width

- distribution of distance between leads

The density of leads and their orientation are closely related with characteristics of large-scale deformations in ice cover, caused by wind and coastline effects. The process of lead formation and evolution can be described mathematically. A combination of observed lead characteristics with simulations of a mathematical model is considered to be very prospective for NPOESS operational work.

The characteristics of leads can be retrieved by trained analysts from Imagery with sufficiently good HSR and signal-to-noise (SNR) performance. The HSR requirement is driven by the

distribution of lead width. Sensors with better HSR invariably detect more leads, suggesting that the number of leads increases with decreasing width.

Our specification for Imagery HSR (c.f. Table 2) is an advance over AVHRR capability, and is roughly comparable to OLS capability and the expected MODIS capability.

Polynyas also play an important role in the energy balance of polar regions. Polynyas are readily detectable by a human analyst as regions of contrast in either visible or thermal bands. Contrast in visible bands is caused by differences in surface reflectance between the pack ice and the polynya. Contrast in thermal bands is primarily due to differences in surface temperature between the pack ice and the polynya.

Detection of polynyas is much easier than detection of leads, and places no special demand on either the ice concentration measurement uncertainty or the HSR of the Imagery bands.

2.5   INSTRUMENT CHARACTERISTICS

The VIIRS sensor design is based on the sensor requirements of the National Polar-orbiting Operational Environmental Satellite System (NPOESS) and on EDR thresholds and objectives. These system-level requirements have been flowed down into a fundamental set of "sensing" requirements which forms the basis for the VIIRS imagery (Hutchison, 1998). The imagery algorithm takes as input Raw Data Records (RDRs) generated from the VIIRS Imagery bands [Y2478] . The RDRs will be geolocated and calibrated to produce TOA radiance Sensor Data Records (SDRs), as discussed in Sections 2.6.1 and 3.2.5). The performance characteristics of the TOA radiance SDRs, listed in Table 7 and Table 8, are obtained from the VIIRS Sensor Specification Document *[PS 154640-101]* and the VIIRS RDR to SDR Conversion ATBD *[Y3261].*

Raytheon

Table 7. Imagery EDR – Input Data Summary (Spatial)

λ(µm)	Δ λ(µm)	GSD (m) at Nadir (Track x Scan)	HSR (m) at Nadir (Track x Scan)	GSD (m) at Edge of Scan (Track x Scan)	HSR (m) at Edge of Scan (Track x Scan)
0.7*	0.40	742 x 742	742 x 742	742 x 742	742 x 742
0.412***	0.020	742 x 262	742 x 786	1600 x 1600	1600 x 1600
0.645*	0.050	371 x 131	371 x 393	800 x 800	800 x 800
0.865***	0.039	371 x 131	371 x 393	800 x 800	800 x 800
1.61***	0.06	371 x 131	371 x 393	800 x 800	800 x 800
3.74**	0.38	371 x 131	371 x 393	800 x 800	800 x 800
11.45*	1.90	371 x 131	371 x 393	800 x 800	800 x 800

*   Explicitly required bands
**   Additional band required to meet Imagery application-related threshold requirements
*** Bands used to enhancement performance of application-related products

Table 8. Imagery EDR – Input Data Summary (Radiometric)

λ(µm)	Δλ(µm)	Ltyp (W/m2-sr-um) or Ttyp	SNR / NEdT at Nadir	SNR / NEdT at Edge of Scan
0.7*	0.4	4.E-9 W/(cm2-sr) (night), 1.e-2 W/(cm2-sr) (day)	30 (night), 600 (day)	7 (night), 200 (day)
0.410**	0.020	44.9	752.3	434.3
0.645*	0.050	22.0	317.9	183.5
0.865**	0.039	25.0	341.8	241.7
1.61***	0.06	7.3	134.5	77.7
3.74**	0.38	270 K	1.11 K	1.92 K
11.45*	1.90	210 K	0.43 K	0.74 K

*   Explicitly required bands
**   Additional band required to meet Imagery application-related threshold requirements
*** Bands used to enhancement performance of application-related products

The radiometric performance of the bands exceeds the specification for Measurement Uncertainty (c.f. Table 2) with margins that allow the performance of the Application-Related Products to meet or approach objective requirements (c.f. Sections 3.4.4 and 3.5.4).

2.5.1 Daytime/Nighttime Visible Band (DNB)

The Daytime/Nighttime Visible band (DNB) is explicitly required by the VIIRS SRD.

DNB data is taken by a sensitive, very-wide-dynamic range Charge-Coupled Device (CCD) detector in the main VIIRS Sensor. The CCD is located adjacent to the VIS/NIR detector chip on the Warm Focal Plane. It is positioned so that as the Sensor scans the image of the Earth across the focal plane, a particular point on earth will be imaged first by the VIS/NIR chip and then by the DNB CCD.

The detective elements of the DNB CCD are 15.4 micrometer by 24.2 micrometer photosites. In the VIIRS sensor each of these photosites images an angle that corresponds to approximately 17 x 11 meters on the ground at nadir. The signals from many of these photosites are combined on the CCD chip to create the analog signals corresponding to entire ground pixels.

To encompass the extreme radiometric dynamic range of day and night scenes, the DNB CCD includes four regions of light-sensitive photosites with three different sensitivities:

Most Sensitive Regions: The CCD includes 2 identical regions incorporating 250 subpixel detectors operated in Time Delay Integration (TDI) mode. TDI gives a total effective integration period 250 times longer than the integration period of a single subpixel detector, and thus increases sensitivity by nearly 250 times. In normal circumstances the signals from these two identical maximum-sensitivity detector regions are added together for further improvement in SNR. However, if radiation should compromise the value of a pixel measurement made by one of the two segments, the corresponding pixel signal from the other segment would be used.

Medium-sensitivity region: A second detecting region on the CCD chip utilizes three subpixel detectors in TDI. This region also has a lower amplifier gain to give it a net radiometric gain that is approximately 200 times less than the gain of the most sensitive regions.

Lowest-sensitivity region: The CCD also incorporates a detecting region which does not incorporate multiple detectors in TDI. In addition, this region incorporates a 35:1 neutral-density filter and reduced amplifier gain, resulting in a radiometric gain approximately 1/475 of the medium-sensitivity region's gain.

The three regions are designed so that before a more sensitive region saturates, the next less sensitive region will have received a signal sufficient to produce an acceptable SNR. Analog signals from all three regions are converted into digital form and processed digitally to select the signal from the region offering the best SNR for each pixel.

The CCD design allows any number of subpixel elements to be aggregated into single pixels as they are read from the CCD. In the VIIRS sensor this capability will be used to generate pixels with near-rectangular sample spacing on the ground. To accomplish this, many different aggregation modes will be used during the course of the crosstrack sensor scan. Since the subpixel aggregation is an additive process, the total number of subpixels aggregated to create each pixel appears as a factor in the radiometric gain of the pixel.

2.5.2   Other Imagery Bands

2.5.2.1 VIIRS Imagery Band Selection Process

Bands selection for the Raytheon VIIRS sensor design is based upon the strength (strong and/or weak) of three components that make up the signatures of each feature. These component are: (a) surface radiance which includes temperature and emissivity or solar reflectivity, (b) cloud absorptivity or refelctivity, and atmospheric transmissivity. Examples of these features in several VIIRS channels are shown in Figure 2.
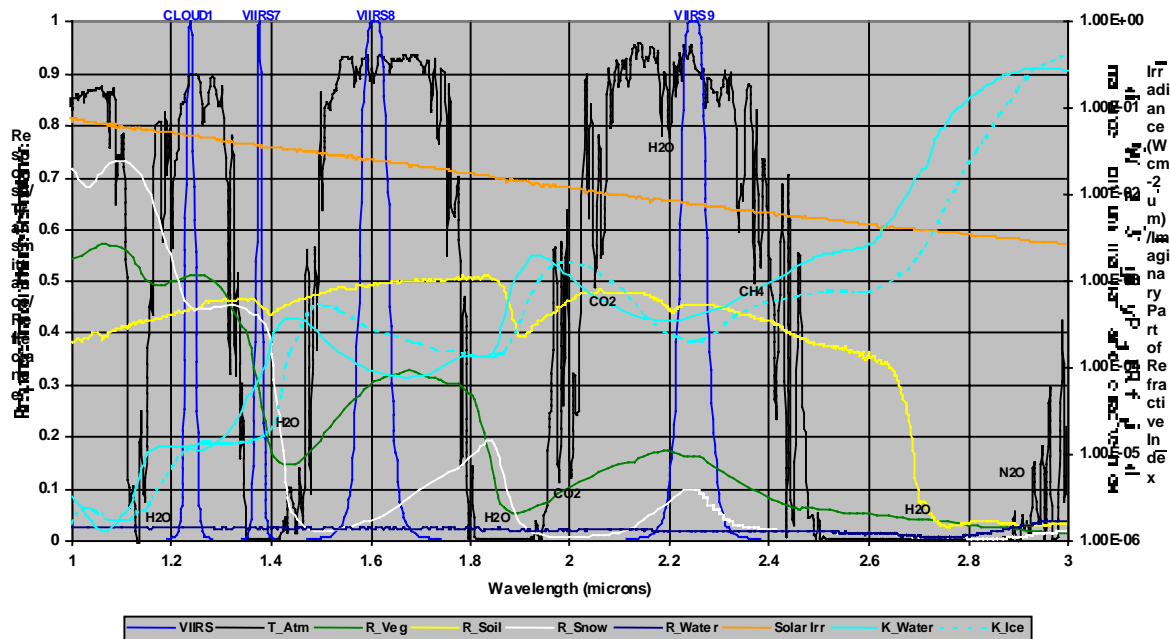
Figure 2. Reflectivity, absorptivity, and transmissivity of atmosphere, surface, and clouds for several VIIRS channels

Figure 2 shows the band positions for VIIRS channels 1, 7, 8, and 9 (**---**) along with atmospheric transmissivity (**---**), reflectivity of vegetated (**---**) and bare soil (**---**) ice (white) and water surfaces (**---**), solar irradiance (gold), and imaginary components of the index of refraction for water (**---**) and ice (**---**).

The positive identification of clouds in multispectral imagery requires that the analyst understand and exploit the properties of water droplets and ice crystals, along with the spectral characteristics of different backgrounds in VIIRS imagery and imagery-assist bands. A discussion of the phenomenology associated with the features follows along with the definition of bands selected to meet VIIRS threshold and objective requirements for the application-related products.

2.5.3 Daytime Visible Band (DV)

The Daytime Visible band (DV) is explicitly required by the VIIRS SRD. Unlike the DNB, the Measurement Range and Measurement Uncertainty requirements are determined by the application-related requirements on manually generated cloud data and sea ice data. Flowdown of application-related requirements to DV band requirements was performed to establish the spectral response and noise requirements for the DV band (Hutchison, 1998).

The Raytheon daytime visible imagery is centered at 0.645 microns. The justification for this selection is shown in Figure 3.
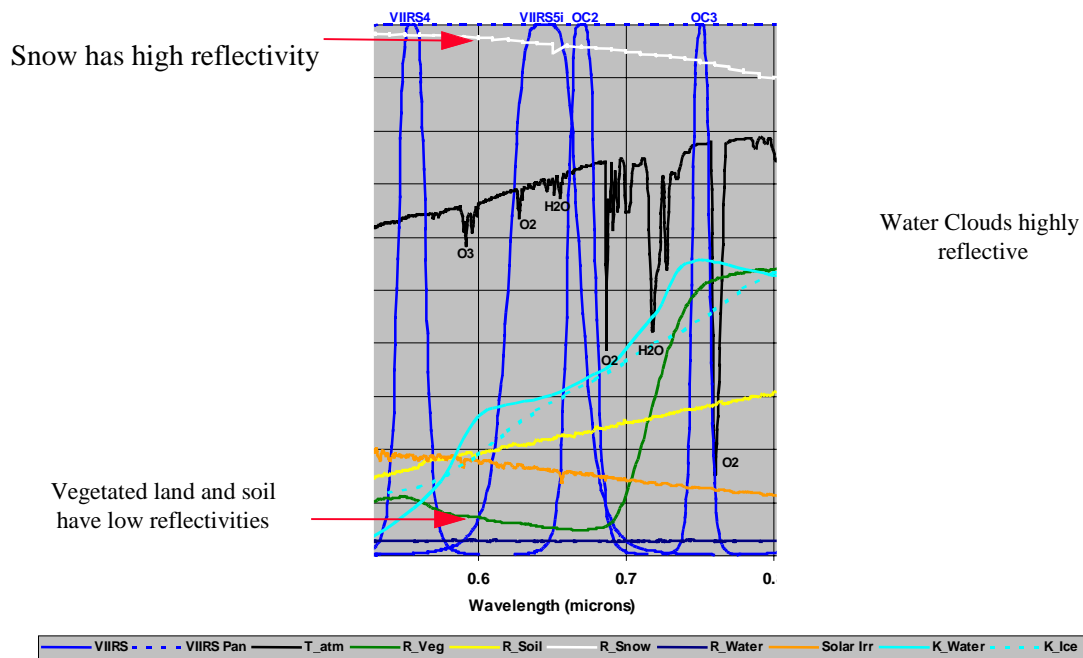
Figure 3. Phenomenology of the VIIRS Daytime Visible (DV) Imagery band, centered at 645 nm.

Figure 3 shows the location and spectral response function for the daytime visible band, along with the characteristics of the Earth-atmosphere system. It is clear that the reflectivity of vegetated land is very small in this band but it begins to increase quite rapidly at ~ 0.7 microns. By limiting the width of the band between 0.6-0.7 microns, we also avoid the water vapor absorption lines in the 0.7-0.8 micron region which could cause variations in cloud and land signatures. The reflectivity of water surfaces is even lower. On the other hand, the reflectivity of clouds is much larger which means this band is particularly valuable for discriminating between clouds and vegetated land and ocean surfaces. Additionally, the reflectivity of snow is very high. Therefore, this channel is not good for differentiating between snow and clouds nor is it particularly useful for identifying boundaries between land and ocean surfaces.

2.5.4   Long-Wave Infrared Band (LWIR)

An infrared band is explicitly required by the VIIRS SRD. We have interpreted the requirement to be for a thermal infrared band, free of solar contamination, which we designate as the Long-Wave Infrared (LWIR). This interpretation is most consistent with OLS heritage. Unlike the DNB, the Measurement Range and Measurement Uncertainty requirements are determined by the application-related requirements on manually generated cloud data and sea ice data. Flowdown of application-related requirements to LWIR band requirements was performed to establish the spectral response and noise requirements for the LWIR band (Hutchison, 1998).   The phenomenology of the 12 micron band used for flowdown is spectrally analagous to the 11.45

micron phenomenology. Therefore, the conclusions of our flowdown can be applied to the VIIRS LWIR imagery band at 11.45 microns.

The Long-Wave Infrared band (LWIR) is explicitly required by the VIIRS SRD. Unlike the DNB, the Measurement Range and Measurement Uncertainty requirements are determined by the application-related requirements on manually generated cloud data and sea ice data. Flowdown of application-related requirements to LWIR band requirements was performed to establish the spectral response and noise requirements for the LWIR band (Hutchison, 1998).

Figure 4 shows the location and spectral response function for the VIIRS LWIR band, along with the characteristics of the Earth-atmosphere system
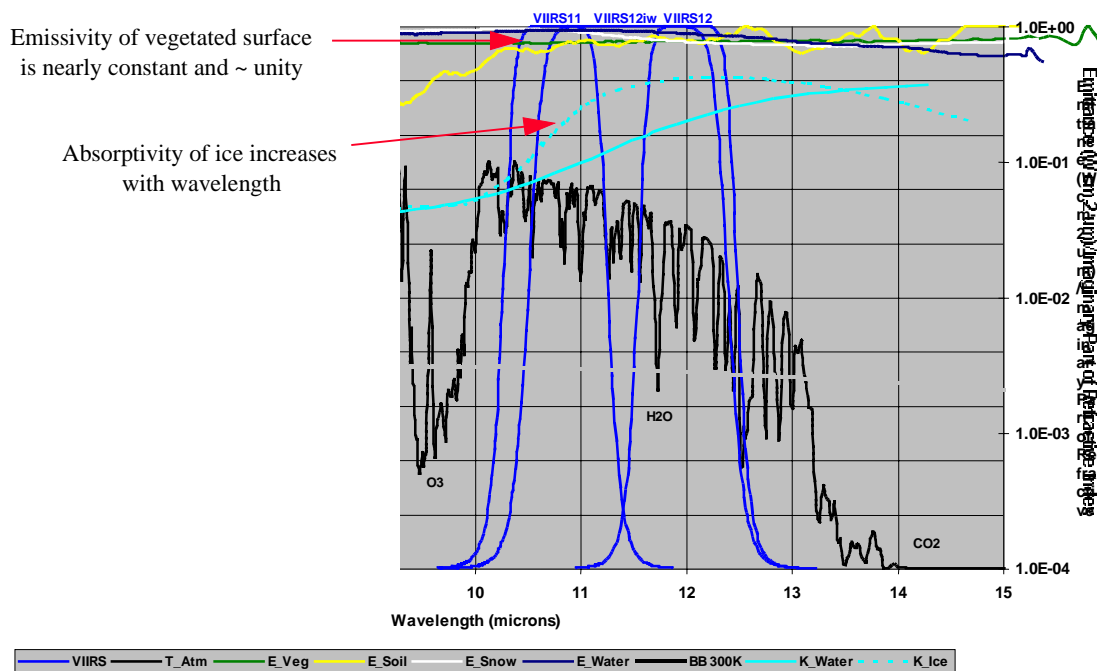
Figure 4. Phenomenology of the VIIRS Long-Wave Infrared (LWIR) Imagery band, centered at 11.45 microns.

Figure 4 shows the water vapor absorption across the LWIR band. The band is valuable for estimating the true radiating temperatures of objects in the band after correcting for atmospheric water vapor attenuation, which makes the measured cloud top temperature slightly colder than its true radiating temperature. In addition, due to the high absorptivity of ice at these wavelengths, thin cirrus is often easily detected in nighttime conditions, when other VIIRS data in the 1.378 micron band are not available

2.5.5 Mid-Wave Infrared Band (MWIR)

In addition to the minimum required daytime visible and infrared imagery channels, the Raytheon specification includes a mid-wavelength infrared imagery channel, centered at 3.74 microns, and shown in Figure 5.
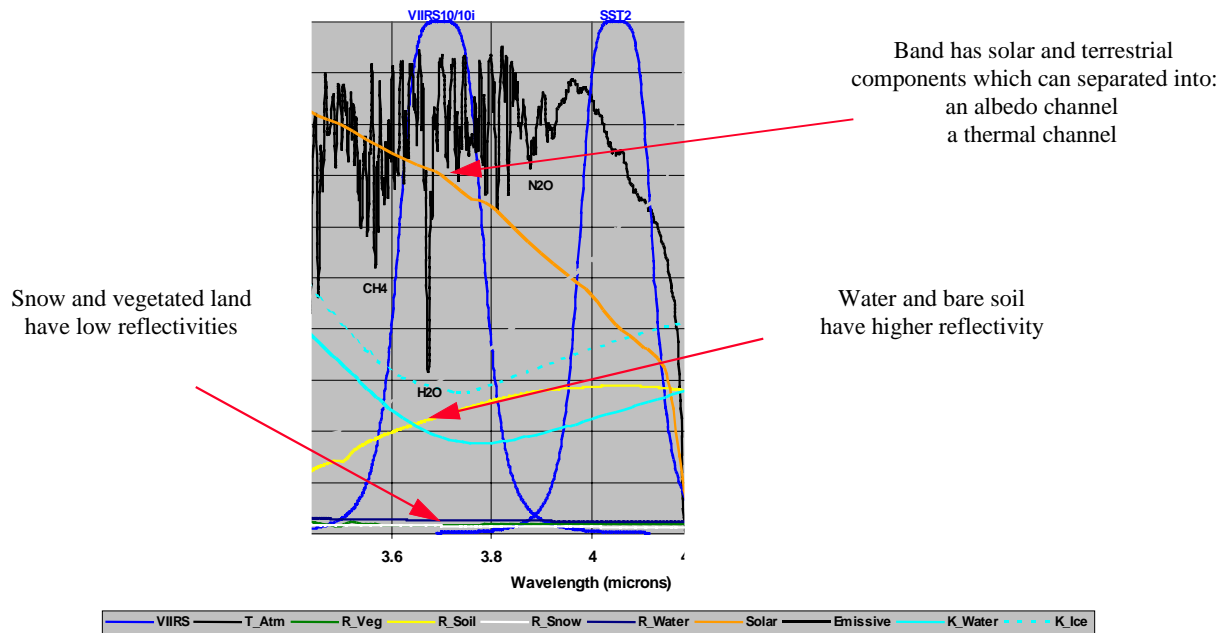
Figure 5. Phenomenology of the VIIRS Mid-Wave Infrared (MWIR) Imagery band, centered at 3.74 microns.

Figure 5 shows water vapor absorption lines in the the VIIRS MWIR band. It also shows that the reflectivity of snow is very low which that of clouds is much larger. It also shows that considerable solar irradiance is present while the reflectivity of bare soil is relatively large compared to snow and clouds. Therefore, the 3.74 micron band could be useful for differentiating between snow and clouds as well as clouds and vegetated land. However, distinction between cloud and bare soil appears difficult and the presence of terrestrial energy complicates the contrast between snow and clouds.

While the daytime 3.74 micron band imagery channel contains both solar and thermal energy, the capability has been demonstrated to separated this single channel into two channels and thus improve the discrimination between features in the spectral band. This process has been described in the literature (Hutchison et al., 1997) and utilizing the derived albedo channel allows significantly enhances the contrast between snow and water clouds. In fact the procedure also sufficiently enhances the contrast between snow and cirrus (ice) clouds so that snow can be observed through overcast cirrus cloudy conditions. Furthermore, the VIIRS flowdown process demonstrated that the thermal channel proves highly effective at differentiating between water clouds and bare soil. Finally, the nighttime 3.74 micron band image has been widely used for detection and identification of nighttime stratus, especially when coupled with the VIIRS LWIR band.

Flowdown of application-related requirements has resulted in the specification of an additional imagery band in the Mid-Wave Infrared (MWIR). The band, at 3.74 microns, is needed to meet the threshold requirement for the Cloud Cover ARP.

The VIIRS sensing requirements were established using a series of simulations for the following cases.

    a. Case 1: Stratus at Night

    b. Case 2: Daytime and Nighttime Cirrus

    c. Case 3: Cloud Typing (Stratus versus Cirrus)

    d. Case 4: Cumulus

    e. Case 5: Daytime Obscurations

The simulations assumed the minimum of number of imagery bands as required by the VIIRS SRD, i.e. one for daytime visible, one nighttime visible, and one infrared imagery band. While completing the initial set of simulations, it was determined that differentiating between nighttime stratus and cirrus clouds was not possible without the MWIR band, i.e. Case 3 results did not meet specifications. Thus, the MWIR band was added to the minimum "sensing" requirement for VIIRS imagery. With the MWIR band added, Case 1 and Case 2 were re-analyzed using the brightness temperature differences (BTD) between the MWIR and LWIR imagery bands. The addition of the bi-spectral signatures of these clouds in the BTD imagery reduced the Raytheon VIIRS sensor noise model specifications necessary to meet threshold requirements. In addition, in Case 4, the daytime MWIR imagery was broken into thermal and albedo components as described in the literature (Hutchison et al., 1997) and used to differentiate between cumulus and snow fields along with stratocumulus over deserts conditions. Cumulus clouds over other backgrounds is trivial. Finally, the simulations were completed for Case 5 to establish that an optical depth of aerosol greater than 1 is required for detection with the LWIR imagery band.

2.5.6 Imagery Assist Bands

The VIIRS SRD specifies that the spectral bandpasses required to meet the threshold requirements for the manually-generated cloud cover EDR and cloud type EDR must be at the "imagery" resolution. The flowdown of these requirements determined that only three spectral bands were required to meet the threshold requirements (Hutchison, 1998). However, the Raytheon cloud and imagery IPTs also demonstrated the use of imagery bands with imagery-assist data, collected at a more coarse resolution, to advance toward meeting objective requirements, especially for the cloud typing EDR. Therefore, this section begins with a discussion of the phenomenology associated with the selection of the VIIRS imagery channels in the Raytheon design. Subsequently, the phenomenology associated with non-imagery channels is presented for the bands which provide useful information for the manual detection of clouds and their classification by type.

The NIR band is available at the fine resolution of the Imagery bands, because of non-Imagery EDR requirements. It is useful to improve performance of the sea ice data application-related products (c.f. Section 3.5.4).

The SWIR band is available at the fine resolution of the Imagery bands, because of non-Imagery EDR requirements. It is useful as a snow-ice/cloud discriminator.

A number of VIIRS bands are useful for RGB color composite cloud analysis (c.f. Section 3.4.3.4). These include the fine resolution bands at 0.865 µm and 1.61 µm, and the moderate resolution bands at 0.41 µm, 1.38 µm, 4.05 µm, 8.55 µm, and 10.76 µm,

2.6 RETRIEVAL STRATEGY

2.6.1   Imagery SDRs

Imagery SDRs will be produced from the VIIRS Raw Data Records (RDRs) by an RDR to SDR conversion, as described in the VIIRS RDR to SDR Conversion ATBD *[Y3261]*. They will be produced as image pixels separated by the Horizontal Reporting Interval (HRI). A process of sampling and aggregation will achieve an HRI roughly equivalent to the Horizontal Spatial Resolution (HSR).

Details of this process are found in the VIIRS Sensor Specification Document *[PS 154640-101]* and the VIIRS RDR to SDR Conversion ATBD *[Y3261]*, and will be further discussed in Section 3.2.5.

2.6.2   Top-of-Atmosphere Radiances

Calibrated top-of-atmosphere (TOA) radiances for all imagery bands will be produced in the Build-SDR module, following the system standards for VIIRS SDRs. An overview of the process is given in Section 3.2.1. A full description of the process is documented in the VIIRS RDR to SDR Conversion ATBD *[Y3261]*.

2.6.2   Top-of-Atmosphere Reflectances

Calibrated top-of-atmosphere radiances in the daytime visible (DV) and daytime/nighttime visible (DNB) imagery bands will be converted to top-of-atmosphere reflectances, as described in the VIIRS RDR to SDR Conversion ATBD *[Y3261]*.

2.6.3   Equivalent Blackbody Temperatures

Calibrated TOA radiances in the Mid-Wave Infrared (MWIR) and Long-Wave Infrared (LWIR) imagery bands will be converted to equivalent blackbody temperatures, as described in the VIIRS RDR to SDR Conversion ATBD *[Y3261]*.

2.6.4   Near Constant Contrast (NCC) Visible Imagery

The NCC visible imagery EDR will be generated from Daytime/Nighttime Visible Band (also called Day/Night Band or DNB) data. Calibrated top-of-atmosphere radiances in the 0.5-0.9µm band will be taken and normalized to produce the NCC imagery. A description of the algorithm will be given in Section 3.3.

2.6.5 Manually-Generated Cloud Data

Our system solution produces radiances, reflectances, and equivalent blackbody temperatures that are sufficient for an analyst to generate the cloud data products.

2.6.6 Sea Ice Data

Automated algorithms will be used to derive ice edge location and ice concentration. The algorithms will function in the Snow/Ice Module, as an integral part of the software architecture for producing Snow/Ice EDRs as well as Imagery ARPs. The processing outline is described in Section 3.5.1.

Although ice edge location and ice concentration are application-related products of the Imagery EDR, similar algorithms and input data are used for the Fresh Water Ice Sea Ice Age/Edge Motion EDRs. There is a large degree of commonality between the algorithm theoretical basis for Imagery Sea Ice ARPs and that for Fresh Water Ice [Y2404]. Also, the sea ice Imagery ARPs are required as input data to the algorithm for the retrieval of Sea Ice Age/Edge Motion EDR products[Y2409].

A description of the algorithm and its data flows will be given in section 3.5.

Raytheon

3.0 ALGORITHM DESCRIPTION

3.1 OVERVIEW

The imagery algorithm consists of four major processing functions:

1. The Imagery SDR process

2. The NCC imagery product process

3. The manual cloud analysis product process

4. The sea ice data product process.

3.2 IMAGERY SDR PRODUCTION

3.2.1 Processing Outline

Imagery SDRs are computed from the RDRs, as part of the Build-SDR module, which applies geo-location, gridding, and calibration to the RDRs. The functionality of the Build-SDR module will allow it to produce SDRs which fully meet the explicit imagery requirements. These SDRs are therefore the basic Imagery EDR product. The process is documented in the Build-SDR Module Software Architecture Document *[Y2479]* and in the VIIRS RDR to SDR Conversion ATBD *[Y3261]*.

3.2.2 Algorithm Input

The Imagery SDR algorithm requires the VIIRS Raw Data Records (RDRs) for each imagery band. These RDRs are created by the ingest function of the IDPS. The process is described in the Build-RDR Module Software Architecture Document *[Y2478]*.

3.2.2.1 VIIRS Data

The required VIIRS data are the VIIRS RDRs, which contain the basic digital numbers to be converted into radiance or reflectance by applying calibration coefficients. The calibration coefficients themselves are also included in the RDR, along with other elements of the telemetry needed for gridding and earth location.

3.2.2.2 Non-VIIRS Data

No non-VIIRS data are required for the generation of the Imagery SDRs.

3.2.3 Theoretical Description

The production of TOA radiances from application of calibration coefficients, TOA reflectances, and equivalent blackbody temperatures is discussed in the VIIRS RDR to SDR Conversion ATBD *[Y3261]*.

3.2.4 Archived Algorithm Output

The imagery RDR to SDR process creates TOA radiances in all bands. The process also creates TOA reflectances in the daytime visible and daytime/nighttime visible bands. The process also creates equivalent blackbody temperatures for the Mid Wave IR band and the Long Wave IR band. All Imagery SDR products shall be calibrated, geolocated, corrected for Earth curvature and satellite motion, and reported for a set of earth locations forming an approximately rectangular lattice. The lattice spacing will be 742 +/- 5% meters for the DNB, and approximately equivalent to the HSR for the other imagery bands.

3.2.5 Performance of Imagery SDRs

The Imagery SDRs are created from the VIIRS Raw Data Records (RDRs).

The RDRs are obtained by a rotating telescope scanning mechanism that minimizes the effects of solar impingement and scattered light. The VIIRS scan will extend to 55.86 degrees on either side of nadir, providing a swath of 3000 km for the nominal satellite altitude of 833 km.

The scanning approach optimizes both spatial resolution and signal to noise ratio (SNR) across the scan. The concept is illustrated in Figure 6.

Fine-Resolution Bands for Imagery

Nadir	**2028 km**	**3000 km**
• aggregate 3 samples • SNR increases by sqrt(3)	• limit for aggregating 2 samples • SNR increases by sqrt(2)	• no aggregation

371 m   131 m   393 m

605 m   393 m   786 m

800 m   800 m
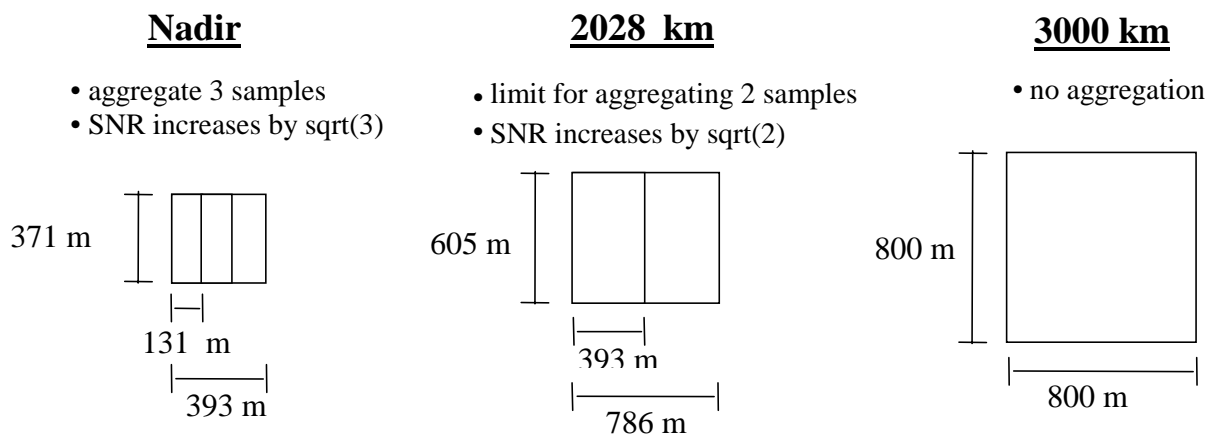
Figure 6. VIIRS detector footprint aggregation scheme for building imagery "pixels".

The VIIRS detectors are rectangular, with the smaller dimension projecting along the scan. At nadir, three detector footprints are aggregated to form a single VIIRS pixel. Moving along the scan away from nadir, the detector footprints become larger both along track and along scan, due to geometric effects and the curvature of the Earth. The effects are much larger along scan. At 31.59 degrees in scan angle, the aggregation scheme is changed from 3x1 to 2x1. A similar switch from 2x1 to 1x1 aggregation occurs at 44.82 degrees. The VIIRS scan consequently exhibits a pixel growth factor of only 2 both along track and along scan, compared with a growth factor of 6 along scan which would occurs without an aggregation scheme.

Figure 7 shows the Horizontal Sampling Interval which results from the combination scan/aggregation scheme.
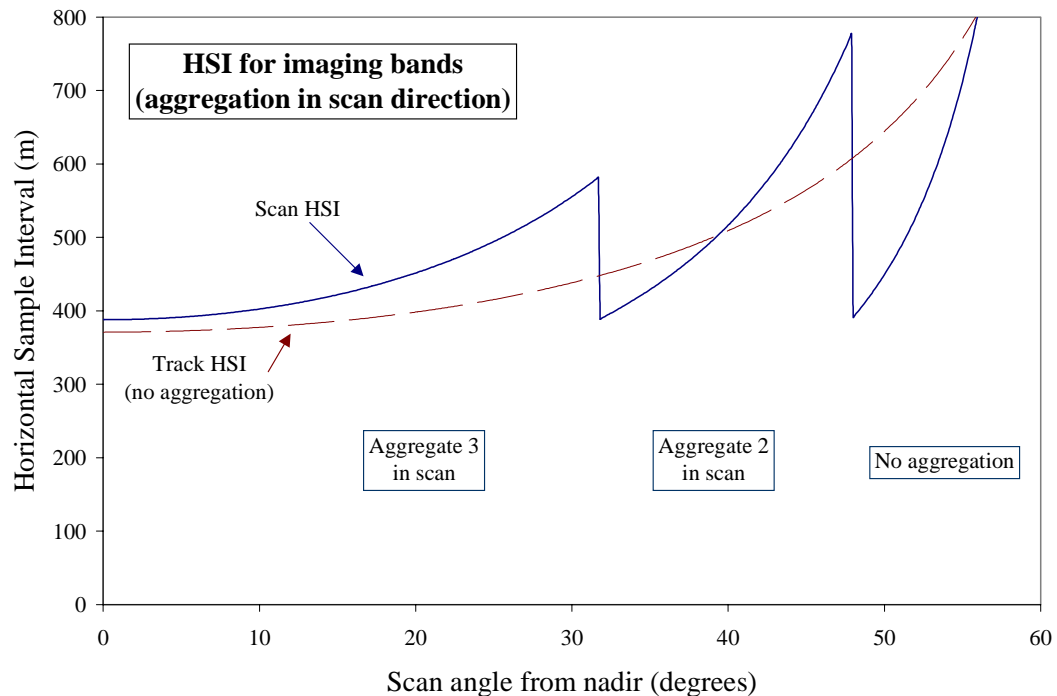
Figure 7. Horizontal Sampling Interval (HSI) for imagery bands (aggregation in scan direction).

The Horizontal Reporting Interval (HRI) of the Daytime Visible (DV), Long-Wave Infrared (LWIR) and Mid-Wave Infrared (MWIR) imagery SDRs will be the HSI. The Modulation Transfer Function (MTF) specification is 0.5 at the sampling Nyquist frequency, resulting in HSR equal to HSI. Therefore, our specification for HRI is equivalent to the imagery HSR specification.

The sensitivity performance of the VIIRS imagery bands (c.f. Table 8 in Section 2.5) exceeds the Measurement Uncertainty specifications listed in Table 2 with comfortable margin.

3.2.5.1 Daytime/Nighttime Visible Band

The TOA radiances and TOA reflectances are produced over the entire operating range of the DNB.

The SNR performance of the DNB at nadir is shown in Figure 8. The performance at edge of scan is shown in Figure 9.

DNB SNR vs Radiance @ Nadir (Max. Aggregation)
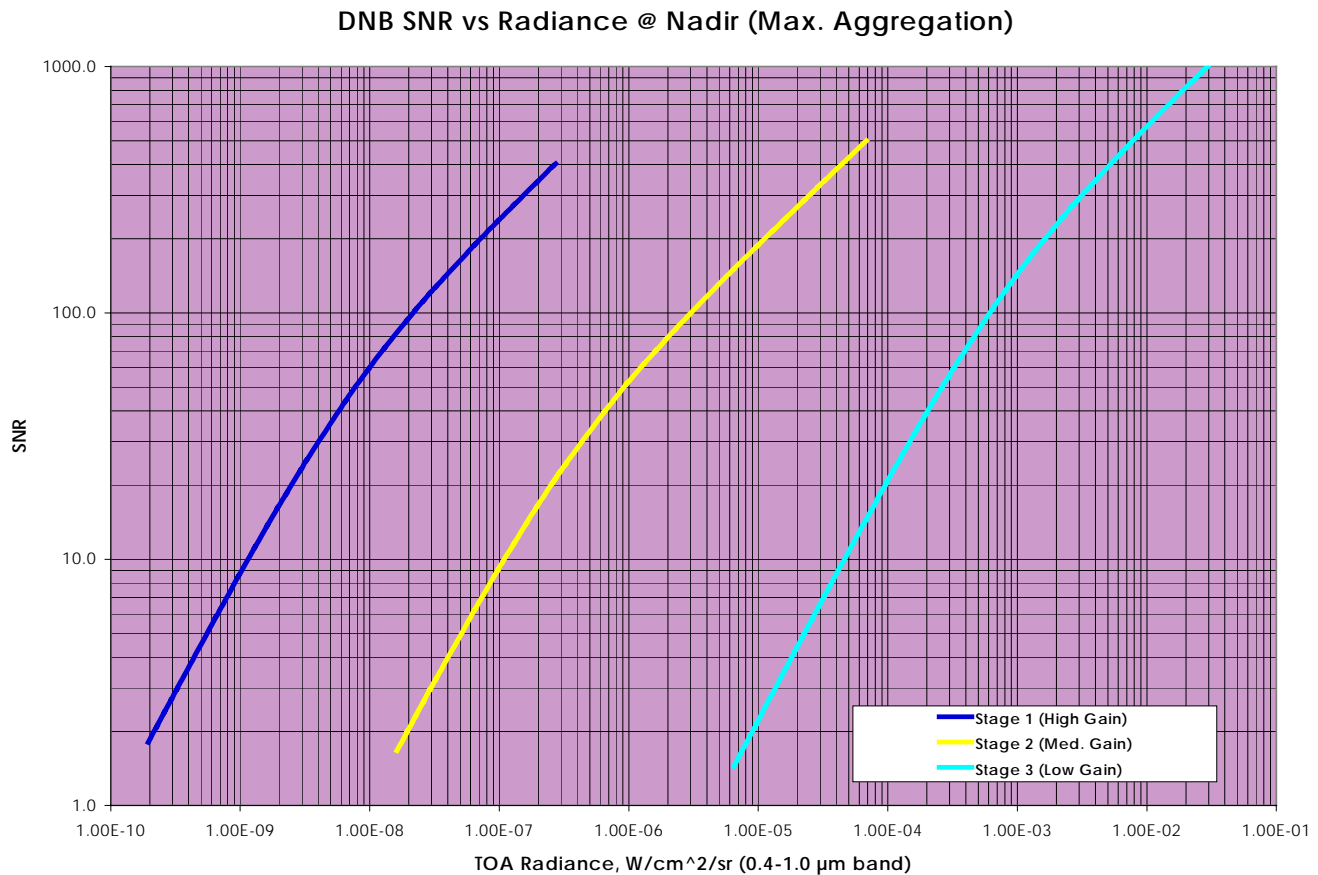
Figure 8. Signal-to-noise performance of the Daytime/Nighttime Visible Imagery Band at nadir, for each of the three CCD gain stages. SNR performance over the specified measurement range (4.E-9 – 3.E-2 W/cm^2/sr) is 30 to 1000. SNR greater than 3 is achieved at a radiance as low as 3.2E-10 W/cm^2/sr.
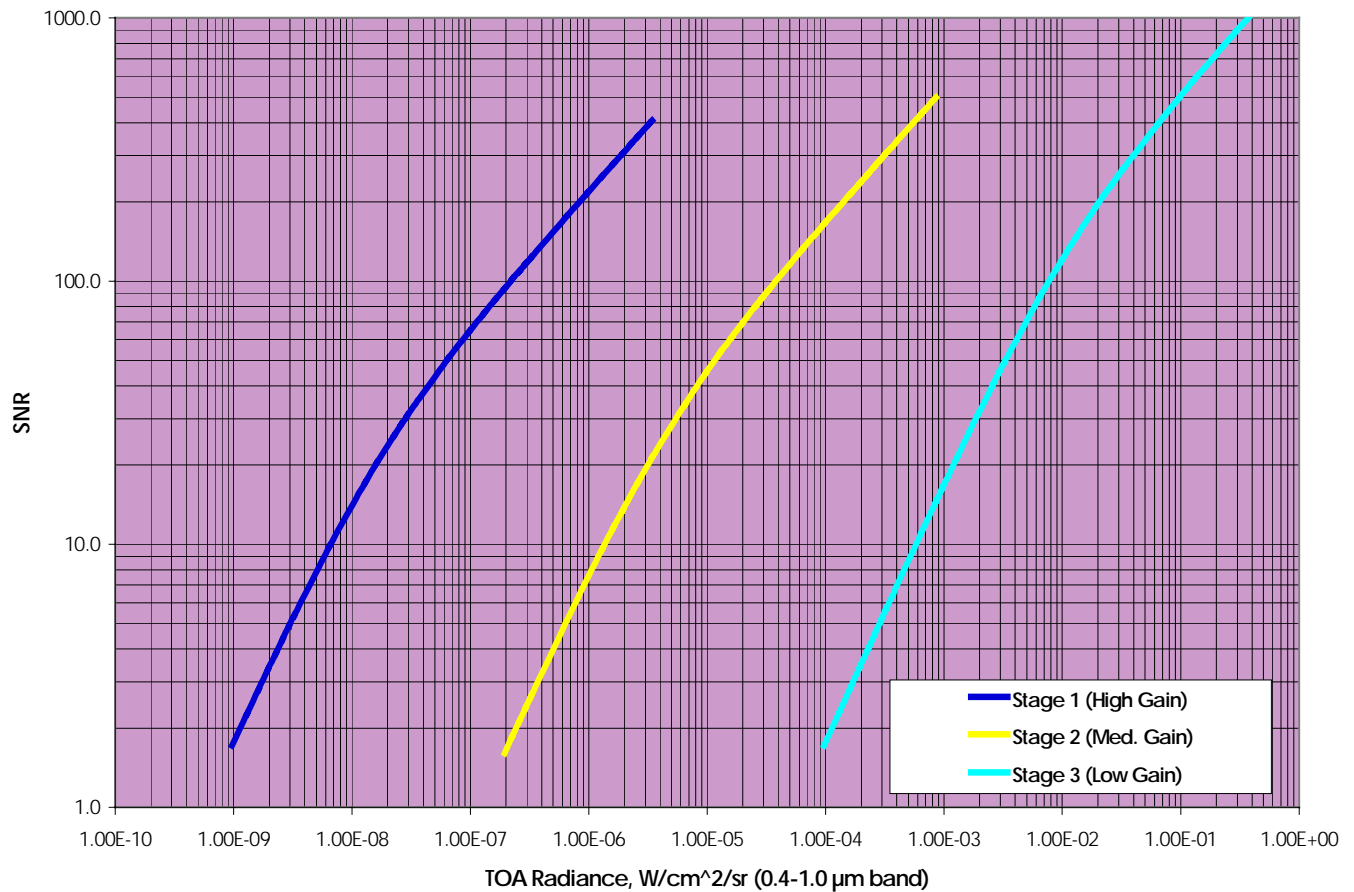
Figure 9. Signal-to-noise performance of the Daytime/Nighttime Visible Imagery Band at edge of scan, for each of the three CCD gain stages. SNR performance over the specified measurement range (4.E-9 – 3.E-2 W/cm^2/sr) is 7 to 250. SNR greater than 3 is achieved at a radiance as low as 1.8E-9 W/cm^2/sr.

The spectral response of the DNB has been designed to operate efficiently under lunar illumination conditions, as shown in Figure 10.

Relative Lunar Signal & Sensor Response
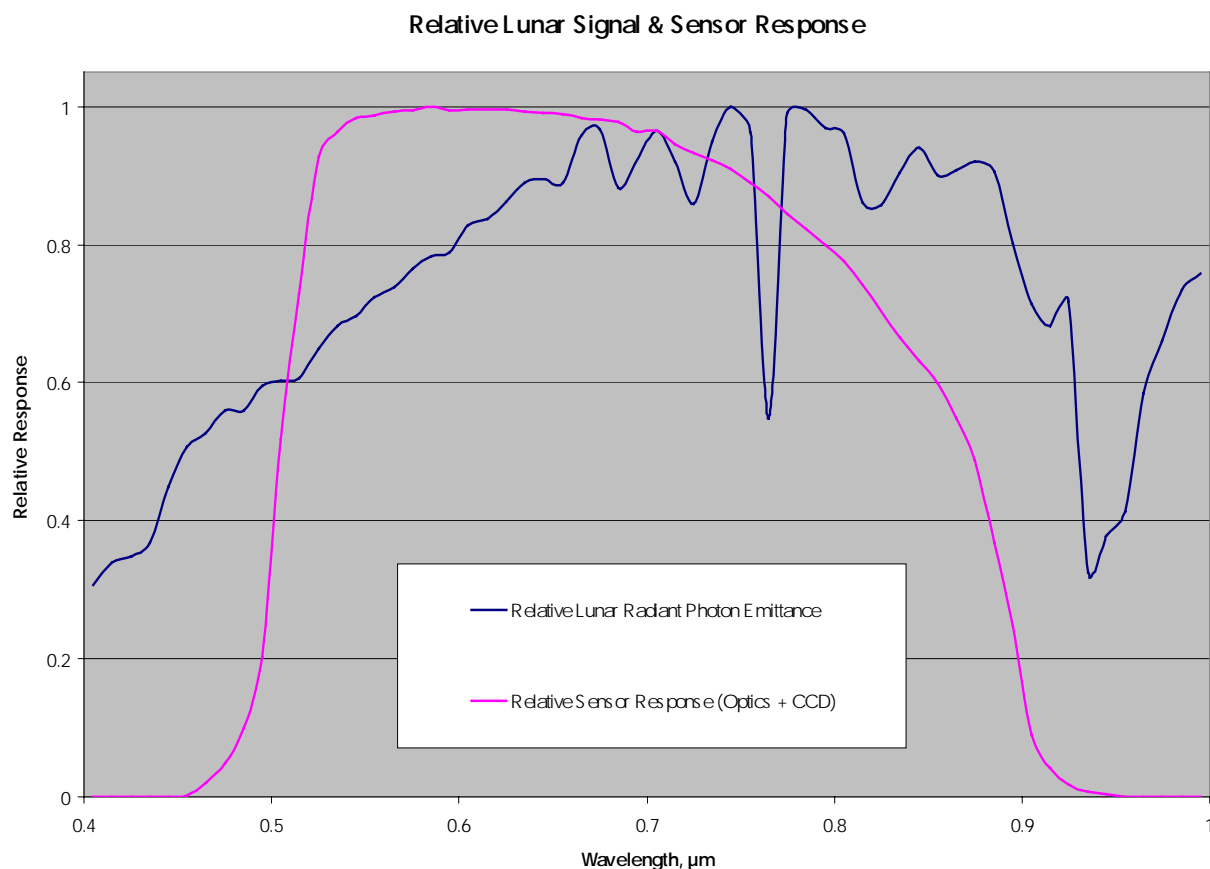
Figure 10. Spectral Response of the Daytime/Nighttime Visible Imagery band, compared with the lunar signal.

The spectral response of the DNB is designed to decline sharply at 0.5 microns, as can be seen in Figure 10. The purpose of the short-wave cut-off is to reduce the contamination of atmospheric path radiance, which is more pronounced at shorter wave lengths. The current design is compatible with OLS heritage.

Raytheon

SNR performance at night will vary with lunar phase, lunar elevation angle, and scan angle. An example for quarter moon phase is shown in Figure 11.
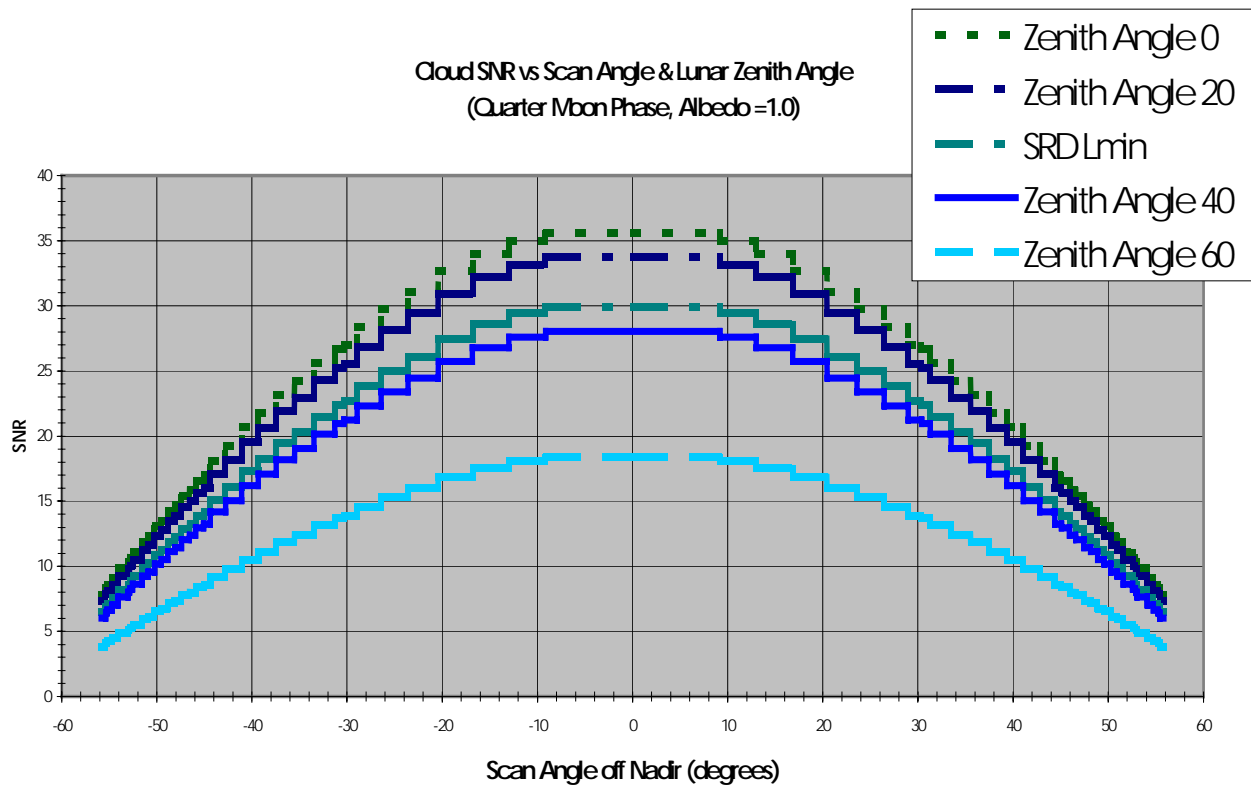
Figure 11. SNR Performance of the Daytime/Nighttime Visible Imagery under quarter-moon illumination conditions, as a function of scan angle.

The top two curves and bottom two curves represent lunar zenith angles of 0, 20, 40, and 60 degrees respectively. The middle curve corresponds to the minimum measurement range of 4E-9 W/cm2/sterad. SNR greater than 10 is achieved at the minimum radiance for almost the entire scan. SNR as high as 30 is achieved at the minimum radiance for a nadir view.

3.2.5.2 Other Imagery Bands

Performance characteristics for the Daytime Visible (DV), Long-Wave Infrared (LWIR), and Mid-Wave Infrared (MWIR) imagery bands meet specifications with comfortable margin (c.f. Figure 7, Table 7, and Table 8).

3.3 NCC VISIBLE IMAGERY PRODUCTION

3.3.1 Processing Outline

The VIIRS day/night broad band CCD consists of detectors operating at three stages:

1) Stage 1 (nighttime mode): If the smallest solar zenith angle to any pixel in the swath is greater than a system-defined threshold value (e.g. 96°), then the daytime visible band is not sent to the satellite data handling system (note: a 96° solar zenith angle is the dark boundary of the civil twilight zone)

2) Stage 2 (terminator mode): If the solar zenith angle to any pixel in the swath is between 80° and 96° then both the low-light visible band and the daylight visible band are sent to the satellite data handling system

3) Stage 3 (daytime mode): If the largest solar zenith angle to any pixel in the swath is less than a system-defined threshold value (e.g. 80°), then the low-light visible band is not sent to the satellite data handling system

In terms of local time, a 96° solar zenith angle at 118° west, 33° north occurs at 0412 AM and 735 PM standard time on June 21st, and at 625 AM to 515 PM standard time on December 21st.

The remainder of this section describes the NCC Imagery EDR ground processing, which is executed only on data generated during periods of Terminator mode operation. The NCC algorithm takes calibrated and geolocated radiance as input. Thus, before the algorithm can be executed, a preprocessing step must be taken to convert the RDR to SDR *[Y3261].*

The production of the NCC Visible Imagery is primarily based on the following four procedures: a) path radiance reduction; b) radiance normalization; c) noise detection and reduction; and d) detector stage boundary smoothing. Path radiance reduction is primarily for viewing the surface features. In terminator region, due to strong atmospheric scattering caused by the long path length, a large portion of the radiance received by the sensor is path radiance, which reduces significantly the visibility of surface features. This path radiance must be minimized in order to enhance the visibility of the surface. The normalization procedure is used to normalize the significant radiance difference caused by the changing illumination condition across the terminator region. The normalization is performed through the use of a pre-constructed lookup table based on a reference surface with constant albedo. The noise detection and reduction procedure is to fly out pixels caused by possible mismatch between the radiance in the pre-constructed LUT and radiance recorded by the sensor. The smoothing procedure is used to smooth any possible discontinuity in pixel values caused by the detector stage change across the terminator.

The NCC Imagery algorithm operates as follows:

NCC1: read the pre-constructed LUT into memory.

NCC2: Determine the number of rows of data that can be read in. The number of rows that can be read in depends on the memory of the computer, the swath width and the pixel size. Based on the current sensor design and memory size of the Raytheon's VIIRS server, a typical value of 2000 seems reasonable.

NCC3: Allocate memory for 2000 row worth of input data (this should include memory space for radiance and viewing/illumination geometry data).

Raytheon

NCC4: Load 2000 (or the remaining unprocessed) rows of radiance, geometry, and detector status data from the SDR the memory.

NCC5: For each pixel in the buffer, do the following steps:

    a) search the path radiance and the reference surface radiance LUTs based on the view/illumination geometry values;

    b) perform path radiance correction by subtracting the pixel radiance value by the LUT path radiance value;

    c) normalizing the radiance by dividing the path radiance corrected pixel radiance by the LUT reference radiance;

NCC6: Perform noise detection and reduction for the buffer using the following steps:

    a) check if the normalized pixel value is great than a threshold. If the pixel value exceeds the threhold, it is considered noisy and the following steps (b) and (c):

    b) search for the neighboring pixels of the current pixel;

    c) calculate the mean value of the neighboring pixels and replace current pixel with the mean (Note that before the mean is calculated, a threshold check is performed to make sure no noisy pixels are used in the calculation of the mean. If all neighboring pixels are noisy, a fill value is set to this pixel).

NCC7: Smooth the boundary between detector stages using the following steps:

    a) find the position of detector stage boundary.

    b) for a given buffer across the boundary (e.g., four pixels), replacing the pixel values in the buffer by the mean value of the buffer.

NCC8: Write the processed pixel to output file and determine if the entire image has been processed. If there are remaining rows to process, go to step NCC4.

3.3.2   Algorithm Input

3.3.2.1   VIIRS data

The algorithm requires the calibrated and geolocated day/night band radiance, the 2-bit detector code specifying the stages, and the corresponding view/illumination geometry data.

3.3.2.2   Non VIIRS data

The algorithm requires a pre-constructed radiance LUT. The LUT should include radiance for a black surface and a reference surface with constant albedo, for all view/illumination conditions that may encounter in the terminator region.

3.3.3   Theoretical Description

3.3.3.1   Physics of the Problem

For decades, merged images (or "photo-mosaics") were produced manually by "cut and paste" methods and by photo-manipulation. More recently, automated methods have been developed that compute the merged image. These methods typically create a new image on a line by line basis. Each line may take data from one image up to a given point; beyond that point, data comes from the second image. The region adjacent to the switchover point is called the "seam".

An unintended feature of photo-mosaicking is the presence of visual artifacts that result from inherent differences between the two images that compose the merged image. The visual artifacts not only introduce potential confusion for the human analyst but can mask features of interest in the original images such as cloud type indicators or ice edge features. If one simply lines up two photos of the same scene taken at different times of day from the same vantage point and then cuts through the pair and tapes the opposite segments from the separate images together, one will immediately notice several artifacts. For example, if the contrast in one image does not match the contrast in the second or one is uniformly darker than the other (histogram mismatch), the human will notice an apparent edge at the seam joining the two halves. This seam is difficult to ignore since the eye responds preferentially to long straight features (e.g., edges, day/night texture changes, etc.).

Generically, artifacts can result from a number of inter-images differences. Some of these are content-related e.g., due to images taken at different times; some are sensor related, e.g., differences in dynamic range; some are platform-related, e.g., misregistration errors; and some result from a combination of content and platform e.g., uncorrected parallax errors. The algorithm must accomplish the seam-finding and image combination in such a way so as to minimize the introduction of artifacts and subsequently must minimize their visual impact.

A further occasion for artifacts occurs due to the special processing required for pixels lying within the solar terminator. For the purposes of this ATBD, we identify the terminator region as the zone that is neither astronomical night nor standard daytime. These pixels may be saturated in the high gain CCD stage while not being fully illuminated in the low gain stage. The choice of grayscale value for the image therefore must maintain available contrast without introducing confusing artifacts or false contrasts.

The NCC EDR does not correspond to a single consistent physical characteristic of the natural environment. The resultant data product is used to provide the analyst an image for visual interpretation. The product is derived from the day/night band SDR which has a separate algorithmic production process that must conform to the system requirements. The requirements that pertain to the NCC EDR instead relate to its usability for manual interpretation.

The NCC EDR must adequately represent the surface and atmospheric (specifically, cloud) conditions across the terminator region to be analyzed without artifacts due to switching detector stages or to the significant radiance difference (in the orders of 1.e06 to 1.e07). The algorithm must completely eliminate any artifacts at the boundary between each stage and bring up the surface or cloud features presented in the entire terminator region.

3.3.3.2 Mathematical Description of the Algorithm

The four general procedures described in section 3.3.2.1 can be expressed using the following:

a) In the terminator region, the radiance of the day/night band (retrieved from the digital number using the calibration coefficients) is resultant from both solar and lunar (and also star and city lights where those sources exist) illumination. The combined radiance can then be expressed as the following:

$$L = L_{sun} + L_{moon} + L_{other} \tag{3.3.1}$$

b) for each part of the radiance components, they can be decomposed to those from atmospheric path and those from the target (surface or clouds):

$$L = L_{sun\_p} + L_{moon\_p} + L_{other\_p} + L_{sun\_t} + L_{moon\_t} + L_{other\_t} \tag{3.3.2}$$

c) the path radiance reduction procedure is to remove the path radiance from the total radiance, i.e., subtract the total radiance by the path radiance simulated from model atmosphere and the resultant radiance becomes:

$$L' = L_{other\_p} + L_{sun\_t} + L_{moon\_t} + L_{other\_t} \tag{3.3.3}$$

Note that path radiance from sources other than the sun and the moon is not removed due to the difficulties in modeling those radiance components.

d) the normalization procedure is to divide this new radiance by the reference radiance of a reference surface, which is derived from model atmospheres with the sun and the moon as illumination sources and path radiance removed:

$$L_{norm} = L'/Lref = (L_{other\_p} + L_{sun\_t} + L_{moon\_t} + L_{other\_t})/(Lref_{sun\_t} + Lref_{moon\_t}) \tag{3.3.4}$$

In the above equation, if there is no other illumination source than the sun and the moon, and if the model atmosphere matches real atmosphere, the L_{norm} value is the same as the ratio of the target albedo to the reference surface albedo. In actuality, the radiance resultant from sources other than the sun and the moon is very small in most circumstances and is negligible as compared to those from solar/lunar irradiance. In addition, the real atmosphere will also not match exactly to the model atmosphere used in the pre-constructed LUT. Therefore, the L_{norm} value is approximately but not exactly proportion to the ratio of the target albedo to the reference surface albedo. The significant radiance difference across the therminator due to illumination irradiance difference is normalized in L_{norm} and the resultant image product will present near constant contrast across the scene.

e) because the ratio method used in the normalization procedure can be sensitive to the noise (i.e., noise can be enlarged due to the ratio procedure), the noise reduction procedure is necessary to detect and minimize noise.

f) The final smoothing procedure is simply an averaging process across the boundary of detector stages.

3.3.4 Archived Algorithm Output

The algorithm output is a visible image at the resolution of the DNB Horizontal Reporting Interval of 742 meters +/- 5%. Figure 12 is a simulated radiance image at the terminator area using the Amazon TERCAT scene provided by the IPO. Due to the significant irradiance change across the terminator, features in the nighttime side of the scene are not visible. Figure 13 shows the output from a prototype of the NCC algorithm given the inputs from Figure 12, for an ideal noise-free sensor input. Performance with real sensor data input is discussed in Section 3.3.5.

Raytheon
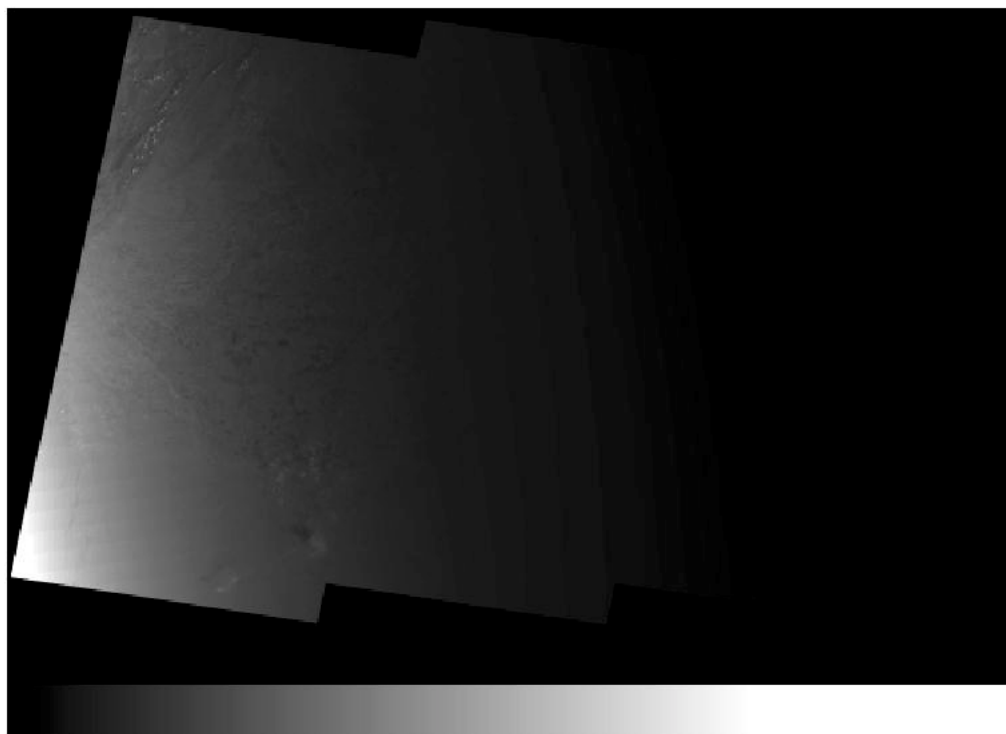
Figure 12. Input radiance image to the NCC algorithm
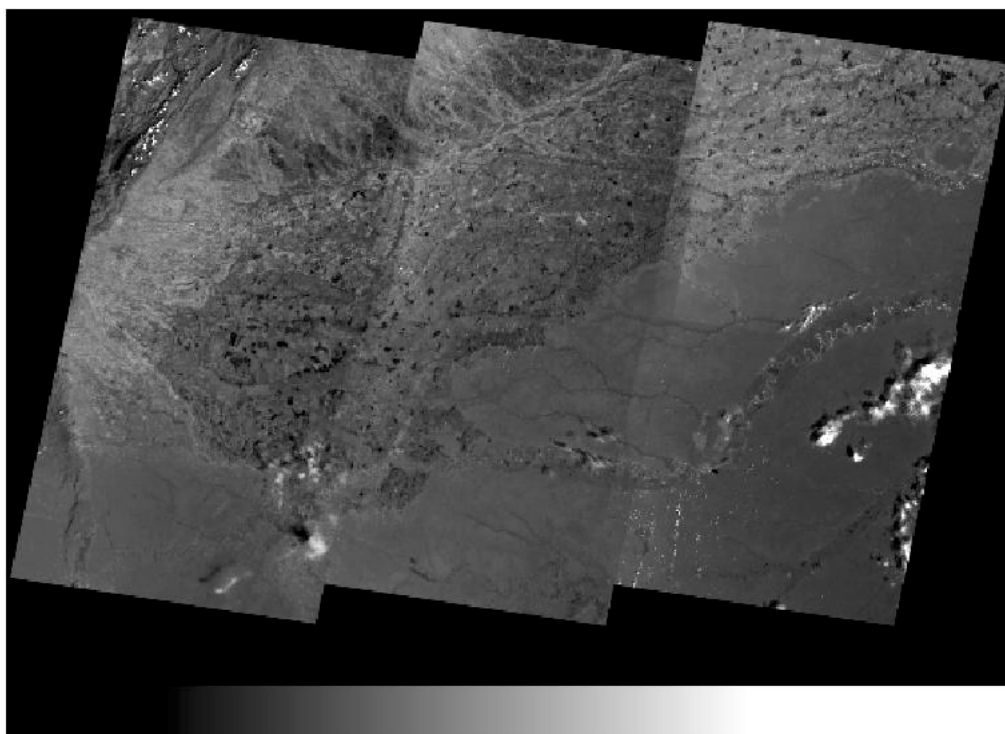
Figure 13. NCC Algorithm Output

3.3.5 Performance of NCC Visible Imagery

The analysis of algorithm performance is based on Modtran 4.0 simulation. When solar zenith angle is greater than 89.0 degrees, Modtran simulation (including version 4.0 and all previous versions) does not produce accurate TOA radiance. That is, the radiance calculated from Modtran is the same for any surface or cloud albedo. Thus, there is no cloud and surface signal in the simulated TOA radiance except for the path radiance which only changes with illumination and viewing geometry at given atmosphere.

For a noise-free simulation, the path radiance is 100% removed using the LUT because the simulated image and the LUT were generated using the same Modtran model. Therefore, when the solar zenith angle is greater than 89 degrees, the solar (path) radiance is completely removed and the retrieved image preserves the cloud and surface contrast. In a real situation, because the solar path radiance cannot be completely removed, the algorithm's performance in the region where solar zenith angle ranges from 90 to 100 degrees will of course not be as good as the simulated result shown in Figure 13.

An improved RT model for the solar zenith angle range between 90 and 100 degrees is required to test algorithm performance on real sensor data. We discuss this matter further in the section on algorithm initialization and validation (Section 3.3.6).

When the solar zenith angle exceeds 100 degrees, the contribution of solar illumination is negligible and the solar path radiance problem is no longer an issue

3.3.6 Initialization and Validation

3.3.6.1 Initialization

The algorithm is based on standard techniques of atmospheric correction and normalization. LUTs will be created from RT simulations, using the best available forward model.

3.3.6.2 Pre-Launch Characterization

Our pre-launch plan is to test the algorithm on unclassified OLS imagery obtained from the National Geophysical Data Center (NGDC), and make any algorithm adjustments which improve the terminator imagery. Algorithm run time performance will be assessed with regard to the requirement to produce NCC Visible imagery in near real time at field terminals.

3.3.6.3 Validation

Following NPP launch, the performance of the algorithm will be tested on VIIRS DNB imagery. The heritage OLS technique can be used operationally at the start of the NPP. If it is determined that our algorithm produces a superior product, it can be adopted as the operational algorithm.

Raytheon

3.3.7 Practical Considerations

3.3.7.1 Numerical Computation Considerations

The intended algorithm runs on image segments corresponding to output of the broad day/night band SDR algorithm. The rectangular block might be as large as 25 million pixels. The size of the path and reference surface radiance Look Up Tables (LUTs) depends on the numbers of geometry nodes and atmospheric models. The actual computation for each output pixel is relatively simple and the total computation time is largely dependent on the size of input data black. There will be a compromise between the number of I/O and the data block size in each I/O. The optimum compromise will be decided on the basis of hardware capabilities at the field terminals.

3.3.7.2 Programming and Procedural Considerations

All procedures are automatic, to perform in the operational environment

3.3.7.3 Configuration of Retrievals

The NCC algorithm expects the VIIRS day/night CCD band SDR and related geometry parameters as input. The output of this algorithm is for analyst manual interpretation and does not serve as quantitative input to any other EDRs. The NPOESS processing configuration is designed to satisfy these expectations.

3.3.7.4 Quality Assessment and Diagnostics

In general, the NCC image should resemble its constituent imagery products. If these products are insufficient to support manual analysis, then the NCC product is unlikely to serve the analyst any better. Thus, if there is little moonlight, then contrast at the terminator and on the dark side will be poor. Sun reflections and glint can also impair human analytic performance. If helpful to analysts, it is possible to flag imagery that might show sun or moon glint.

3.4 MANUAL CLOUD ANALYSIS PRODUCT DESCRIPTION

3.4.1 Processing Outline

Manual cloud analysis products are not produced by the VIIRS operational system. The products are expected to be produced at various locations by trained analysts, using the VIIRS Imagery as input data. Different analysts may wish to use different techniques. Our specifications for the VIIRS sensor have been developed by analysis using the techniques described below, which we refer to as the VIIRS Manually-Generated Cloud Data algorithm (VMCD). An outline of a proposed User's Guide to assist an analyst in implementing the techniques is included as an Appendix to this document.

3.4.2 Algorithm Input

Ancillary data, both VIIRS and non-VIIRS, are useful for manual cloud analysis. We have assessed the relative importance of the various sources of ancillary data. A prioritized list is presented as Table 9.

Table 9.   Ancillary data to augment manual cloud analysis.

Prioritized Item	Application	Utility assessment
1) Cloud mask/ Cloud Cover	Used to speed manual analysis by providing a mostly-correct first guess	Crucial. Manual analysis cannot be accomplished without this. Analysis timelines do not permit analyst to determine the cloud state of every pixel or even horizontal cell individually.
2) Geographic/ physio- graphic data, oceanic currents	Identifies clear-scene structural and textural details for comparison	Very important, but difficult to assess contribution. Analysts have varying degrees of initial geographic knowledge
3) Raw Vis/LLLS/IR imagery (contrast enhanced)	Presents a less processed view of the scene. Processing artifacts, pseudo-colors, etc., are removed, allowing analysts to make an independent assessment of the scene.	Important but difficult to assess contribution. Perform manual cloud analysis with and without these data using different teams of analysts; compare results to ground truth [Manual comparison method]
4) Cloud Mask diagnostics (TBR)	Flags which indicate whether ambiguous results occurred from the several cloud tests. Manual attention concentrates on these locations	Will be important but difficult to assess contribution. Perform manual cloud analysis w/ and w/o, compare results to ground truth
5) Snow/Ice fields	Draws analyst attention to suspect snow/ice areas for confirmation.	Important. Manual comparison method
6) Conventional Surface observer cloud reports from nearest hourly/synoptic time	Provides independent on-the-spot assessment of cloud conditions	Less important. Manual comparison method
7) Aerosols	Analyst can judge whether imagery effects are from clouds or aerosols	Less important. Manual comparison method
8) Cloud Top T, p, z	Could be of use but is likely to overload an already stressed	Given a reliable product this could take on

Raytheon

Prioritized Item	Application	Utility assessment
	analyst. Would be better to design one product that would roll this and the next three items together and ideally merge with cloud mask.	greater importance.
9) Optical depth, EPS	See Cloud Top T, p, z	See Cloud Top T, p, z
10) CMIS soundings	See Cloud Top T, p, z	See Cloud Top T, p, z

It is important to not overwhelm an analyst with an abundance of information. Manual cloud analysis accuracy is not the bottleneck. Decreasing the amount of time required to review and correct the automated analysis to a given level of accuracy is more important than further increasing accuracy, once the objective performance level is met. Additional information can greatly decrease manual analysis throughput. Cloud analysts are generally mass producers, not craftsmen or artisans.

Given that, we could focus our thoughts on a "new" product that would synthesize many of the items presented in the table into one product that could be easily used by an analyst to improve his analysis.

3.4.2.1 VIIRS Data

The VMCD algorithm requires SDRs for each VIIRS imagery channel and several imagery assist channels. The imagery SDRs are the daytime/nighttime visible band, the 0.645 μm daytime visible band, the 3.74 μm band, and the 11.45 μm IR band. The imagery assist channels include the 0.412 μm, 0.858 μm, 1.38 μm, 1.61 μm, 4.05 μm, 8.55 μm, and the 10.8 μm bands. It is assumed that these data are accurately calibrated, earth-located, and co-registered.

3.4.2.2   Non-VIIRS Data

AFWA has two major functions that use VIIRS capabilities to generate cloud data (1) QC, Bogus of the cloud data base, discussed in Section 2.3.1, and (2) contingency support, e.g. understanding the contents of a scene -- e.g. Kosovo. Ancillary data requirements for both functions include:

a.   Automated cloud analyses (cloud cover, cloud top height, etc.)

b.   Surface type maps (geography) of area covered by imagery

c.   Surface elevation and terrain maps

d.   Conventional weather observations as available (surface reports, aircraft reports, and radiosonde observations)

3.4.3   Theoretical Description

3.4.3.1   Physics of the Problem

The ability to manually identify clouds in any given spectral band is based upon the contrast, measured in radiance, between the cloud and the surrounding cloud-free background. More precisely:

$$C = I_V(0)_{cloud} / I_V(0)_{background}$$
(3.4.1)

The measured or satellite observed radiance, $I_v(0)$, may be composed of reflected solar radiation and resultant albedos, thermal radiation emitted by or brightness temperatures of the terrestrial feature, or both when observations are made in the 3-5 micron wavelength interval.

The monochromatic, upwelling infrared radiance measured at the sensor aperture in a cloud-free atmospohere is given by (Liou, 1980, p. 247):

$$I_v(0) = \varepsilon_v B_v\left[\mathsf{T}_s\right]T_v(p_s) + \int_{p_s}^{0} B_v[\mathsf{T}(p)]\frac{\partial T_v(p)}{\partial p}\,dp + (1-\varepsilon_v)\int_{0}^{p_s} B_v[\mathsf{T}(p)]\frac{\partial T_v(p)}{\partial p}\,dp$$
(3.4.2)

and:

v	= wavenumber of emission
$B_v\left[\mathsf{T}(p)\right]$	= Planck function at wavenumber (v) for temperature (T)
ε_v	= emissivity of surface at wavenumber (v)
$T_v(p_s)$	= atmospheric transmittance between pressure level (p_S) and space
$I_v(0)$	= monochromatic radiance arriving at satellite.
p_s	= surface pressure
T_s	= surface temperature

For imaging sensors, the atmospheric transmittance between pressure levels and space is very small and Equation 3.4.2 is closely approximated by Equation 3.4.3, which shows that the radiance arriving at the satellite sensor is a function of the emissivity of the surface, the surface temperature, and the transmission from the surface to the sensor:

$$I_v(0) = \varepsilon_v B_v\left[\mathsf{T}_s\right]T_v(p_s)$$
(3.4.3)

Thus, the capability to manually detect a cloud in infrared imagery is enhanced not only by temperature contrasts between the features but also by observing the features in spectral bands where there emissivity contrasts exist or in bandpasses which effect atmospheric transmissivity as is the case with the 1.378 micron channel which suppresses the signatures of low-level features, including clouds and cloud-free surface thus enhancing the signatures of higher level clouds.

The amount of solar radiation reflected by the Earth-atmosphere system into the sensor aperture is given by (Liou, 1980, p. 25):

$$I(0;\mu,) = I\left(\tau_{1;\mu,}\phi\right)^{-\tau_{1}/\mu} + \int_{0}^{\tau_{1}} J(\tau';\mu,\phi)e^{-\tau_{1}/\mu}\frac{d\tau'}{\mu},$$ (3.4.4)

Term A   Term B

where:

$I_{v}(0)$	= monochromatic radiance arriving at satellite
τ	= optical depth of each τ' layer, while the atmosphere is τ_{1} thick
Term A	= surface energy contribution attenuated to space
Term B	= internal atmospheric contributions attenuated to space
μ	= cosine of angle between radiation stream and local zenith angle
ϕ	= azimuth angle.

The complexity of this calculation lies in the source function term, $J(\tau;\mu,\phi)$, which is given for solar radiation by Equation 3.4.5.

$$J(\tau;\mu,\phi) = \frac{\tilde{\omega}}{4\pi}\int_{0}^{2\pi}\int_{-1}^{1} I(\tau;\mu',\phi')P(\mu,\phi;\mu',\phi')d\mu'd\phi'$$ (3.4.5)

Term C

$$+\frac{\tilde{\omega}}{4\pi}\pi F_{0}P(\mu,\phi;-\mu_{0},\phi_{0})e^{-\tau/\mu_{0}}$$

Term D

where:

Term C	= multiple scattering of diffuse (scattered) energy
Term D	= single scattering of direct solar irradiance, F_{O}.

and:

ω	= single scattering albedo
P	= phase function
F_{0}	= solar irradiance
μ_{0}	= cosine of solar zenith angle
ϕ_{0}	= solar azimuth angle

Thus, the capability to manually detect a cloud in visible and near-infrared imagery is enhanced by viewing in spectral bands where contrasts in the reflectivities of the features are known to exist.

In reality, monochromatic radiation does not exist because of line broadening from natural, pressure (collision), and Doppler (thermal velocity) effects. Also, since an instrument can distinguish only a finite bandwidth, the upwelling radiance measured by the satellite is integrated

over the sensor transmission filter, which is also called the sensor response function, and is given by Equation 3.4.6.

$$I_v(0) = [\int_{v1}^{v2} I_v(0)\phi_v dv] / \int \phi_v dv \qquad\qquad (3.4.6)$$

where:

ϕ_v = filter (sensor) response function at wavenumber (v)

v_1, v_2 = wavenumber range of filter response

3.4.3.2   Image Processes to Enhance Cloud Detection in Multispectral Imagery

The manual interpretation of clouds and background features in multispectral imagery is facilitated by the use of false color composite images which are made by assigning a different spectral band to each gun of a CRT (d'Entremont *et al.*, 1987). The hue of the false color composite emphasizes the gun in which the feature has the strongest signature, i.e., has the larger radiance arriving at the satellite sensor. Equal contributions from each channel in the CRT results in a feature appearing as a (white through black) gray shade in the false color composite, with the shade of gray depending upon the strength of albedos or brightness temperatures of the feature in the spectral bands.

In current operational AVHRR imagery, the signature of vegetated land is more pronounced in the 0.9-μm channel than the 0.6-μm band while water clouds are similar in both the 0.6-μm and 0.9-μm channels as seen in Panels A(1) and A(2) in Figure 14, respectively. Thus, a false color composite of the scene shown in Panel A(3) shows highly vegetated areas in green, less-vegetated areas as brown, and clouds as white (Hutchison *et al.*, 1997). In addition, the land-sea boundary is seen distinctly in the color composite since the land near the ocean's edge is densely vegetated while the ocean has a low albedo in both spectral bands.

Additional false color composites can be created to emphasize other features in the scene. For example, high water clouds may be differentiated from lower-level water clouds by including 3.7-μm and/or the 12.0-μm infrared bands shown in Panels A(1) and A(2), respectively in Figure 15. This process is demonstrated in Panel A(3) where the 0.6-μm image assigned to the blue gun in Figure 14 has been replaced with the 12.0-μm channel. Colder clouds appear bluish in the composite in Panel A(3) of Figure 15 while warmer clouds have a yellow-greenish hue.

Care must be taken using this false color composite to avoid misclassifying optical thin, cirrus clouds as lower-level clouds. This is accomplished using another color composite described in Figure 16. First, a method is described to differentiate between snow and water clouds in daytime imagery.

The contrast between snow and water clouds is greatly enhanced by including the 1.6-μm channel in the false color composite, since water clouds are highly reflective in this band while snow and ice (clouds) reflect poorly (Valovcin, 1978). Alternatively, the reflectively of snow in the 3.7-μm band is also very small and can be used to simulate the signatures in a 1.6-μm channel

Raytheon

by removing the thermal component of the radiation from the observed satellite radiances (Hutchison *et al.*, 1997; Allen, Durkee, and Walsh, 1990) to create an image which facilitates the manual distinction between snow and water clouds as shown in Figure 16.

A benefit of using the 3.7-μm albedo channel, rather than the 1.6-μm imagery, to manually discriminate between snow and water clouds is that the former simultaneously enhances the contrast between snow and thin cirrus clouds as well as the contrast between water clouds and snow. In fact, the spectral signature of optically thin cirrus in the derived 3.7-μm albedo image is actually enhanced over that present in the 12.0-μm imagery (Hutchison *et al.*, 1997) as seen in Panels A(1) and A(2) of Figure 17.

A(1)

A(2)
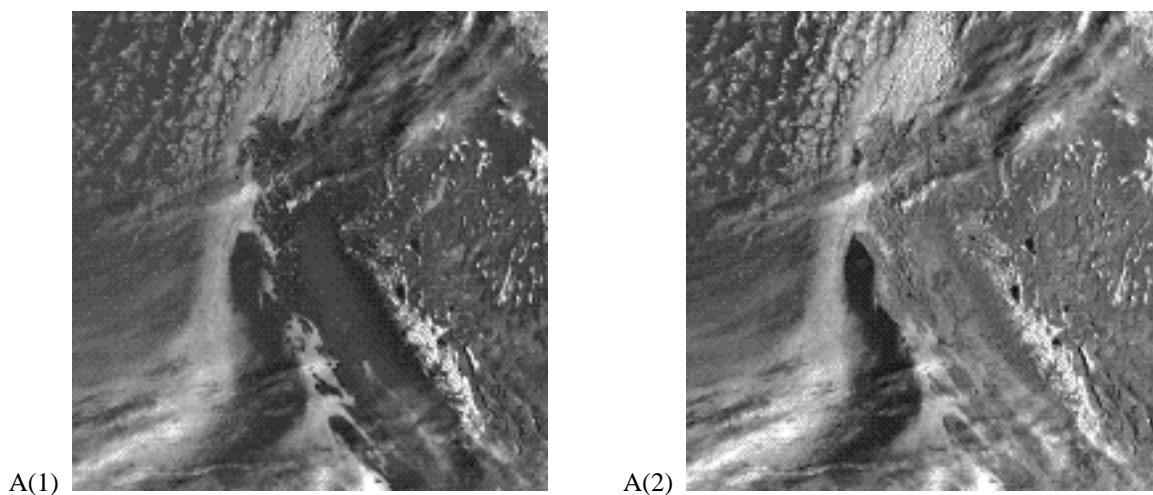
Panels A. Highly reflective snow and water clouds are visible in AVHRR Channel 1, A(1), while coastline and inland lakes become more discernible in Channel 2, A(2). Snow is bright in both channels.

A(3)
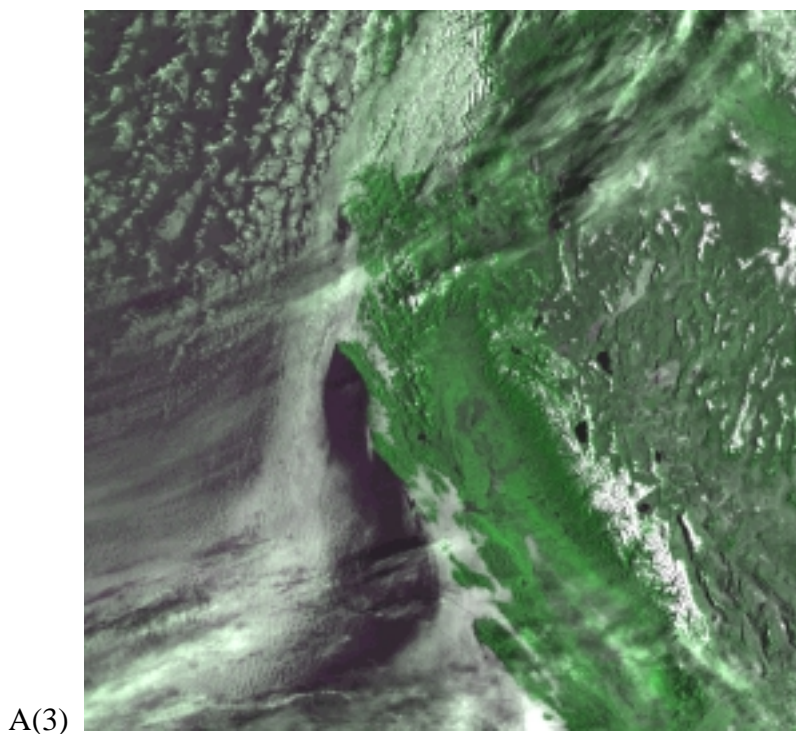
Panel A(3). False color composite of NOAA-12 AVHRR imagery shown was created by assigning Channel 1 to the red and blue guns and Channel 2 to the green gun of a CRT. This false color composite is useful for manually distinguishing between densely vegetated (rich green hue) and more sparsely vegetated (brownish hue) land as well as the water-land boundaries. Snow and clouds both appear bright in this color composite.

Figure 14. NOAA-12 AVHRR Channel 1 and Channel 2 imagery collected over western U.S. at 1505 GMT on March 19, 1996.

Raytheon

A(1)   A(2)
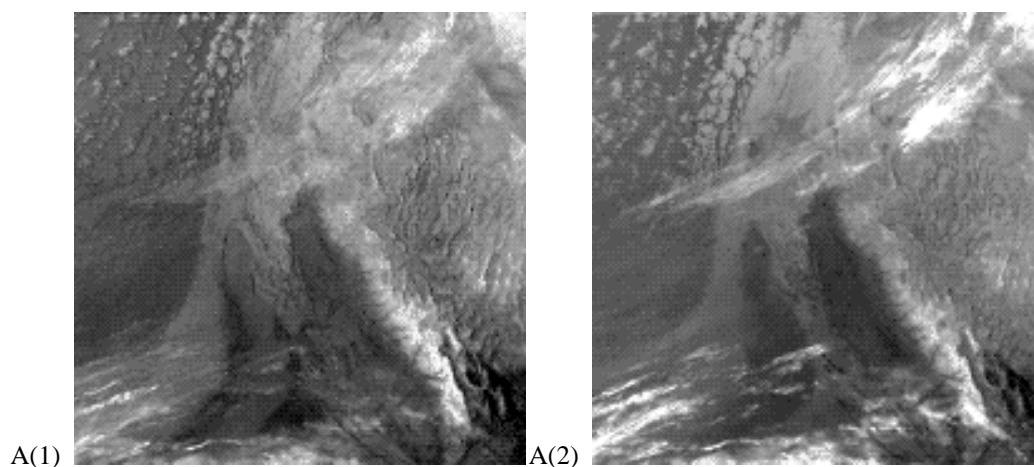
Panels A. Ice clouds and snow along the Sierra Mountain range, lower right quadrant, have a similar (bright) appearance in AVHRR channel 3, A(1), and channel 5, A(2), which makes distinguishing between them difficult.
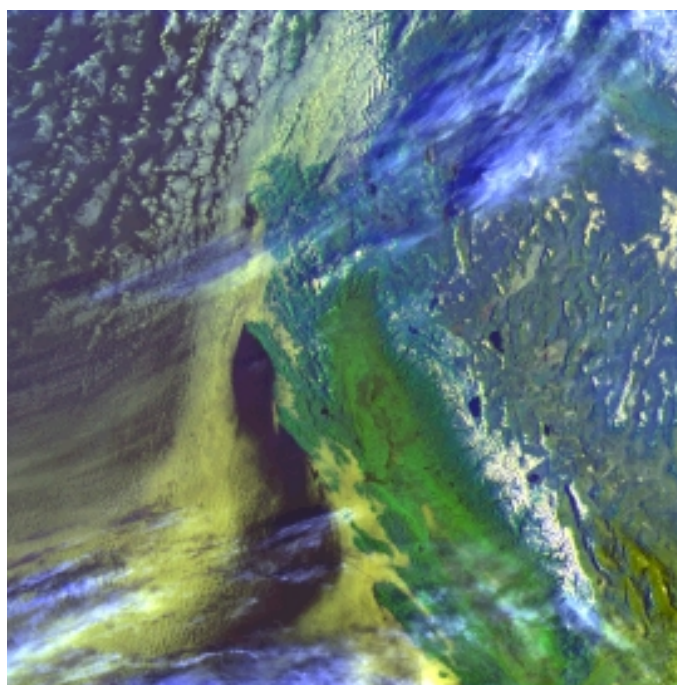
Panel A(3). The false color composite in A(3), created by assigning AVHRR Channel 1 to the red and blue guns and Channel 2 to the green gun of a CRT, is used to manually distinguish between densely (rich green hue) and more sparsely (brownish hue) vegetated land as well as the water-land boundaries. Snow clouds both appear bright in this color composite.

Figure 15. NOAA-12 AVHRR Channel 3 and Channel 5 imagery collected over western U.S. at 1505 GMT on March 19, 1996.

A(1)   A (2)
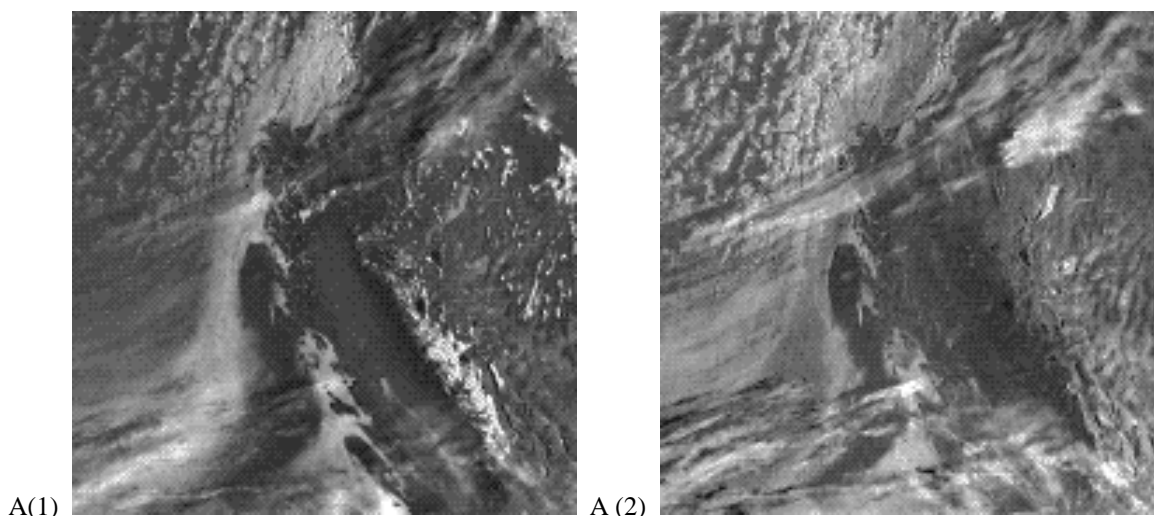
Panels A. The contrast between snow is greatly enhanced by correcting the 3.7-μm band for thermal emissions as seen by comparing the 0.6-μm band, A(1), with the 3.7-micron albedo data in A(2), and the brightness temperature difference image of channel 3 minus channel 5, C(2).

Figure 16. NOAA-12 AVHRR Channel 1 and the derived 3.7-μm (albedo) data for the scene collected 1505 GMT on March 19, 1996.

Panels A. The false color composite in A(1), created by assigning AVHRR Channel 1 to the red, the derived Channel 3a (albedo) to the green, and Channel 5 to blue gun of a CRT while Channel 3 replaces Channel 3a in A(2).

A(1)   A(2)
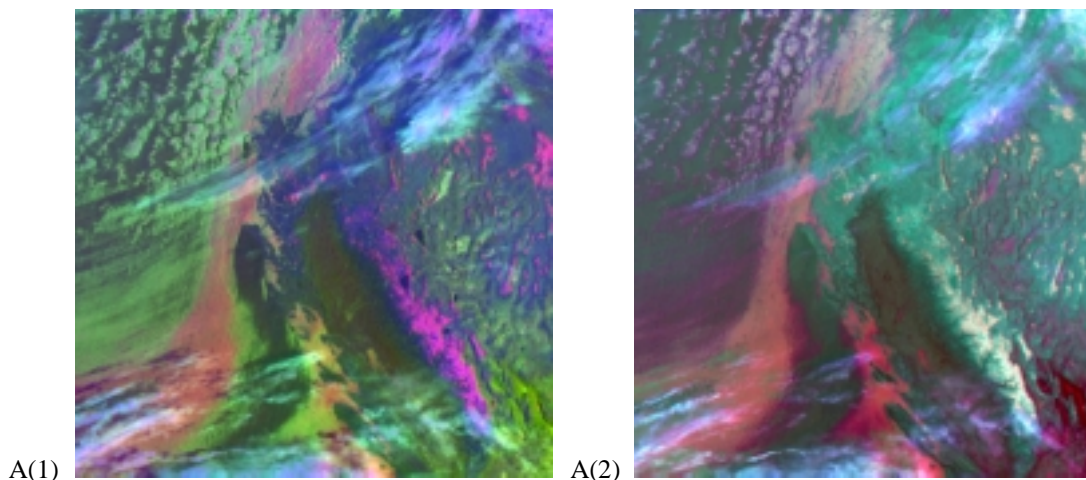
Figure 17. Color composite of NOAA-12 AVHRR imagery created by assigning Channels 1, 3, and 5 to the red, green and blue guns of a CRT.

The enhanced spectral signatures in channel 3a (albedo) greatly assist in manually distinguishing between ice clouds (blue) and snow (purple) in Panel A(2) of Figure 17. The clear distinction between thin cirrus and the snow-covered mountains in the lower-right quadrant results from the spectral signatures of these features being very different in channels 1, 3a, and 5. In fact, it was found that the signature of snow in Panel A(1) of Figure 17 from the red and blue guns was

nearly an order-of-magnitude greater than its signature in the green gun; thus, snow appears purple in the false color image, indicating nearly equal energy coming from the red and blue guns (channels 1 and 5). On the other hand, the signature of snow in Panel A(2) from the red, green, and blue guns is nearly the same for channels 1, 3, and 5; since equal contributions from each gun produces a gray shade rather than a color, snow appears white in this figure. Thin cirrus appears bluish in both panels because ice has its strongest signature in channel 5. However, it is important to note that more thin cirrus is evident in Panel A(1) than A(2) because the signature of thin cirrus in the combination of channel 3a and channel 5 is greater than its signature in channel 3 and channel 5. Finally, the large difference in the signature of snow between channel 3a and channel 1, shown in the false color composite of Panel A(1), means it is possible to positively identify snow-covered surfaces using an automated algorithm based upon the bi-spectral reflectance ratio between these two channels. It appears that the low clouds in Panel A(1), shown as red and occurring in the left half of the image, have a similar spectral signature to that of snow and therefore could be misclassified; however, this is not the case. In channel 3a, the spectral signature of snow is much weaker, by a factor of nearly 5, than the signature of low-level water clouds. In addition, the relative signature of warmer, water clouds is only slightly larger in channel 1 (the red gun) than in channel 5 (the blue gun) and this difference becomes smaller as the cloud tops become colder, i.e. the clouds change from low to middle level clouds. On the other hand, while the spectral signature of snow is much lower in channel 3a (the green gun) than the channel 1 (the red gun), it is even lower when compared to channel 5 (the blue gun) since snow-covered surfaces appear cold in channel 5. Thus, the channel 1, 3a, and 5 false color composite is a robust display for the manual identification of snow and thin cirrus in multispectral imagery (Hutchison *et al.*, 1997; Hutchison and Locke, 1997). Therefore, the threshold requirements for manual cloud detection and cloud typing in daytime imagery are satisfied using only the DV, MWIR, and LWIR imagery bands along with image processing techniques. The performance summary is provided in Section 3.4.4.

3.4.3.3 Mathematical Description of the Algorithm

The most important step in creating the manual CNC analysis is the accurate interpretation of all cloudy and cloud-free features in the multispectral images using (1) image enhancement techniques and (2) false color composites as previously described while (3) following guidelines that are well documented in the literature (Scorer, 1990). Once these features are identified, the manual cloud-no cloud (CNC) analyses is created from the analysis of individual bands of the multispectral imagery where these features, included edges, are most distinct. The CGTA software allows analysts to compare the spectral signatures of clouds and cloud-free surfaces in all spectral bands and use iterative techniques over subimage regions to create CNC analyses. Individual CNC analyses may be created from a single band or composited from as many as five spectral bands into a total CNC analysis. The operator may draw polygons around areas of interest in each channel and set threshold levels for declaring pixels in that area cloudy; thus, the need for strong contrasts between clouds and background features becomes apparent. Additionally, a composite (total cloud) analysis from one set of five channels for a scene can be updated with CNC analyses of another five bands of the same scene, e.g., if working with hyperspectral imagery, to extend the total CNC analysis to include all clouds in 10 spectral bands and so forth. Thus, in theory, there is no limit to the number of spectral bands that may be used to create the manual CNC analysis; however, in practice, only a couple bands are needed for skilled

analysts to interpret features in a scene and create the manual CNC analysis with a repeatability of about 1-2 percent. Additionally, the accuracy of the manual CNC analysis is limited by image quality, i.e., clouds with a horizontal spatial resolution finer that the sensor optics may not be included in the manual analysis. Cloud Type ground truth (cirrus, stratus, cumulus) will be accomplished in a similar manner using only the areas already declared cloudy in the composite CNC mask as described in Hutchison *et al.* (1997).

3.4.3.4   VIIRS Imagery and Imagery Assist Color Composites

The Raytheon VIIRS design calls for a flowdown of imagery "sensing" requirements necessary to meet threshold Application-Related Requirements for the Imagery EDR. A minimum of three imagery channels are required to satisfy threshold requirements for the Manually-Generated Cloud Data (Hutchison, 1998). These are the daytime visible (DV) band, the Mid-Wave Infrared (MWIR) band, and the Long-Wave Infrared (LWIR) band.

Our VIIRS design also calls for imagery assist channels to be used with imagery channels to push toward NPOESS VIIRS Objectives. In the case of the Manually-Generated Cloud Data, this is readily accomplished using (1) false color composites and (2) the CGTA software concepts. The Imagery Risk Reduction Plan identifies the attributes of each Manually-Generated Cloud Data ARP for which pushing toward objective requirements is feasible (Hutchison, 1999). The performance summary for the Manually-Generated Cloud Data Product ARPs is provided in Section 3.4.4.

This section identifies the color composites recommended for the manual analysis of cloud cover and types with VIIRS imagery and imagery assist bands and discusses the colors present in the color composites. The approach assumed is one of "peeling an onion" in which information about the scene is gained incrementally as more VIIRS channels are used in color composites. While this approach may not ultimately be used in the time-constrained environment of a weather central, it is useful for training analysts in the interpretation of multispectral satellite meteorology. Training programs that incorporate imagery and the identification of cloud ARPs are recommended, although not included here due to the size of these color imagery files based upon MAS data.

The generation of these color composites was done with MAS imagery. The methodology was discussed in the Imagery TIM. This methodology is depicted in Figure 18.
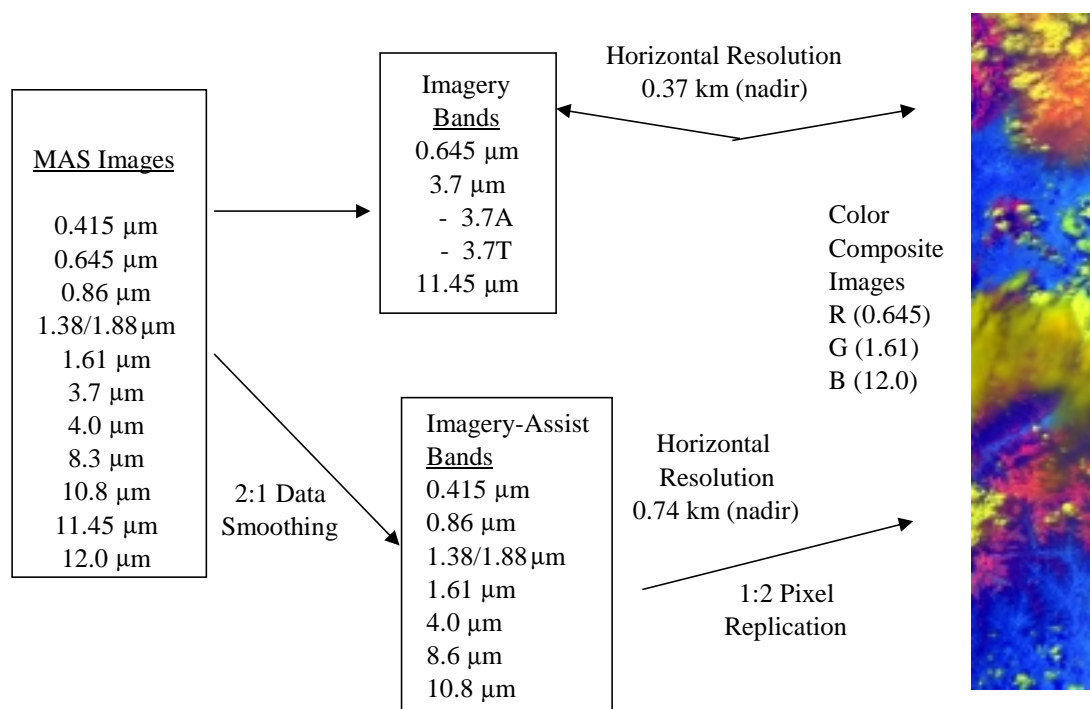
Figure 18. Methodology illustrated in using MAS data to construct Color Composites using Imagery and Imagery Assist bands.

VIIRS bands at 0.86 and 1.6 µm are also available at the fine resolution of the imagery bands. The analyst can use these with unsmoothed imagery bands to obtain some RGB color composites at imagery resolution.

Initially the MAS bands most spectrally similar to VIIRS were considered with Reflectance determined for the Solar and NIR bands and BT's determined for the Thermal and crossover region bands. The imagery bands underwent no data smoothing, while the imagery assist bands went through 2:1 data smoothing. The final bandset used in the Color Composite generation was decided based upon the spectral information content of the bands used, and what distinct spectral features the cloud analyst wished to from the imagery. Note, this methodology is usable by VIIRS due to the spectral similarities which exist between the VIIRS and MAS/MODIS bandsets.

Eighteen color composites were constructed from the VIIRS bandset after a careful survey of the spectral information content. All 18 Composites are included in Appendix B. Eight of these are discussed in this section.

1.   Daytime Composite #1 - RGB (0.645, 1.61, 10.8./11.45): Figure 19

A traditional RGB composite which highlights a rich array of cloud and surface detail.

Feature Identification: Highlight differences between water clouds and snow

–Snow is rose - purple

–Low clouds are yellow;

–Higher (water) clouds range from yellow through green to light blue as the cloud temperature decreases.

Assists in separating low, middle, and high-level water clouds as an cloud typing objectives

Ambiguities: Cirrus and snow are similar but can be differentiated
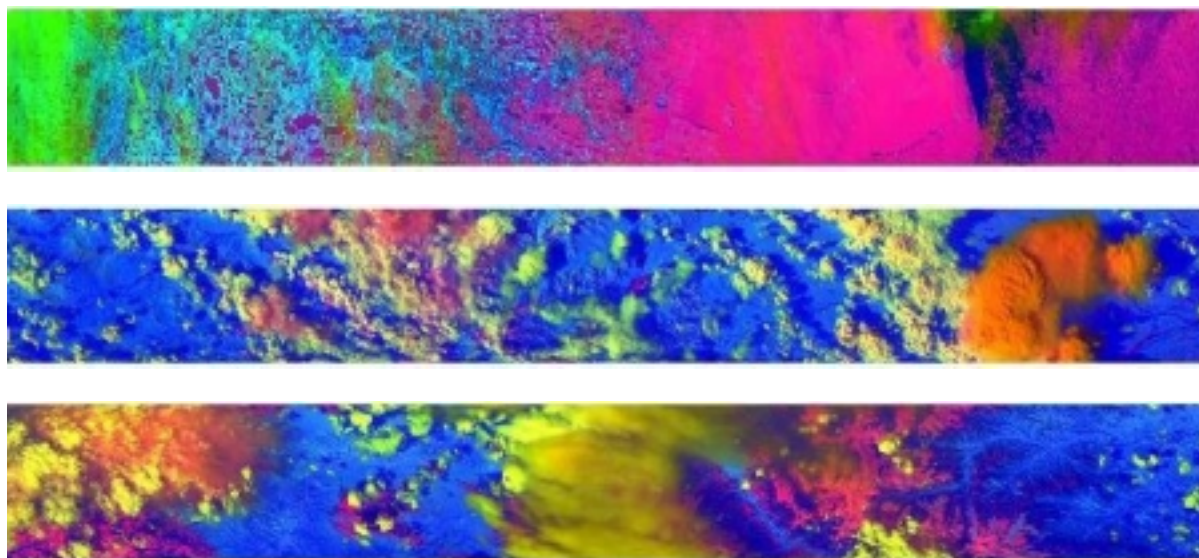
Figure 19. RGB Composites of bands (0.645, 1.61, 10.8./11.45)

2. Daytime Composite #2 - - RGB (1.38[1.88], 1.61, 11.45): Figure 20.

This composite brings out additional detail.

Feature Identification: Clear Distinction between cirrus and snow/ice fields

– Snow/ice fields are masked in 1.38 μm imagery

– The 11.45 μm imagery channel provides useful information on cloud top temperatures, when coupled with the 1.38 μm channel can be used to differentiate between cirrus and other cloud types

– Optically-thin cirrus has a deep bluish hue

– Lower-level water clouds appear greenish

– Optically thick cirrus are more golden and in some cases purple

– Overshooting tops, e.g. thunderstorms, appear orange or white-lavender (objective requirement)

Ambiguities: Little detail on snow and surface features, This composite may not provide great detail on cloud top temperatures, i.e. cloud heights, if large temperature variations exist in the scene.
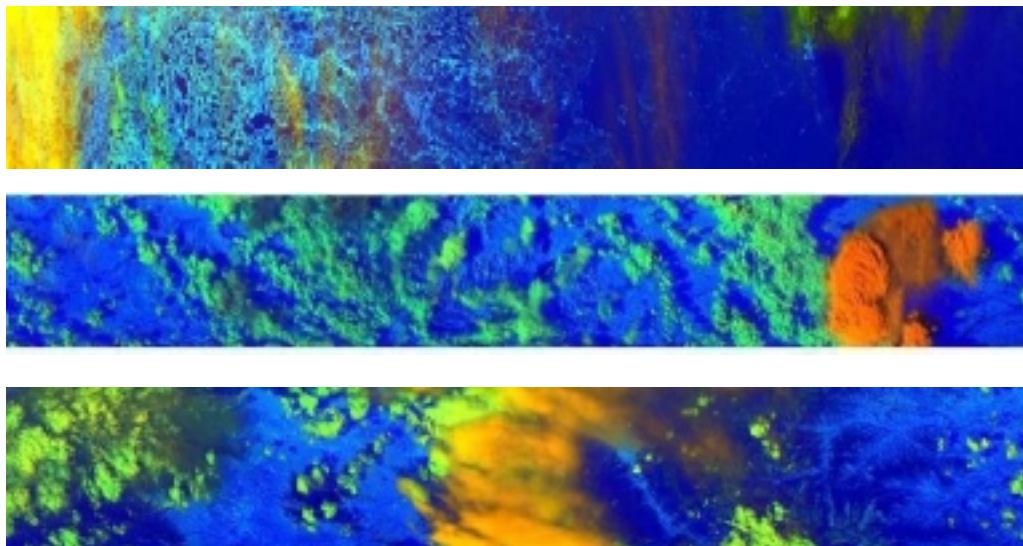
Figure 20. RGB Composites of bands RGB (1.38[1.88], 1.61,11.45)

3. Daytime Composite #3 - - RGB (1.61, Invert BT8.6, 0.645): Figure 21.

This composite brings out additional detail.

Feature Identification: Distinction between lower level Cumulus and upper level Cirrus and snow/ice fields

- Snow/ice fields are blue from 0.645 µm imagery

- Optically-thin cirrus has a greenish - turquoise hue due to contribution emissions at 8.6 µm

- Lower-level water clouds are rose to white

- Overlaying water clouds are darker blue

Ambiguities: Cirrus and snow may in some cases be the same color
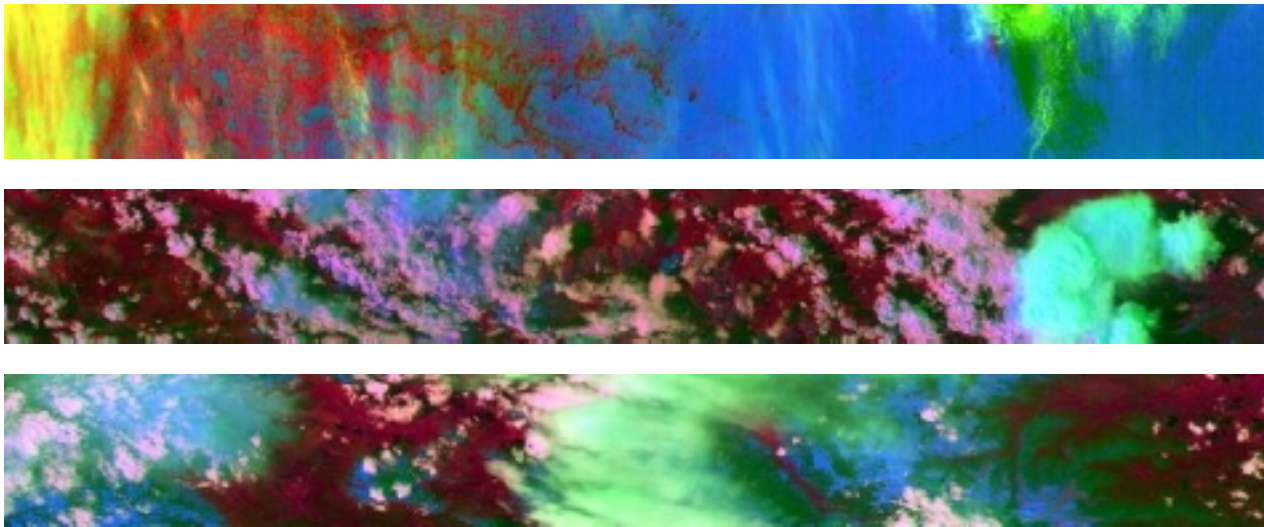
Figure 21. RGB Composites of bands RGB (1.61, Invert BT8.6, 0.645)

4. **Day/Nite Composite #4** - RGB (BT11.45, BT8.6, BT3.75): Figure 22

This composite brings out additional detail.

Feature Identification: Distinction between lower level Cumulus and upper level Cirrus and snow/ice fields

    – Snow/ice fields are olive-green from Thermal imagery

    – Optically-thin cirrus has a deep blue-blackish hue over land and blue over ice

    – Lower-level water clouds appear dark blue

    – Vegetated regions tend to be white

    – Overshooting tops, e.g. thunderstorms, appear black with dark clearly defined boundaries, and cellular structure clearly visible (objective requirement)
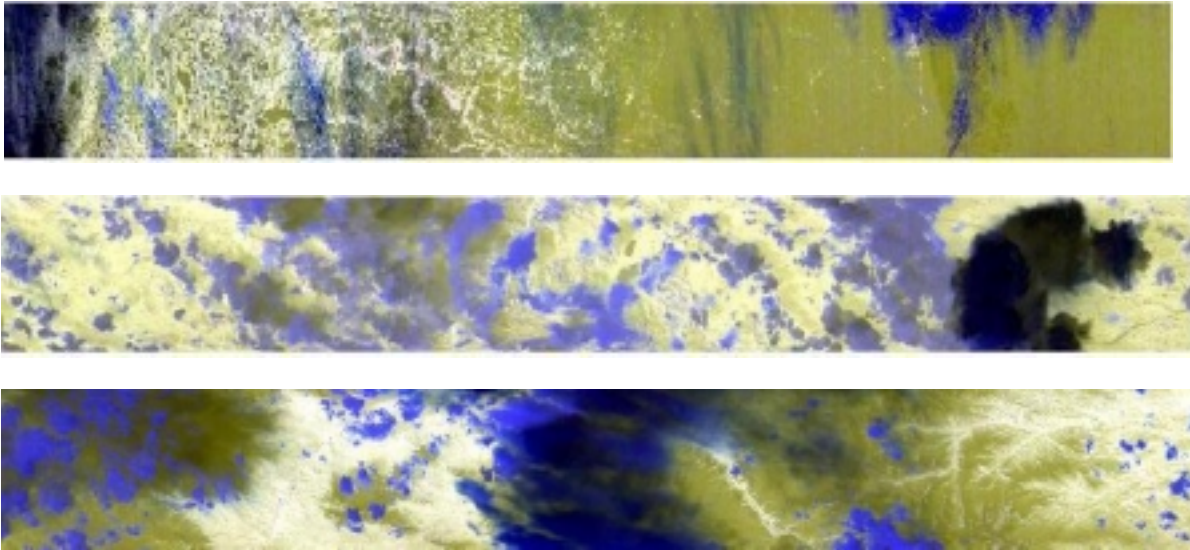
Figure 22. Day/Nite Composite #4 - RGB (BT11.45, BT8.6, BT3.75)

5.   Daytime Composite #5 - RGB (0.645, 0.858, 0.645), Figure 23.

Feature Identification: This is the well-known color composite design to highlight "vegetation" because vegetated regions are more highly reflective in the longer wavelengths which makes these regions appear "green" in the false color composite. Separation of land and water surfaces is also readily accomplished with this composite which uses the 0.645 μm imagery channel with the 0.858 μm imagery assist channel..

Ambiguities: Several features appear gray shaded in this composite and might be ambiguous. For example, snow, water clouds, and non-vegetated regions may all appear as a shade of gray with snow and clouds being particularly difficult to separate.
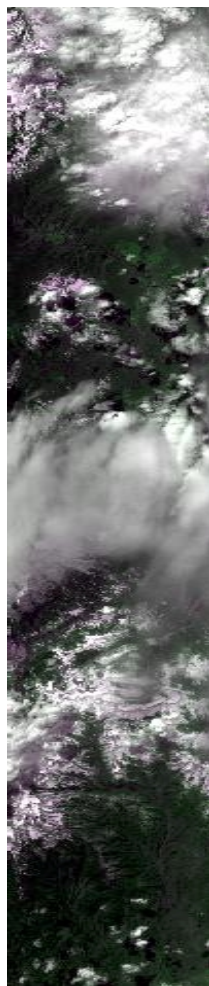
Figure 23. Color composite of MAS data collected over Denver, CO [RGB= (0.645 μm, 0.858 μm, 0.645 μm)].

6.   Daytime Composite #6 - RGB (0.645, 1.61, 10.8), Figure 24.

Feature Identification: This is a relatively new color composite design to highlight differences between water clouds and snow in newly acquired data from NOAA-15. The process renders the snow and ice white and most other surface features in natural colors. Low clouds are yellow; higher clouds range from yellow through green to light blue as the cloud temperature decreases. This composite assists in separating low, middle, and high-level water clouds as an cloud typing objective.)

Ambiguities: Differentiation between snow/ice and cirrus clouds may be difficult, especially when they are approximately the same temperature in the 10.8 μm imagery channel, since these clouds are relatively transparent in the 0.645 μm imagery band, and both reflect poorly at 1.61 μm imagery assist channel.   (These data were taken from the NOAA website at http://www.osei.noaa.gov/Events/Snow/NOAA15new for the grtlks.jpg example. Cirrus clouds are evident along with snow south of Lake Michigan but both appear white.)
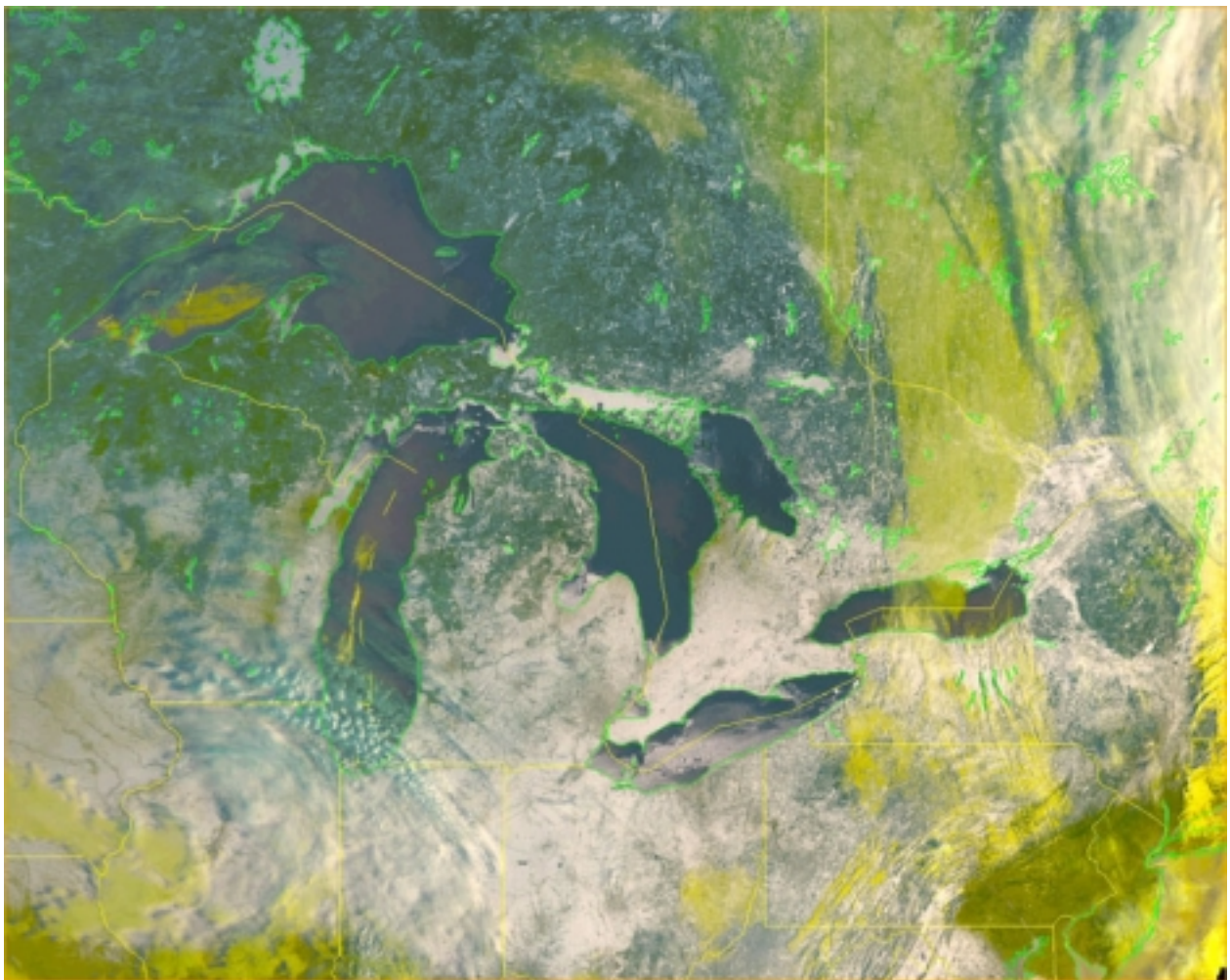
Figure 24. Color composite of NOAA-15 AVHRR imagery created by assigning the 0.645 μm, 1.61 μm, 10.8 μm channels to the red, green and blue guns of a CRT.

7. Daytime Composite #7 alternative - RGB (0.645, 1.61, 3.75 albedo), Figure 25a.

Feature Identification: This color composite is also designed to highlight differences between water clouds and snow but provides better differentiation between optically-thin cirrus clouds and snow/ice since the 3.75 μm albedo imagery channel has the appearance of a 3.75 μm minus 10.8 μm brightness temperature difference fields. Therefore, the cloud/cloud discrimination is more accurate. Vegetated land appears green, snow fields are red, optically thick clouds appear yellow to white, while optically thin water (edges) clouds appear bluish. Thin cirrus clouds appear a deep orange because their signatures is more strongly suppressed in the 3.75 μm albedo band than in the 1.61 μm imagery assist channel while thick cirrus appears reddish since it is highly reflective in the 0.645 μm imagery channel while nearly equal in the other two channels.

Ambiguities: This composite provides no information on cloud top temperatures as does the RGB (0.645, 1.61, 3.75) since the process renders the snow and ice white and most other surface features in natural colors. Care must be taken in this composite since the 3.75 μm channel measures optical thickness, not temperatures. Therefore, edges of a stratocumulus cloud, for example, may be a different color than pixels located at center of the cloud.

8. Nighttime Composite #9 - RGB (3.75, 10.8,11.45), Figure 25b.

Feature Identification: This is the well-known color composite design to highlight stratus clouds (which appear reddish due to their lowest emissivity in the 3.75 μm imagery) and optically-thin cirrus clouds, which appear bluish due to their coldest temperatures in the 11.45 μm imagery channel.

Ambiguities: This composite may not provide great detail on cloud top temperatures, i.e. cloud heights, if large temperature variations exist in the scene.

Raytheon
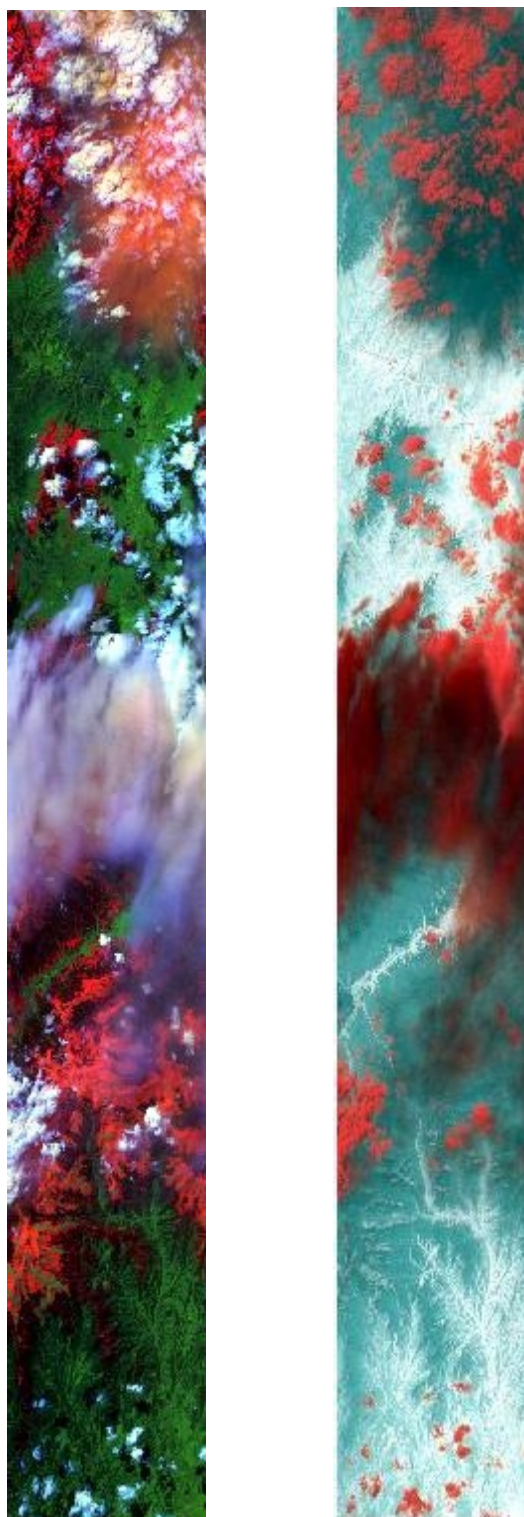
Figure 25 (a.) Color Composite of MAS imagery over Denver, CO [RGB (0.645, 1.61, 3.75 albedo0] (b.) [RGB (3.75, 10.8,11.45)]

Generation of these RGB composites greatly assists the manual analyst in determining cloud type and also to increase confidence in the cloud cover determination. Use of RGB composites will result in fewer Quality Control (QC) bogus operations and assist the manual cloud analyst in determining cloud type for many of the objective cloud types. The biggest improvement will be in the fact that the manual analyst will have improvements in meeting critical time schedules by using RGB composites.

The Raytheon VIIRS team has identified the need for a "VIIRS User's Guide" for the interpretation of imagery as a post-PDR activity and has developed the structure of this publication. It is needed because:

Current OLS & AVHRR sensors are spectral content limited. Analysts using these data are accustomed to "seeing" clouds and different backgrounds in only five spectral band.   VIIRS extends MODIS a leap forward into an operational context. MODIS contains 36 spectral bands but these data are only used in a research environment. VIIRS will provide all the value of MODIS for manual cloud analyses but these data will be provided in the operational environment within a 20 minute time frame.

Algorithm technology and user knowledge must be brought forward to fully realize value of true multispectral VIIRS measurements. The VIIRS automated cloud analysis algorithms exploited the spectral signatures of these data to generate the cloud cover product. It is therefore essential that those who perform manual quality control of these automated products be expert in the knowledge of spectral signatures in these bands. Thus, it becomes necessary for Raytheon to educate the users of the VIIRS data. A VIIRS User's Guide is the one highly beneficial approach to help facilitate this education process

3.4.3.5   VIIRS Cloud Mask for Imagery

In addition to the Imagery and Imagery assist bands the analyst will also have access to the Cloud Mask IP. The Cloud Mask is an automated algorithm done within the VIIRS Data Processing Architecture. The objective of the VIIRS Cloud Mask (VCM) is to determine if a given Field of View (FOV) has a cloud present. The VCM is defined as the pixel level flag which indicates when a line segment extending between the sensor and a given area of the Earth's surface is intersected by a cloud. The cloud mask IP includes a binary cloudy/not cloudy flag operating at the pixel level using VIIRS radiance data. The VCM operates at the moderate resolution (742 m at nadir), and at the fine resolution (371 m at nadir). Also output by the VCM in addition to the binary cloudy/not cloudy flag are many processing flags and test result indicators, which are available to the imagery analyst to use for assisting in Cloud Cover and Cloud Type assessment.

3.4.3.5.1 Fine Resolution Cloud Mask

The VIIRS fine resolution bands 'nest' in the moderate resolution bands as depicted in Figure 26.

Fine Resolution

Moderate
Resolutio
n
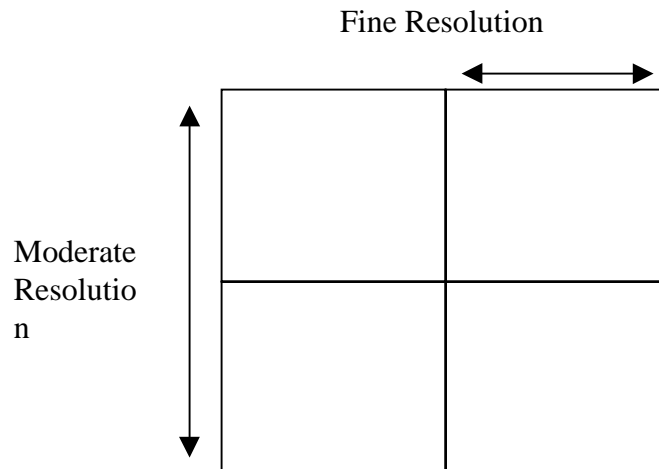
Figure 26. Depiction of the Nesting of the VIIRS Fine Resolution Bands within the VIIRS Moderate Resolution Bands

This nesting allows the inclusion of a fine resolution cloud mask along with the VCM output. Cloud tests performed with the 0.645, 0.865, 1.6, 3.74, and 11.45 micron bands are reported at the imagery resolution, and have spectral contrast tests performed upon them, along with tests being performed at the finest resolution they offer. These tests performed are based upon BT and Reflectance Thresholds that are MODIS and CLAVR in heritage. The details of the tests performed to detect clouds from the fine resolution bands are discussed in the VCM ATBD.

The primary benefit to mention to the imagery analyst is that the physical scale of the fine resolution cloud mask is consistent with that which the analyst will view the imagery. Due to this scale similarity fine details in the imagery being analyzed may be identified. The greatest benefits to the cloud analyst however will be in the Quality Control of the automated analysis being done will improve analysts capabilities. Cloud edge pixels which will be difficult to discern with the moderate resolution cloud mask will be more readily detectable with use of the fine resolution mask. Pixels containing thin cloud optical depths at subpixel resolution, which the moderate resolution cloud mask might not detect, may be detectable at the fine resolution. Finally smaller clouds may be detected and small scale cloud features may be brought out to assist in the cloud typing of the analyst.

3.4.3.5.2 Cloud Mask Output of Use to the Analyst

Table 10 lists the VCM IP output. The output is composed of 48 bits per pixel. Each of these bits, or combination of bits, is used to denote a particular flag or product of use to other EDRs located in the Data Processing Architecture. Most of the bits are at the moderate pixel resolution. Four of the bits are reserved to report cloud/no cloud at fine pixel resolution. The data contained within the VCM IP is of use to the cloud analyst as well.

Table 10. 48 Bit Intermediate Product output of the VCM

BYTE	Flag	Bit #	Note (bit results indicate)
1	Cloud Mask Quality Flag	1	1= Mask Okay/0=Mask Questionable
	Binary Cloud result	2	1= cloudy/0=not cloudy
	Cloud Imagery Resolution Flag	3-6	1=cloudy/0=not cloudy (each bit is a pixel of the 2x2 fine resolution pixels nested in the moderate resolution pixel), 1111 = all cloudy, 0000=all not cloudy
	Cloud Confidence Flag	7-8	4 confidence levels of Cloud Mask Flag, 11= Confident Cloudy, 10=Probably Cloudy, 01= Probably Clear, 00=Confident Clear
2	Sun Glint Flag	9-10	11= Geometry Based Sunglint, 10= Wind Speed Based Sunglint, 00= No Glint (1 spare flag 01)
	Snow Surface	11	1=Snow/Ice, 0=No Snow/Ice
	Surface Type	12-14	111=Land, 000=Water, 010=Coastal, 011=Desert Other 5 flags (101,110,100,001,010) reserved for additional surface types used in future
	Non-Cloud Obstruction	15	1=Yes, 0=No
	Thin Cirrus Detected (Daytime)	16	1=Yes, 0=No
3	Cloud Phase	17-18	11=water, 00=ice, 10=mixed, 01= unknown
	Pixel Within 2 of a cloudy pixel	19	1=yes, 0=no (moderate resolution pixel size considered)
	Shadow Flag	20	1=yes, 0=no
	High Cloud Flag	21	1=yes,0=no
	Low Cloud Flag	22	1=yes,0=no
	Fire Detected	23	1=yes, 0=no
	Day/Night	24	1=Day,0=Night
4	Cloud Test Flags	25-32	4 Cloud Test Results indicators 1=tested/0=not tested and 1=cloud detected/0=no cloud detected. Each Cloud test done has a 2 bit flag which tells if a pixel was tested and if it passed or failed.
5		33-40	4 Cloud Test Results indicators (see Byte 4)
6		41-44	2 Cloud Test Results indicators (See Byte 4)
		46-48	Spare Bits (2 more cloud tests allowed in future)

Quality Indicator: This bit indicates if there is a problem with the quality of the VCM IP which follows for the pixel in question. If an analyst sees a "1" result for this bit, he would not use or trust the VCM IP.

Binary Cloud result: This bit indicates if a cloudy/not cloudy result has been indicated for the pixel. This is at the moderate resolution.

Cloud Imagery Resolution Flag: These 4 bits tell the imagery analyst if clouds were detected in the 2x2 fine resolution pixels which are within the moderate resolution pixel. The 4 bits are ordered from the upper left fine resolution quadrant. Looking at Figure 26; the first bit is this upper left quadrant, the second bit is the upper right quadrant, the third bit is the lower left quadrant, and the fourth bit is the lower right quadrant. A bit result of '1' indicates a cloudy result, while a '0' indicates a not cloudy result for the fine resolution pixel. For example a result of '1000' would indicate that a cloud is present in the upper left quadrant of the 2x2 fine resolution pixels, while a result of '0010' indicates that a cloud is present in the lower left quadrant.

Cloud Confidence Flag: These 4 confidence levels are for the moderate pixel resolution flag, bit number two. These results denote the confidence of the pixel being cloudy or clear. This is of use to an analyst in assessing the cloudiness at the moderate resolution for difficult to assess pixels. More detail is explained in the VCM ATBD.

Sun Glint Flag: Sun glint pixels possess glitter contamination. These pixels may be difficult for the imagery analyst to assess cloudiness in. Consequently, the pixels in which possible sun glint is occurring are identified. Sun glint will not result in a cloud mask to not being generated. In the case of sun glint the solar tests performance may be inhibited, but the thermal channel tests will still be done to generate the equivalent of a nighttime cloud mask. Knowledge of sea surface winds is included in the sun glint test, surface winds can narrow the region in which sun glint may occur. There is a justifiable concern that cloud detection will not be as reliable in glitter-contaminated regions. A classification as clear is probably correct, but a classification as cloudy may actually be due to the glitter effect as opposed to a cloud. Sun glint will be considered over both land and water areas. Land regions are included because spatially unresolved water bodies, snow, or recent rainfall can also cause sun glint. Sun glint is also a function of surface with and the state of the ocean, and effected by sea surface winds.

There are two sun glint products in the VCM IP, the geometry based sunglint and the wind based sun glint. The analyst should consider the geometry based sunglint region to be what is the pixels in which geometric conditions allow for sunglint to be present. The wind based sunglint flag indicates the pixels in which sunglint should be present due to the winds presence, ie. A smaller region than the geometric region. Both of these sun glint products are at the moderate pixel resolution.

Snow Surface Flag: This is a flag which indicates the presence of snow/ice in the pixel. This is highly useful to the analyst in snow/cloud discrimination. More detail of this flag is in the VCM ATBD.

Surface Flag: This is a flag which indicates the surface type in the pixel. This is highly useful to the analyst in cloud cover determination.

Non-Cloud Obstruction Flag: Detection of non-cloud aerosols are one of the Cloud Types that an analyst must identify. For long path-lengths, aerosol-laden atmospheres may be misinterpreted as clouds by an imagery analyst. This test is present primarily for the imagery

analyst to assess the presence of aerosols by use of an automated indicator. This flag is at the moderate resolution of the pixels.

Thin Cirrus Detected (Daytime): This flag indicates to the imagery analyst if a thin cirrus has been detected by the invaluable 1.375 micron thin cirrus test. This will assist the analyst to both do Cloud Cover assessment and Cloud Type determination. This flag is at the moderate resolution.

Cloud Phase: This flag indicates to the imagery analyst what the cloud thermodynamic phase is of the cloud. This is useful for the analyst doing Cloud Type determination, as specific cloud types have dominate cloud water thermodynamic phases associated with them.

Pixel Within 2 of a Cloudy Pixel: This flag indicates to the imagery analyst if the pixel is within 2 pixels of a cloud. This may be used by an analyst to indicate cloud edges and quickly identify regions that are near cloud edges, and thus might need more detailed analysis to determine the cloud cover within the often difficult to determine cloud edge region.

Cloud Shadow Flag: This flag indicates to the imagery analyst when a cloud shadow has been detected. Regions which have cloud shadows are of interest to a cloud analyst in that they may assist the cloud to identify cloud regions better, in that the cloud shadow regions generally possess the shape and morphology of the cloud creating them. Cloud shadow flags will only be provided over vegetated land regions at present. The technique for detection of cloud shadows is discussed in the VCM ATBD. The flag is reported at moderate resolution.

High and Low Cloud Flags: This flag indicates to the imagery analyst that the cloud in the pixel was determined to be a high cloud or a low level cloud by the cloud detection algorithms. This will assist the Cloud Analyst in assessing the Cloud Type and both of these bit results can be used together to allow determine if single versus multi-layered clouds are present in the pixel. The VCM developer has noted that for multi-layered cloud conditions quite commonly the high and low cloud indicators are noted. These flags are based upon the predominance of specific cloud detection tests to detect high and low clouds, some cloud tests are sensitive to high clouds while others are sensitive to low clouds.

Fire Detected: This flag indicates to the imagery analyst that a fire has been detected within the pixel. Non-cloud obstructions/aerosols are emitted by fires, this will assist the analyst in detection of this Cloud Type in the pixels surrounding the fire region.

Day/Night: This flag indicates to the imagery analyst what the VCM considers day and night pixels. This can also allow the analyst to rapidly assess where the day/night terminator region is.

Cloud Test Flags: These flags are specific to the individual cloud tests results. Knowledge of these flags will allow the analyst to know which cloud tests caused a cloud to be detected, and assist the analyst in cloud typing. Specific tests are useful in detecting certain cloud types. This flag is reported at moderate resolution.

Spare bits: These bits are not presently used by the VCM IP, but they are there to be used in the future. The cloud imagery analyst might suggest uses for these bits, and the modularized construct of the VCM would allow the bit output requested/needed.

3.4.4 Performance of Manually-Generated Cloud Data

The performance of manually-generated cloud data with respect to the VIIRS requirements and the system specification (c.f. Tables 3 and 4) is reviewed in this section.

The performance analysis was conducted as part of the SRD requirements flowdown to the sensor, as described in Section 2.5 and documented Hutchison (1998).

3.4.4.1 Cloud Cover

Table 11 shows the Cloud Cover measurement uncertainty errors, stratified by cloud type. Performance is for a horizontal cell 3 times the imagery HSR, and is based on the sensor noise specification. Actual sensor performance is expected to be better than the specification.

Table 11. Cloud Cover Measurement Uncertainty

Cloud Type	Status (Nighttime)	Cirrus	Cumulus (Daytime)	Obscured Not Cloudy
Measurement Uncertainty	0.027	0.078	0.04	0.041

These results demonstrate that the predicted performance satisfies threshold requirements with margin, even for the driving case of thin cirrus.

Additional analyses were also completed to determine the capability of the human analyst to satisfy VIIRS Objective Requirements for the manually-generated cloud cover ARP. Results are based upon the manual detection of cirrus clouds, which is the worst case scenario. These results are shown in Table 12 and demonstrate that the measurement uncertainty remains below 0.1 for HCS 2 times HSR, which is the only attribute that changes between the VIIRS Threshold Requirement and Objective Requirement for the manually-generated cloud cover ARP. Therefore, the imagery channels selected for the VIIRS sensor also allow the human analyst to satisfy the VIIRS Objective Requirements for manually-generated cloud cover, even though there is little margin. (Blue denotes VIIRS Objective Requirements are satisfied for this ARP.)

Table 12 also shows the relationship between HCS and measurement uncertainty of manually-generated cloud cover analyses. (Blue denotes success in meeting Objective Requirements; Green is success in meeting Threshold Requirements.) Relatively small VIIRS pixels (HSR) are classified as either completely cloudy or completely cloud-free by the human analyst, which makes the distributions completely bi-modal at the HSR level. As these pixel data are aggregated to the reporting interval, these distributions become less bi-modal as the HCS size increases. Thus, larger the HCS, the less likely it is be perfectly correct but more important they are also less likely to be completely in error when compared to the a priori cloud map used to build the simulated VIIRS imager. The results is that the (RMSE) measurement uncertainty becomes smaller as the HCS becomes larger. At HCS 2x2 HSR, the measurement uncertainty

for the manually-generated analysis of cirrus in simulated VIIRS imagery using only the LWIR band is 0.099. The Objective requirement is 0.1 at this HCS; therefore, the objective requirement is satisfied, though with very little margin.

Table 12. Measurement Uncertainty versus HCS from manual analysis of cirrus with visible optical depth of 0.03.

HCS (2 x 2 pixels)	NUMBER OF HCS PIXELS IN SIMULATONS			BI-MODAL	UNCERTAINTY
	Total	Clear	Overcast	(Percent)	(Fraction)
Truth	16,129	10,363	4677	93.25	n/a
Analysis	16,129	10,124	4969	93.58	0.099
(3 x 3 pixels)					
Truth	7140	4417	1890	88.33	n/a
Analysis	7140	4364	2010	89.27	0.078
(4 x 4 pixels)					
Truth	3969	2389	967	84.56	n/a
Analysis	3969	2373	1049	86.22	0.069
(8 x 8 pixels)					
Truth	961	528	170	72.63	n/a
Analysis	961	529	194	75.23	0.050
(25 x 25 pixels					
Truth	100	40	3	43.00	n/a
Analysis	100	40	6	46.00	0.032

The threshold HCS requirement, shaded green, is 3 x 3 pixels. The objective HCS requirement, shaded blue, is 2 x 2 pixels. The results shown in Table 12 were obtained with the LWIR band, using a sensor noise model with more noise than the current specification (c.f. Section 2.2, Table 2).

3.4.4.2. Cloud Type

Three characteristics of clouds are considered by the human analyst in creating the Manually-Generated Cloud Type ARP. These characteristics include:

(1) Cloud spectral signatures: in general, stratus clouds are colder in the 3.75 micron band than the 11.45 micron band while the reverse is true for thin cirrus clouds.

(2) Cloud top temperatures: in general, water clouds can be segregated into lower and higher level clouds based upon their temperatures in the 11.45 micron band. For example, comparison of the cloud top temperature to cloud-free surface temperatures of the neighbor regions allows the analyst to estimate cloud top height, using the general rule that temperature decreases approximately 6 degrees Kelvin for every kilometer in the troposphere. This approach allows stratocumulus (low clouds) to be readily differentiated from altocumulus (middle clouds).

(3) Texture: in general, cumuliform clouds are readily differentiated from stratiform clouds and cirrus clouds are identified by texture. For example, cirrocumulus associated with the jet stream is famous for its "fishbone" appearance.

These characteristics can be combined to identify additional cloud types. For example, texture allows standing lenticular clouds to be identified and cloud top temperatures allow stratocumulus standing lenticular clouds to be separated from altocumulus standing lenticular clouds while spectral signatures allow cirrocumulus standing lenticular clouds to be identified.

Based upon the spectral signatures, cloud top temperatures, and the Raytheon VIIRS imager design, we believe it is possible to positively identify 13 of the 17 cloud types listed as Objective Requirements for the Cloud Type ARP, including all cloud types listed as Threshold Requirements. This list and techniques used for positive identification are shown in Table 13. Examples of the applications of these techniques are contained in Appendix A.

Table 13. Approach to the positive identification of cloud types by human analysts using VIIRS imagery and imagery assist bands.

Cloud Type	Abbreviation	Approach to Accurate Classification			Comments
		Spectral Signature	Shape/Texture	Temperature Contrast (cloud top vs cloud-free)	
Altocumulus	AC		x	x	
Altocumulus Castellanus	ACCAS				small scale features
Altocumulus (Standing Lenticular)	ACSL		x	x	
Altostratus	AS		x	x	
Cirrocumulus	CC	x	x	x	
Cirrocumulus (Standing Lenticular)	CCSL	x	x	x	
Cirrostratus	CS	x	x	x	
Cirrus	CI	x	x	x	
Cumulonimbus	CB	x	x	x	
Cumulus	CU		x	x	
Cumulus Fractus	CUFRA				small scale features
Towering Cumulus	TCU		x	x	
Stratus Fractus	STFRA				small scale features
Nimbostratus	NS				requires ancillary precipitation data
Stratocumulus	SC		x	x	
Stratocumulus (Standing Lenticular)	SCSL		x	x	
Stratus	ST	x		x	
Obscured/Not Cloudy	OBS	x	x		
Clear	CLR	x			

Cloud types achieved for Threshold Requirements are shaded green. Cloud types achieved for Objective Requirements are shaded blue. Unshaded cloud types are unachieved objective requirements.

The imagery channels chosen to satisfy the requirements for cloud cover also allow the threshold cloud types, listed in the table, to be identified with little or no ambiguity based upon unique spectral signatures, texture, and shape. Therefore, the minimum cloud typing can be completed with very high (>95%) probability of being correct.

Of the four cloud types which cannot be identified directly with VIIRS imagery and imagery assist bands, one is nimbostratus which is only differentiated from altostratus by the occurrence of rain, which cannot be positively identified by the VIIRS alone. However, use of CMIS

imagery would allow this distinction to be made. The other cloud types involve all fractus-type clouds (cumulus fractus, stratus fractus, altocumulus castellanus) which are identified by small scale features indicative of atmospheric instabilities. There small scale features are observatable by the human on the ground but are by a satellite with a 400 meter horizontal spatial resolution at 833 km in space.

3.4.5   Initialization and Validation

Initialization and validation activities can best be accomplished in coordinated with the U.S. Air Force Weather Agency, which is the primary customer for the manual and automated cloud data product EDRs, as described in Section 2.4.2. The purpose of these activities is to assure that ()1) VIIRS data products can be incorporated into the automated Cloud Depiction and Forecast System (CDFS) and that (2) human analysts have the necessary skills to fully exploit the VIIRS imagery in the quality control (BOGUS) process.   This initialization and validation process assumes that the CDFS program will provide AFWA with the capability to construct color composites (as described in Section 3.4.3.2) within the Satellite Data Handling System (SDHS) and that there exists an interactive environment which allow analysts to exploit these color composites in the quality control process to ensure the benefits of an operational test and evaluation program are fully achieved in an operational setting prior to the launch of the first VIIRS sensor.

While the development such a test and evaluation program will require the participation of numerous agencies (including the NPOESS IPO, AFWA, and Raytheon VIIIRS team), the proposed approach could utilize MODIS imagery and automated cloud data products (i.e. automated cloud cover and cloud top height EDRs) obtained from the EOSDIS as test data sets for initialization of the CDFS software environment. Human analysts would be given access to MODIS imagery. Training on the exploitation of theses data sources could be based upon the VIIRS User's Guide, shown in Appendix A.   This approach to an initialization and verification program is highly desirable since it would leverage existing software at AFWA and the human analysts needed to provide an independent assessment of the VIIRS imagery.

The pre-launch characterization and post-launch validation plan for the VIIRS Cloud EDRS will be extended to the Manually Generated Cloud Data. Details are discussed in the VIIRS System Verification and Validation Plan Document *[TP 154640-001].*

3.5   SEA ICE DATA PRODUCT DESCRIPTION

3.5.1   Processing Outline

The algorithm of concentration retrieval has changed since the version 2 ATBD, due to the new requirements. Instead of using spectral mixture analysis to select ice tie points, we now select tie points from the local distribution of surface temperature and/or surface reflectance. Surface temperature and surface reflectances are derived from TOA radiances in the imagery bands. This change was necessary because of the new requirement that all bands used to meet an Imagery threshold requirement must be Imagery bands.

The algorithm of ice edge location retrieval has changed since the version 2 ATBD, due to the new requirements on ice concentration. Instead of deriving ice concentration isolines, we now produce a gridded ice concentration map.

The sea ice data products are retrieved by an automated algorithm (ice edge location, ice concentration) and by manual analysis (leads and polynyas, data assimilation). As with cloud data products, the manual analysis is not part of the VIIRS operational system. It will be performed at various ice centers by trained analysts using established techniques. The ice fraction is derived by application of the tie point method, as discussed in Section 3.5.3.2. We retrieve and report the fraction of ice cover for each imagery pixel as the ice concentration product.

The process flow for the automated production of Imagery Sea Ice Data is described in the VIIRS Snow/Ice Module Software Architecture document *[Y2477]*. The main steps are as follows:

1) Input data, described in Section 3.5.2, is read in to the module. Pixels within the pre-specified horizontal coverage range are passed into the ice units, beginning with the ice concentration unit.

2) The surface reflectance image is passed into the ice concentration unit. Pixels with bad quality, land, cloud, and solar zenith angle flags are masked. Ice concentration is calculated for each good pixel.

3) The surface temperature image is passed into the ice concentration unit. Pixels with bad quality, cloud, and cloud flags are masked. Ice concentration is calculated for each good pixel.

4) The combined ice concentration for each pixel is calculated as the weighted mean of the individual band results. The band weights are derived from the RMS variation in that band.

5) The ice concentration is passed into the ice edge location unit. Pixels with no concentration result are masked. The ice edge location algorithm tags each pixel as edge or no edge, and computes edge location coordinates from the coordinates and concentration of each edge pixel and its neighbors.

The algorithm uses reflectance and surface temperature data obtained from intermediate products (IPs) produced from the Daytime Visible (DV) and Long-Wave Infrared (LWIR) imagery bands to meet the threshold requirements. Performance may be enhanced by the use of the Near Infrared (NIR) fine resolution band at 0.865 μm. The relative weight assigned to the DV and NIR bands shall be determined by initialization and validation (c.f. Section 3.5.6). Data shall be masked using a land/water mask prepared from NASA GTOPO30 or other applicable topographic or geographic data sets providing compatible spatial resolution. Following application of the land/water mask, data shall be masked using a cloud mask. The cloud mask *[Y2412]* is generated from non-Imagery SDRs at the VIIRS moderate resolution. A fine resolution cloud mask will also be available (c.f. Section 3.4.3.5), which may improve performance.

3.5.2 Algorithm Input

3.5.2.1 VIIRS Data

An automated algorithm will retrieve the sea ice concentration from the processed imagery. The input VIIRS data will be in the form of two-dimensional pixelized images of surface temperature, visible surface reflectance, and near IR surface reflectance. A summary of VIIRS bands is presented in Table14. The 0.645 and 11.45 μm imagery bands are sufficient to meet SRD requirements with margin. The 0.865 μm imagery-assist band provides extra margin.

Table 14. Imagery (Sea Ice Data) – Input Data Summary

λ(μm)	Δ λ(μm)	GSD (m) at Nadir (Track x Scan)	HCS (m) at Nadir (Track x Scan)	GSD (m) at Edge of Scan (Track x Scan)	HCS (m) at Edge of Scan (Track x Scan)
0.645	0.050	371 x 131	371 x 393	800 x 800	800 x 800
0.865	0.039	371 x 131	371 x 393	800 x 800	800 x 800
11.45	1.90	371 x 131	371 x 393	800 x 800	800 x 800

For optimal performance of the algorithm, the VIIRS data presented in Table 15 are desired:

Table 15. VIIRS data for the Imagery (Sea Ice Data) products

Input Data	Source of Data	Reference
Instrument Quality	VIIRS RDR to SDR Processor	*[Y3261]*
Geo-location	VIIRS Geo-location Algorithm	*[Y3258]*
Solar/Sensor Geometry	VIIRS RDR to SDR Processor	*[Y3261]*
Visible Surface Reflectance	VIIRS Atmospheric Correction Over Land Algorithm	*[Y2411]*
Near IR Surface Reflectance	VIIRS Atmospheric Correction Over Land Algorithm	*[Y2411]*
Surface Temperature	VIIRS Ice Surface Temperature Algorithm	*[Y2405]*
Cloud Mask	VIIRS Cloud Mask Algorithm	*[Y2412]*
Land/Water Mask	VIIRS Cloud Mask Algorithm	*[Y2412]*

Instrument Quality

Each pixel of each band image will have its own quality flag. Cells with quality below a threshold, to be determined, shall be excluded from further processing.

Raytheon

Geo-location

Geo-location of each imaged pixel will be used to report the latitude/longitude coordinate of each horizontal cell of the ice concentration product, and to report the ice edge location coordinates.

Solar / Sensor Geometry

The solar zenith angle will be used to determine the relative weight of the reflectance-based and temperature-based retrievals. Reflectance data will be progressively de-weighted as the solar zenith angle increases, providing a seamless transition across the terminator. The weighting function will be determined by pre-launch validation, as part of the initialization plan, and will be adjusted by post-launch validation. Solar/sensor geometry will be used to apply a BRDF quality flag, if warranted by pre-launch or post-launch validation.

Surface Reflectance

Discrimination of ice from open water can be made on the basis of their reflectance spectra. The VIIRS Atmospheric Correction Over Land algorithm [*Y2411*] will supply a surface reflectance intermediate product (IP) for the visible and near IR bands used by the algorithms. Models of surface reflectance error are used in our error analysis (c.f. Section 3.5.4.2).

Surface temperature

Surface temperature of the ice is needed for ice concentration retrieval at night, and is often useful for daytime retrievals.

The VIIRS Ice Surface Temperature algorithm *[Y2405]* will determine the temperature of ice surfaces for each imaged pixel, which will be supplied as a Surface Temperature Intermediate Product (IP). A model of surface temperature error is used in our error analysis (c.f. Section 3.5.4.2).

Cloud Mask

The VIIRS cloud mask *[Y2412]* is expected to derive a status of clear/probably clear/probably cloudy/cloudy for each pixel, following the convention of the MODIS cloud mask (Ackerman *et al.*, 1997). Pixels flagged as "cloudy" will be excluded from further processing. We expect that pixels flagged as "probably cloudy" will also be excluded. This determination must depend on an assessment of the cloud mask performance, particularly over snow and ice surfaces. Pixels flagged as "probably clear" will be processed, although we wish to flag the output ARP as "possibly cloud contaminated." Pixels flagged as "definitely clear" will be processed. It is anticipated that the cloud mask will also flag pixels that are shadowed by clouds. In that case, a cloud shadow quality flag will be assigned to those pixels. Ice edges are often associated with cloud edges, increasing the critical need for effective cloud masking.

Land / Water Mask

Imagery sea ice data will be reported for ocean pixels. Coastline pixels must be identified and reported with a quality flag. The best quality land/water map available will be used. It is believed that a 1 km land/sea map will be developed by the EROS Data Center (EDC) from data products generated by the MODIS instrument. The land/water mask will be supplied as part of the Cloud Mask *[Y2412]*.

3.5.2.2   Non-VIIRS Data

The algorithms for Imagery (Sea Ice Data) require no ancillary data from outside of the VIIRS system.

3.5.3   Theoretical Description of the Retrieval

In the following sections, the mathematical background of the processes outlined in Section 3.5.1 is described.

3.5.3.1   Physics of the Problem

Ice reflectance

Remote sensing and *in situ* studies of sea ice are relatively widespread and are of significant potential benefit. The wide range in spectral albedo observed in sea ice of various types and thickness is a well-established characteristic of sea ice.

Spectral reflectance curves differ for different ice type. Each ice type has its own characteristic spectral signature. Spectral albedo of sea ice at various bands undergoes significant changes depending upon ice thickness, structure, and the state of ice surface.

Reflectance from ice surfaces differs from snow reflectance because the ice consists of sheets rather than grains. Clear ice slabs are highly transmitting (Bolsenga, 1983). Reflectance occurs by scattering from impurities, such as brine pockets and air bubbles. Therefore, the reflectance observed from natural ice surfaces is highly variable, depending on the condition of impurities for a given ice sheet. Given the wide variety of ice conditions in nature, ice reflectance is not as well determined as snow reflectance. Snow reflectance is amenable to the Mie scattering theory (Warren, 1982). In contrast, studies of ice reflectance tend to be empirical.

Snow reflectance

The reflectance characteristics of sea ice surfaces are influenced by accumulated snow cover. Pure snow is a distinctive target across a part of the solar spectrum. It is among the brightest of natural substances in the visible and near-infrared part of the spectrum, but it is also often the darkest in the shortwave infrared (Dozier, 1989). The spectral albedo of snow depends on wavelength, and this dependency is controlled by the imaginary part *(k)* of the complex refractive index. This reaches a minimum at a wavelength of about 0.46 microns, and increases by a factor of 10^6 - 10^7 as wavelength increases out to 2.5 microns (Warren, 1982; Dozier, 1989). Light

transmission decays exponentially in snow across a distance *d* as exp(-4πkd/λ). The *e*-folding distance for snow (the distance over which transmittance is reduced to 1/e) decreases from more than 20 m in the 0.4 – 0.5 micron range to less than 1 mm at 1.6 microns.

Light in snow is scattered primarily by refraction through, not reflection from, the ice grains. Photons are scattered at the grain surfaces, but absorbed while traversing the grain interiors. Only about 3 percent of the light scattered by an ice grain is reflected from the external surface. Nearly 89 percent is refracted through the grain, and 8 percent is scattered after internal reflections (Bohren and Barkstrom, 1974). Because ice is so transparent to visible radiation, snow reflectance is insensitive to grain size in bands below 0.7 microns, but sensitive to absorbing impurities in the snow (Wiscombe and Warren, 1980; Grenfell *et al.,* 1981). Because absorption by ice is much stronger in bands above 1.4 microns, reflectance at these wavelengths is insensitive to absorbing impurities, but sensitive to grain size. Absorbing particulates affect snow reflectance out to 0.9 microns (Grenfell *et al.,* 1981; Warren and Wiscombe, 1980), so the 0.86 micron band is sensitive to both absorbing impurities and grain size. All aforementioned values in this paragraph are determined from geometric optics for a sphere.

The spectral signature of snow is unique among common substances. Clouds and snow are both bright across the visible and near-infrared region, but clouds are much brighter than snow in the shortwave infrared. This is because the smaller size of the scatterers in clouds decreases the probability of absorption in this spectral region where ice and water are moderately absorptive (Crane and Anderson, 1984; Dozier, 1984, 1989). Conversely, bodies of open water are dark at all wavelengths.

The physical basis of snow reflectance is also discussed in the VIIRS Snow Cover/Depth ATBD *[Y2401].*

Surface temperature

During a great part of the seasonal cycle, infrared bands will be the only available information to retrieve ice fraction. Infrared radiance allows us to calculate surface temperature.

Ice surface temperature is a good indicator of ice state for relatively thin ice. The surface temperature varies in a large range of magnitude depending on the stage of ice development or ice age (thickness). Thus, surface temperature is an indicator of ice age.

Changes in sea ice surface temperature are governed by the joint influence of vertical heat fluxes of different origin. The intensity of turbulent exchange by heat between the atmosphere and underlying ice surface, as well as the surface balance of long-wave radiation, directly depend on ice surface temperature. Vertical heat flux through ice cover is an explicit function of the vertical ice temperature profile, which depends on ice surface temperature. Thus, all main components of heat exchange between the atmosphere and the underlying ice surface (except short-wave radiation fluxes) are explicit functions of ice surface temperature.

In wintertime, heat flux between the atmosphere and ice is compensated by ice growth at the underside of the ice. There are no vertical changes in heat flux at the boundary between air and ice surface. At the same time, many components of heat flux depend on ice surface temperature.

Therefore, conditions of conservation of vertical heat flux at the surface can be fulfilled only if ice surface temperature is adjusted to varying influencing environmental conditions.

Ice thickness is the main factor determining vertical heat flux through the ice under specified atmospheric conditions. Thus, a general conclusion about the relation between ice surface temperature and thermodynamic processes in ice cover and atmospheric boundary layer can be formulated. Ice surface temperature is determined by the processes of vertical heat exchange and is a distinctive indicator of ice thickness.

Physical Hypotheses

A. Both surface temperature and reflectance measured on the basis of satellite data vary in a large range of magnitude depending on ice fraction and ice age. Thus, surface temperature and reflectance are a valuable source of information on ice fraction and age in the cell as the surface temperature and reflectance of a mixed ice/water pixel will depend on ice fraction as well as ice type. To separate the influence of ice fraction and ice type, we need to use an additional assumption about these two influencing parameters.

Our approach is based on a consideration of processes forming ice distribution. Spatial changes in the predominant ice type (age) and its properties are governed by freezing and melting and can be considered as smooth. This hypothesis, which is certainly correct in most cases, is used to develop the algorithm of ice concentration retrieval.

B. Sea ice cover in polar regions consists of different floating ice forms (ice floe sizes). The sizes of ice floes depend upon season and region decreasing during melting. A predominant ice floe size also decreases with decrease in ice concentration. But even in the summertime in the areas of open ice, at least 25% of ice floes have an average diameter greater than 500 m. In addition, ice floes of smaller size tend to gather in belts or spots of very close ice. As a result, we can state that in almost all cases, data of satellite observations even for relatively small areas of ocean surface will include pure pixels corresponding to ice.

Our approach takes advantage of the overwhelming probability that an ice scene will contain pure ice pixels in a region localized near any pixel that contains some ice. In that case, the condition of the predominant ice type in the area under consideration can be approximated as the reflectance (or temperature) peak of the distribution (histogram) of reflectance (or temperature). Our approach adopts the derived condition of the predominant ice type as the ice tie point for a given pixel.

C. Tie point analysis determines the fraction of ice. The tie point analysis is based on the assumption that the spectral fraction of ice is equal to the horizontal fraction of the pixel covered by ice. The ice tie point is reflectance (or temperature) of ice in various stages of development. These ice tie points are not predetermined but vary in large range depending on time and space. The tie points are scene specific and calculated by an automated algorithm, promising global operational capability.

D. Ice concentration is derived independently from three bands (visible reflectance from the DV band, near IR reflectance form the NIR band, and temperature from the LWIR band). We use

the reflectance tie points if the solar zenith angle is smaller than a threshold value. We use the temperature tie point if it is colder than a threshold value. If all tie points are useful, we calculate a weighted average ice fraction. The relative weights of the three bands are determined automatically from the conditions of a specific scene. Optimized band weights reduce error and provide a seamless day/night transition.

3.5.3.2 Mathematical Description of the Sea Ice Algorithms

3.5.3.2.1 Ice Concentration from Tie Points

Under conditions where there is a predominant ice type in a local area, ice fraction for each imaged pixel can be retrieved by the direct application of a tie point method. The tie point is a special case of spectral mixture analysis, restricted to two endmembers. The endmember signatures are derived from identifying pure pixels in the scene.

The ice fraction for a mixed pixel is:

$$f(p) = (\ b_p - b_{water})\ /\ (b_{ice} - b_{water}) \tag{3.5.1}$$

where: *$f(p)$ is the calculated sea ice fraction*

          b_{ice} is the brightness value of a pure ice pixel

          b_{water} is the brightness value of a pure water pixel

          b_p is the brightness value of the pixel

Our algorithm acquires three independent brightness values for each pixel. These are a visible reflectance, a near IR reflectance, and a temperature.

To take advantage of all of the available information, our algorithm generalizes the tie-point equation to three dimensions. We assume that the locus of equal ice fraction in multi-dimensional space corresponds to planes perpendicular to the line connecting ice and water tie points. In that case:

$$f(p) = \Sigma_j\ (b_{jice} - b_{jwater})(\ b_{jp} - b_{jwater})\ /\ \Sigma_j\ (b_{jice} - b_{jwater})^2 \tag{3.5.2}$$

where: *$f(p)$ is the calculated ice fraction*

          b_{jice} is the jth brightness value of a pure ice pixel

          b_{jwater} is the jth brightness value of a pure water pixel

          b_{jp} is the jth brightness value of the pixel

and the brightness values in Equation 3.5.2 have been normalized to their root mean square deviations on the scene. In that case, equation 3.5.2 is equivalent to:

$$f(p) = (\Sigma_j \, (w_j)(\, b_{jp} - b_{jwater}) \, / \, (b_{jice} - b_{jwater} \,) \,) \, / \, \Sigma_j \, w_j \qquad (3.5.3)$$

or:

$$f(p) = \Sigma_j \, (w_j \, f_j(p)) \, / \, \Sigma_j \, w_j \qquad (3.5.4)$$

where: *f(p) is the calculated ice fraction*

                w_j is the relative weight in band j

                b_{jice} is the jth brightness value of a pure ice pixel

                b_{jwater} is the jth brightness value of a pure water pixel

                b_{jp} is the jth brightness value of the pixel

                $f_j(p)$ is the ice fraction calculated from band j

and: $w_j = E_j \, (b_{jice} - b_{jwater})^2$ (3.5.5)

We see that the relative weights of the bands scale as the square of the difference in ice and water tie points relative to the RMS deviation of the scene. The factor E_j is included to allow for other band-dependent factors, such as solar zenith angle. To some extent, the degrading effects of large solar zenith angle will be found in increased RMS deviation in the reflectance bands. It must be determined whether an extra E_j factor is needed. This will be a goal of initialization.

Our approach is to calculate ice fraction for each band, according to equation 3.5.1, and derive a band-weighted ice fraction, according to equation 3.5.4, with band weights determined by equation 3.5.5.

Errors in deriving b_{ice} and b_{water} have been an obstacle to achieving global operational ice concentration retrieval. Our algorithm greatly reduces these errors by deriving tie points from the scene.

An ice/water threshold is derived to select the pixels used for the water distribution for scenes containing open water. We assume that a scene-corrected threshold corresponds to the minimum probability of reflectance and/or temperature located between values associated with water and ice. Location of the minimum is found by use of a sliding integral taken over the probability density of the parameter (reflectance or temperature). The range of measured parameter values is divided into a specified number of histogram bins. The histogram of the distribution for the scene is computed. The histogram is smoothed by a running boxcar filter of specified width, producing a sliding integral of the parameter distribution. The lowest value of the sliding integral is adopted as the ice/water threshold.

The water tie point is selected as the maximum in probability density distribution corresponding to the maximum of the sliding integral over water reflectance (temperature). We analyze water characteristics only in the immediate vicinity of the ice zone. It allows us to improve the

Raytheon

accuracy of water tie point determination as it eliminates water characteristics for areas far away from ice cover. Those characteristics can differ from open water properties in the vicinity of the ice zone.

A scene-corrected ice threshold is derived as the first minimum of the sliding integral of the parameter distribution. The water tie point is selected as the maximum of the sliding integral below the ice/water threshold. Figure 27 illustrates the process.
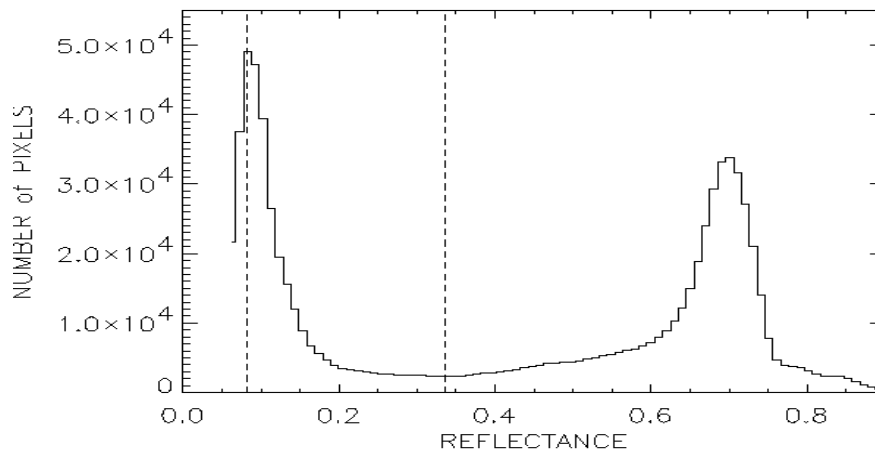
Figure 27. Distribution of 645 nm reflectance for an ice/water scene. The ice/water threshold reflectance (0.336) and the water tie point (0.083) are indicated.

For every imaged pixel, ice reflectance and/or surface temperature corresponding to an ice tie point (pure pixel) is calculated as the most probable reflectance and/or ice surface temperature in the vicinity of the pixel under consideration.

The ice tie point is derived locally for each pixel whose parameter value is on the ice side of the ice/water threshold. The distribution of parameter values in a local search window is acquired. The ice tie point is selected as the maximum value for a sliding integral of the local parameter distribution. Figure 28 illustrates the process.
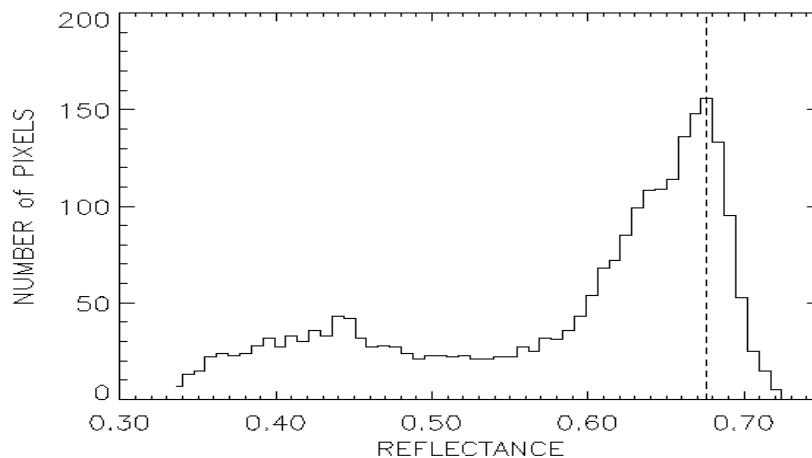

Figure 28. Distribution of 645 nm reflectance for a local search window centered on a single pixel of the scene.

For each pixel, a search window is used to establish the ice tie points from the local distribution of reflectance and/or surface temperature at the spatial scale of the window. The ice tie point is selected as the maximum value for a sliding integral of the local parameter distribution within the search window. For the example presented in Figure 28, the ice tie point for the pixel is equal to

0.676. The accuracy of the ice tie point selection depends on the size of the local search window. Optimization of the search window size will improve algorithm performance.

Having selected the ice and water tie points appropriate to a given pixel, the algorithm applies equation 3.5.3.2.1.1 to retrieve the ice fraction for each pixel. Ice concentration is reported as the ice fraction of each pixel. Concentrations less than 0.0 are set to 0.0. Concentrations greater than 1.0 are set to 1.0.

3.5.3.2.2 Ice Edge Location

Gridded ice fraction at imagery resolution is used to calculate ice edge location. A pixel is tagged as a possible ice edge pixel if one of the following conditions are met:

       (1) It has ice concentration greater than 0.1 and at least one neighboring pixel has ice concentration less than 0.1

       (2) It has ice concentration less than 0.1 and at least one neighboring pixel has ice concentration greater than 0.1

The set of tagged pixels are examined to derive ice edge isolines and ice edge coordinates. Each neighboring pair of tagged pixels will produce an edge coordinate and an edge pixel. The edge pixel will be that member of the pair whose concentration is closer to the 0.1 edge value. The edge latitude/longitude coordinate is derived by a weighted linear interpolation of the pixel coordinates:

$$\text{Lat} = (\text{Lat})_2 + (\,(\,(\text{Lat})_1 - (\text{Lat})_2\,)\, x\, (\, 0.1 - C_2\,)\, /\, (C_1 - C_2)\,) \qquad (3.5.6)$$

$$\text{Lon} = (\text{Lon})_2 + (\,(\,(\text{Lon})_1 - (\text{Lon})_2\,)\, x\, (\, 0.1 - C_2\,)\, /\, (C_1 - C_2)\,) \qquad (3.5.7)$$

       where : $C_{1,2}$ are the ice concentrations for pixels 1 and 2

and the coordinates apply to the pixel centers, as supplied by the geo-location algorithm *[Y3258]*.

Our algorithm also provides the option to retrieve the location of a diffusive ice edge by smoothing the ice concentration on an appropriate spatial scale. Different applications require different spatial scales of smoothing. Our algorithm allows for a flexible choice of smoothing kernel defined by specialized users' needs.

3.5.3.3 Archived Algorithm Output

Ice concentration will be archived as gridded products corresponding to imagery pixels.

Ice edge location will be archived as a contour on a map (an ice edge isoline) and as a set of latitude/longitude coordinates. The resolution will depend on the spatial scale at which the ice concentration is smoothed. It will range from imagery resolution, for unsmoothed concentration appropriate to a compact edge, to coarser resolution characteristic of diffusive ice edges.

Data quality flags will be attached to any reported product derived from input data with a data quality flag attached. These include, but are not necessarily limited to, data flagged as "probably clear", "cloud shadow", and "coastline".

3.5.4   Performance of Sea Ice Data

The performance of the algorithms with respect to the VIIRS requirements and the System Specification (c.f. Tables 5 and 6) is reviewed in this section.

3.5.4.1   Stratification

During Phase I of the NPOESS project, performance shall be verified by analysis, modeling, and/or simulation based on the instrument design and performance characteristics and the algorithms. The analysis, modeling, and/or simulation shall be sufficiently extensive in scope to verify that EDR requirements are met under a broad range of conditions that are representative of those occurring in nature, including both typical and extreme conditions.

3.5.4.1.1 Ice Concentration

We identify the following stratifications for ice concentration:

   1) Ice concentration "truth"

   2) Ice "type"

   3) Day/Night

Performance of the ice concentration algorithm is expected to depend on ice concentration "truth". A sensible stratification must then include ice concentration "truth" as a parameter. We have selected 4 ranges of ice concentration, 0.0-0.35, 0.35-0.65, 0.65-0.85, and 0.85-1.0. These ranges correspond to the following ice concentration zones: very open floating ice, open floating ice, close floating ice, very close floating ice.

Ice conditions are widely variable, depending on its stage of development. The contrast between ice and water tie points is generally larger for ice in later stages of development. Algorithm performance is very sensitive to tie point contrast. Analytically, the error in concentration derived from a tie point equation scales inversely with the tie point contrast. A sensible stratification should include ice "type" as a parameter. We have selected 2 ice types, "Young", and "First-Year or Older". Young ice is characterized by a thickness of 0.1 – 0.3 meters. We select 0.3 meters as our boundary between ice types. Our specification for ice concentration measurement uncertainty (c.f. Table 6) excludes ice with characteristic thickness less than 0.1 meter ("New Ice" and "Nilas").

We include a third stratification by type, which we call "Typical Scene", to illustrate expected performance for a typical probability of ice types.

The requirements are specified at nadir. Our stratification of sensor view angle is restricted to nadir view.

Raytheon

Nighttime and daytime retrievals are distinct. Daytime retrievals can use reflectance data as well as temperature data. Because thermal contrast between ice and water is smaller during the daytime, a daytime retrieval will rely more heavily on reflectance data. Nighttime retrievals, on the other hand, must rely solely on temperature data.

We have used a solar zenith angle of 60 degrees in our simulations to date. Our stratification of solar zenith angle is restricted to this value. A wider range of solar zenith angles shall be simulated in the future, following the development of surface reflectance error simulations over a wider range.

We report performance estimates for a representative sample of geophysical conditions:

      Case 1: Clear, Nadir, Solar Zenith Angle = 60 degrees

      Case 2: Clear, Nadir, Night, Air Temperature = -5 degrees Celsius

      Case 3: Clear, Nadir, Night, Air Temperature = -10 degrees Celsius

Daytime performance will depend on solar zenith angle, as surface reflectance errors increase with decreasing sunlight and increased atmospheric path length. We have modeled surface reflectance error for a solar zenith angle of 60 degrees to represent a typical solar elevation in sub-arctic regions during summertime.

Nighttime performance will depend on the surface air temperature. The thermal contrast between ice and open water increases as air temperature decreases. For an air temperature of 0 Celsius, the thermal contrast between most first year ice types and water is negligible. For an air temperature of –5 Celsius, the thermal contrast between most first year ice types and water is 3 – 4 degrees. For air temperatures colder than –10 Celsius, the thermal contrast between most first year ice types and water is greater than 8 – 10 degrees. We have selected two cases of nighttime air temperature (-5 Celsius and –10 Celsius) to illustrate the relative effect on performance. Typical nighttime air temperatures vary with latitude and season, but are usually colder than –10 Celsius in polar regions. We have found that performance at colder temperatures is similar to the performance at –10 Celsius.

3.5.4.1.2 Ice Edge Location

Ice edge location is derived directly from ice concentration. For this reason, its stratification is similar to that of ice concentration. We identify the following stratifications for the ice edge location:

      1) Ice "type"

      2) Sensor view angle

      3) Day/Night

Note that the ice concentration "truth" is not included as a stratification, because by definition the retrieval occurs at ice edges only.

The rationales for our stratifications are identical to the ice concentration stratification rationales discussed in Section 3.5.4.1.1, with the exception of ice concentration "truth".

3.5.4.2 Stratified Performance Analysis

3.5.4.2.1 Ice Concentration

Ice Concentration is derived by a tie point equation:

$$C \; = \; (P\text{-}W) \,/\, (I\text{-}W) \tag{3.5.8}$$

Where: P = measured parameter (either surface temperature or surface reflectance)

      W = water parameter value (tie point)

      I = ice parameter value (tie point)

Errors in P, W, and I contribute to the measurement uncertainty:

$$\sigma^2{}_C = (\; \sigma^2{}_P \; + \; C^2\,\sigma^2{}_I \; + (1\text{-}C)^2\,\sigma^2{}_w \;) \,/\, (I\text{-}W)^2 \tag{3.5.9}$$

Errors in P are derived from sensor and algorithm, and are taken from the stratified performances of the Surface Reflectance and Surface Temperature intermediate products (IPs). These are documented in the VIIRS System Specification *[SS 154640-001]* and in the VIIRS Imagery TIM *[Y4963]* . Precision and accuracy errors were applied to our test data sets.

I and W are derived from a scene, using search windows. Errors in I and W, caused by deviations of the derived ice and water tie points from the "true" pixel tie points, have been an obstacle to achieving global operational ice concentration retrieval. Our algorithm greatly reduces these errors by deriving tie points from the scene.

Our analysis of ice concentration measurement uncertainty was performed as follows:

We applied our algorithm to MODIS Airborne Simulator (MAS) scenes at a 50 meter pixel resolution. The test scenes are discussed in the VIIRS Test Data Set Specification Document. Reflectances in MAS band 3 (648 nm) and 7 (866 nm) were calculated from the TOA radiances. Brightness temperatures in MAS bands 45 (11 μm) and 46 (12 μm) were calculated from the TOA radiances. Surface temperature was computed by the Surface Temperature IP algorithm. The surface reflectances and surface temperature at 50 meter resolution were used as input data for our algorithm. The retrieved ice concentration was adopted as "truth". The 50 meter truth was aggregated to a VIIRS pixel size at nadir (8 x 8 aggregation to 0.4 km pixels) and adopted as VIIRS "true" concentration at nadir.

A model MTF with HSR = 0.4 km was then applied to the surface reflectance and surface temperature images to simulate VIIRS imagery at nadir.

We then perturbed the MTF-smeared reflectances, using our model errors for the Surface Reflectance IP in the VIIRS DV band (645 nm). The errors depend on surface reflectance truth,

Raytheon

which is correlated with ice concentration. Accuracy and precision errors were applied. Accuracy errors include a 2% calibration bias and an aerosol optical thickness bias of 0.05. Precision errors are derived from the sensor noise. Reflectance errors were calculated for a solar zenith angle of 60 degrees. We note that the VIIRS NIR band I3 (865 nm) is also available as a performance enhancement band. The daytime performance reported here is from VIIRS DV only.

We perturbed the aggregated temperatures, using model errors for the Surface Temperature IP. Surface Temperature IP performance was derived as follows:

The split-window Ice Surface Temperature algorithm was applied to MODIS Airborne Simulator (MAS) scenes at a 50 meter pixel resolution. Brightness temperatures in MAS bands 45 (11 μm) and 46 (12 μm) were calculated from the unperturbed TOA radiances in those bands, and used as input data to the algorithm. The retrieved surface temperatures were adopted as "truth". The 50 meter truth was aggregated to VIIRS imagery pixel sizes at nadir (8 x 8 aggregation to 0.4 km pixels). The aggregated temperatures were adopted as VIIRS "truth".

The MAS TOA radiances were then aggregated to VIIRS pixel size. A proxy for the VIIRS Long-Wave Infrared (LWIR) imagery band radiance was made from the average of the band 45 and 46 radiances. The VIIRS model radiances were then perturbed by our models for sensor noise and calibration bias. A 0.5% calibration bias was applied to all radiances. Sensor noise models for VIIRS bands M15 (11 •m), M16 (12 •m), and LWIR were applied to the corresponding radiances. The perturbed radiances were converted to brightness temperature, and used as input data to the Surface Temperature IP algorithm.

Surface Temperature IP accuracy, precision, and uncertainty errors were calculated from comparison of the retrieved surface temperature to the "truth". At nadir, these errors are 0.278K in accuracy and 0.378K in precision.

We applied the algorithm to the perturbed VIIRS scenes to retrieve ice concentration, and computed measurement uncertainty by comparing the retrieved concentration to the "VIIRS truth". The pixel deviations between retrieved and true concentration were aggregated 2 x 2 to a horizontal cell of 0.8 km. The aggregated deviations were sorted into the four truth stratification bins. For each bin, the RMS of the deviations was computed as the measurement uncertainty for that bin.

We applied the algorithm to the perturbed VIIRS scenes to retrieve ice concentration, and computed measurement uncertainty by comparing the retrieved concentration to the "VIIRS truth". We did this for three sea ice day time scenes:

> A Bering Sea scene in early April (AK_74_14) from the Alaska-April 95 campaign.

> Two Beaufort Sea scenes in late May (ACE_65_3 and ACE_65_8) from the FIRE-ACE campaign.

And for a lake ice daytime scene:

> A Lake Superior scene in February (WIN_46_16) from the WINCE campaign.

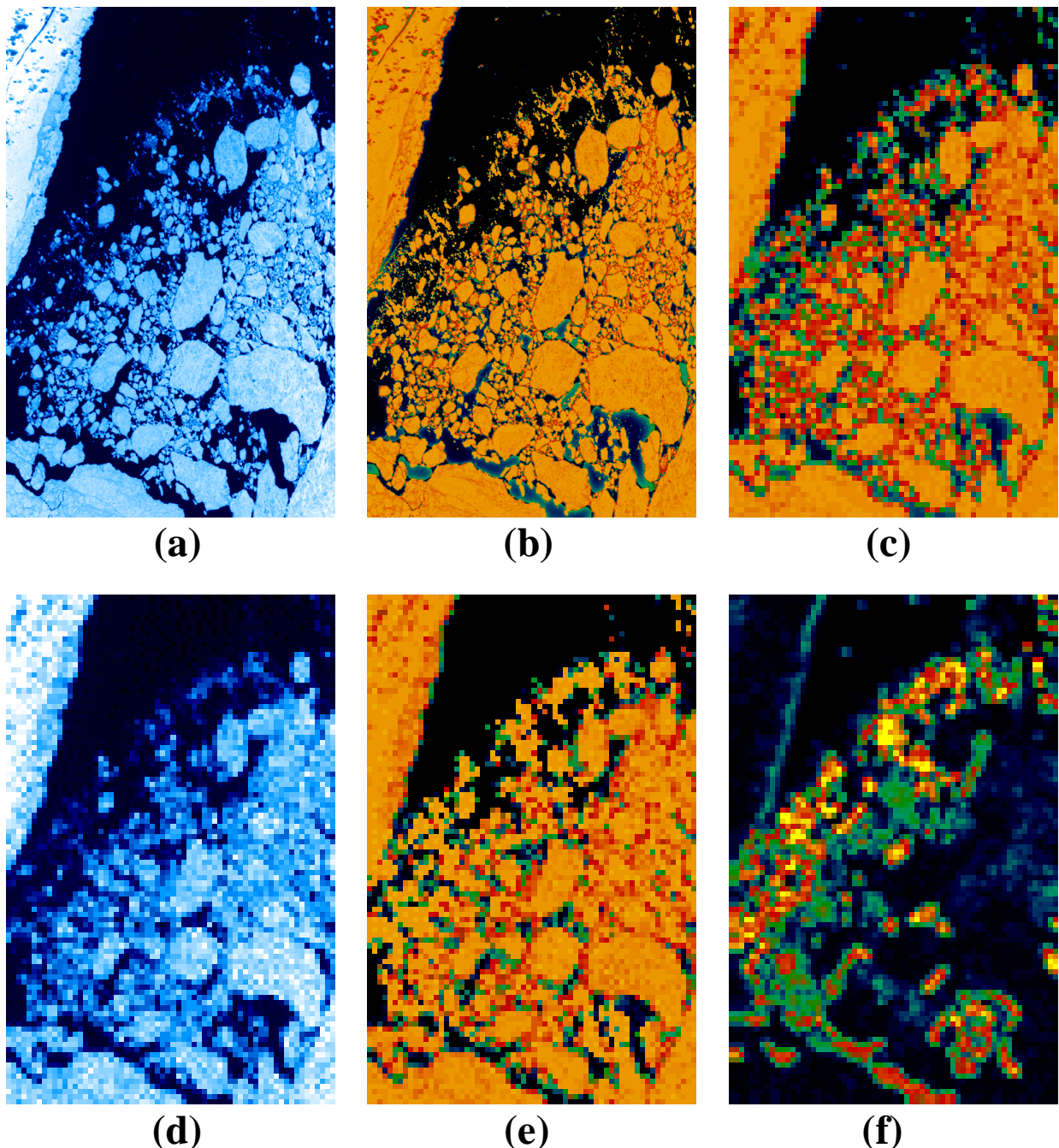An example of the procedure is illustrated for scene ACE_65_3 in Figure 29.

Figure 29. Illustration of the ice concentration performance analysis methodology. The scene is from the FIRE-ACE campaign of the MODIS Airborne Simulator (ACE_65_3).

The original MAS scene (a), is used as input to the ice concentration algorithm, which derives ice concentration at the 50 meter MAS resolution (b). The concentration is aggregated to the VIIRS pixel size of 0.4 km to produce VIIRS truth (c). Scene (a) is then perturbed by our model for the sensor effects to simulate expected VIIRS imagery at nadir (d). Scene (d) is used as input to the ice concentration algorithm, which derives the simulated VIIRS ice concentration (e). A comparison of result (e) with truth (c) produces an error estimate (f).

For daytime performance analysis, we use the reflectance data. For nighttime performance analysis, we use the surface temperature data, adjusted to simulate conditions when air

temperature is –5 Celsius and –10 Celsius. The adjustment is necessary, because the nighttime thermal contrast between ice and water scales linearly with the thermal contrast between air and water:

$$T_W - T_I = 16.2\ H\ (\ 3.61 + 0.049\ T_W + (T_W - T_A\ ))\ /\ (1.5 + 17\ H) \tag{3.5.10}$$

Where: T_W = Water Temperature (Celsius)

T_I = Ice Temperature (Celsius)

T_A = Air Temperature (Celsius)

H = Ice Thickness (meters)

Equation 3.5.10 is derived from energy balance, and is approximately correct for ice thickness less than 1 meter and for typical winter conditions.

An illustration of the process is shown as Figure 30. The MAS scene AK74_14 was processed to create simulated nighttime surface temperature imagery for conditions where surface air temperature = 0^0 Celsius, -5^0 Celsius, -10^0 Celsius, and -20^0 Celsius.

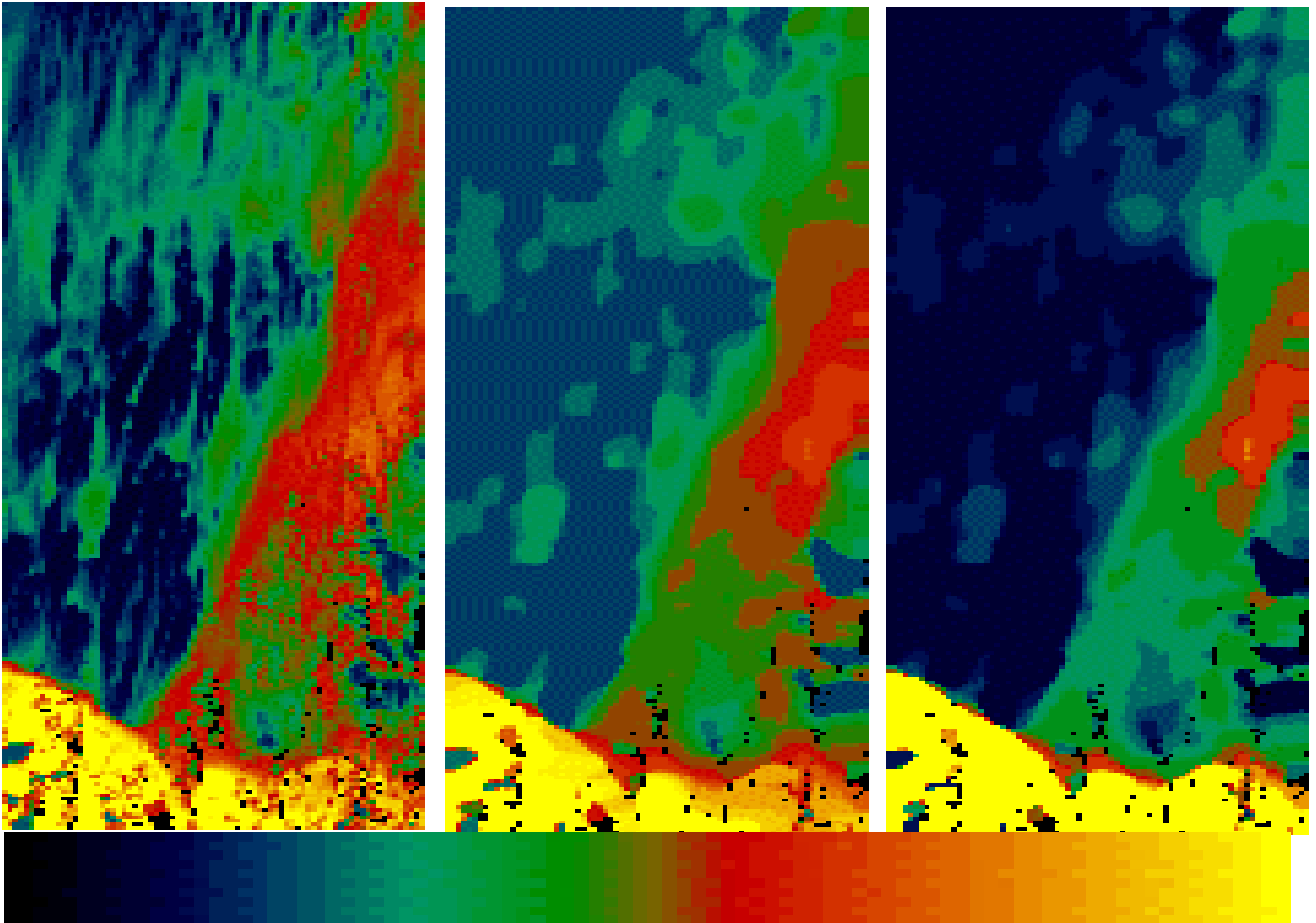**(a)**   **(b)**   **(c)**

Figure 30. (a) Simulated VIIRS daytime visible band imagery of the Bering Sea scene AK74_14. (b) Retrieved ice reflectance tie points. (c) Ice thickness, derived from the reflectance tie points.

The color table displays a reflectance range of 0.0 (blue) to 0.7 (yellow) and a thickness range of 0.0 (blue) to 0.2 meters (yellow). The ice thickness, shown in Figure 30c, is calculated from a fourth order polynomial thickness-reflectance relation, which was determined empirically by matching temperature and reflectance distributions from a number of ice scenes.

The ice temperature was then calculated from equation 3.5.11, for a given air temperature. The surface temperature was computed as:

$$T_S \ = \ T_I \ * \ C \ + T_W * (1\text{-}C) \tag{3.5.11}$$

Sensor perturbations were added as a precision error of 0.378 K and an accuracy error of 0.278 K. The resulting images are illustrated in Figure 31.
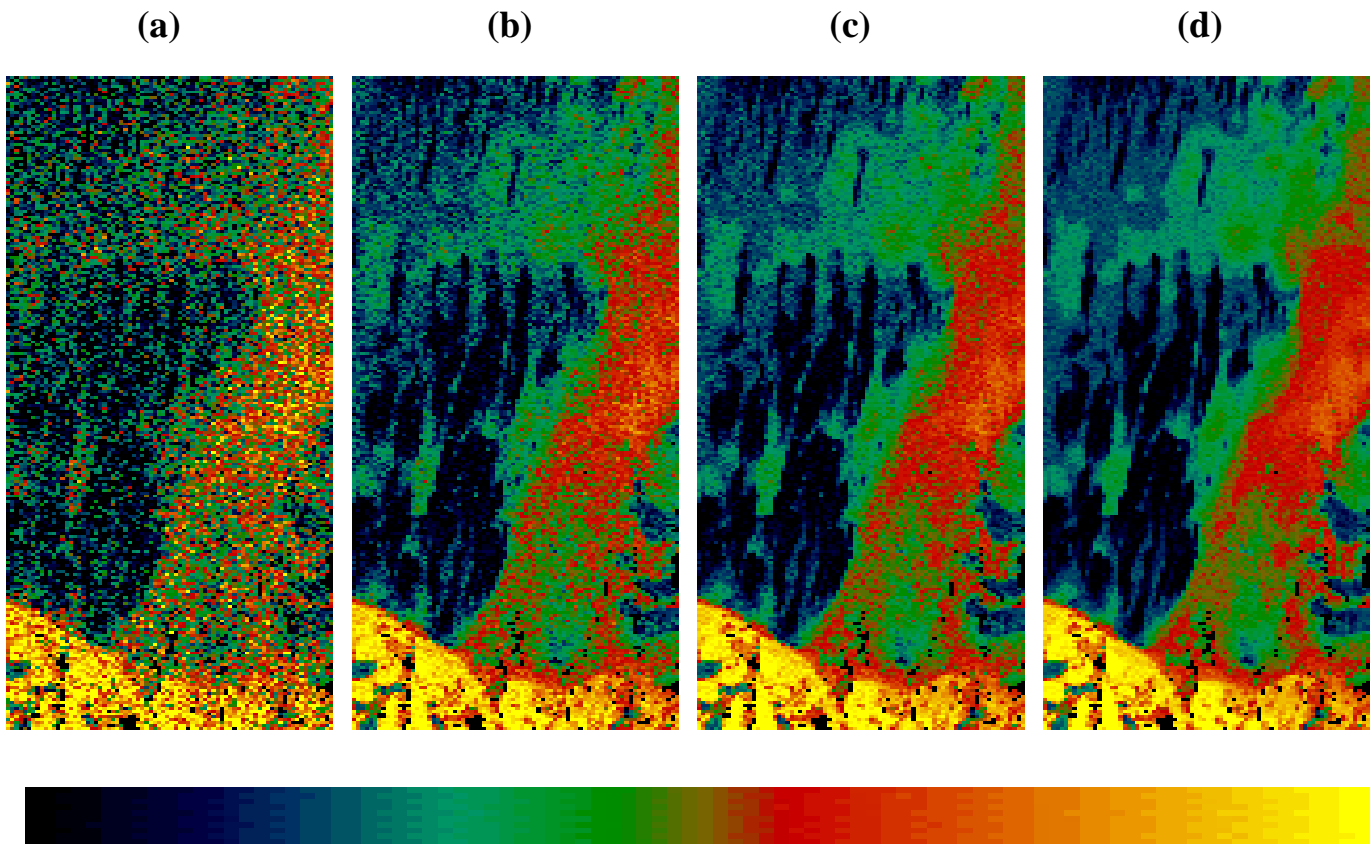
(a)   **(b)**   **(c)**   **(d)**

Figure 31. Simulated VIIRS nighttime imagery of the Bering Sea scene AK74_14, for air temperatures of 0 degrees Celsius (a), -5 degrees Celsius (b), -10 degrees Celsius (c), and -20 degrees Celsius (d).

Figure 31 shows how lower air temperatures increase the thermal contrast between ice and open water, resulting in smaller ice concentration measurement uncertainty. We will specify nighttime performance for the –5 and –10 cases.

Measurement uncertainties were computed from the scenes for each stratification of ice concentration truth. To assign these measurement uncertainties to an ice type bin, the mean tie point difference for each truth bin was computed. The truth / type bin error was then derived as:

$$\sigma_{mn} = \sigma_m \ (I\text{-}W) \ / \ (I\text{-}W)_n \qquad\qquad\qquad (3.5.12)$$

where: σ_{mn} = measurement uncertainty for (truth,type) bin (m,n)

   σ_m = observed measurement uncertainty for truth bin (m = 1,4)

   (I-W)   = observed mean difference in ice/water tie points

   (I-W)$_n$ = mean difference in ice/water tie points for ice type (n = 1,2)

and the scaling factor (1 / (I-W)) is based on equation 3.5.12. The third row of the table is derived as a weighted mean of the first two rows to represent a typical distribution of sea ice thickness.

The following tables show the errors stratified by ice concentration and ice type. The errors are for a horizontal cell of 0.8 km at nadir under clear conditions.

Table 16. Ice Concentration Measurement Uncertainty, Case 1 (Clear, Nadir, SZA=60 degrees)

Ice Type	Ice Concentration Truth			
	0.00 – 0.35	0.35 – 0.65	0.65 – 0.85	0.85 – 1.00
Young	.0537	.0755	.0769	.0844
First-Year/Multi-Year	.0265	.0373	.0380	.0417
Typical Scene	.0321	.0451	.0460	.0504

Table 17. Ice Concentration Measurement Uncertainty, Case 2 (Clear, Nadir, Night, Air Temperature = -5 Celsius)

Ice Type	Ice Concentration Truth			
	0.00 – 0.35	0.35 – 0.65	0.65 – 0.85	0.85 – 1.00
Young	.0301	.0593	.0548	.0574
First-Year/Multi-Year	.0232	.0457	.0423	.0443
Typical Scene	.0244	.0480	.0444	.0465

Table 18. Ice Concentration Measurement Uncertainty, Case 3 (Clear, Nadir, Night, Air Temperature = -10 Celsius)

Ice Type	Ice Concentration Truth			
	0.00 – 0.35	0.35 – 0.65	0.65 – 0.85	0.85 – 1.00
Young	.0277	.0546	.0505	.0529
First-Year/Multi-Year	.0214	.0421	.0389	.0408
Typical Scene	.0225	.0442	.0409	.0428

Typical performances are better than 0.06, compared with our specification of 0.1.

It should be noted that the (1 / (I-W)) factor in the equation for ice concentration measurement uncertainty is the primary determinant of performance. As the contrast between ice and water (I-W) decreases, errors increase inversely. Our simulations indicate that we do not attain our specification when the thermal contrast between ice and water is less than 2.2 K and the visible reflectance contrast is less than 0.14. The effect of reducing all of our system errors by a factor of 2, for example, would allow us to attain our specification for an additional range of 1.1 K in ice temperature. Performance is limited more by the geophysical conditions of the scene than by the sensor/algorithm limitations.

3.5.4.2.2 Ice Edge Location

Ice edge location is computed by linear interpolation of the measured ice concentrations between neighboring pixels. Neighboring pixel pairs are selected when their measured concentrations are on different sides of the 0.1 concentration threshold defining an ice edge.

$$\text{Lat} = (\ (C_1 - 0.1) \times (\text{Lat})_2 + (0.1 - C_2) \times (\text{Lat})_1) / (C_1 - C_2) \qquad (3.5.13)$$

where: C_1 = measured ice concentration for pixel with greater concentration

   $(\text{Lat})_1$ = latitude for pixel with greater concentration

   C_2 = measured ice concentration for pixel with lesser concentration

   $(\text{Lat})_2$ = latitude for pixel with lesser concentration

A similar equation is applied for edge longitude.

Errors in C_1 , C_2 , $(\text{Lat})_1$, $(\text{Lon})_1$, $(\text{Lat})_2$, and $(\text{Lon})_2$ contribute to the measurement uncertainty:

$$\sigma^2_{\text{Lat}} = (A\ ((\text{Lat})_1 - (\text{Lat})_2)^2\ \sigma^2_C\ ) / (C_1 - C_2)^2\ )\ +\ \sigma^2_G \qquad (3.5.14)$$

where: A   = factor depending on separation of C1 and C2 from 0.1.

   σ_G = Geo-location error in latitude.

and σ^2_C = $\sigma^2_{C1} = \sigma^2_{C2}$ is assumed.

A similar equation applies to longitude error.

The combined edge location error therefore has the form:

$$\sigma^2_{\text{Edge}} =\ \ B\ P^2\ \sigma^2_C\ +\ \sigma^2_G \qquad (3.5.15)$$

where P   = separation of pixel centers (km)

   σ_G = Geo-location error of the pixel centers (km)

---

and:

$$B = A / (C_1 - C_2)^2 \tag{3.5.16}$$

Our analysis of ice edge location measurement uncertainty was performed as follows:

We applied our algorithm to the same MODIS Airborne Simulator (MAS) scenes we used for ice concentrastion (c.f. Section 3.5.4.2.1) at a 50 meter pixel resolution. Reflectances in MAS bands 3 (648 nm) and 7 (866 nm) were calculated from the TOA radiances. Brightness temperatures in MAS bands 45 (11 μm) and 46 (12 μm) were calculated from the TOA radiances. Surface temperature was computed by the Ice Surface Temperature algorithm. The surface reflectances and surface temperature were used as input data for our algorithm. Our ice concentration algorithm was applied. The retrieved ice concentration was used as input data to our ice edge algorithm. The latitude/longitude coordinates for compact edges were adopted as edge location "truth".

We applied the ice concentration algorithm to the perturbed VIIRS scenes. The retrieved ice concentration was used as input data to our ice edge algorithm. We calculated the distance between each retrieved compact ice edge location and the nearest "true" ice edge, converting degrees latitude and longitude to km. The conversion accounts for the cosine of the latitude reduction in longitude degree to km conversion.

An example is shown as Figure 32.
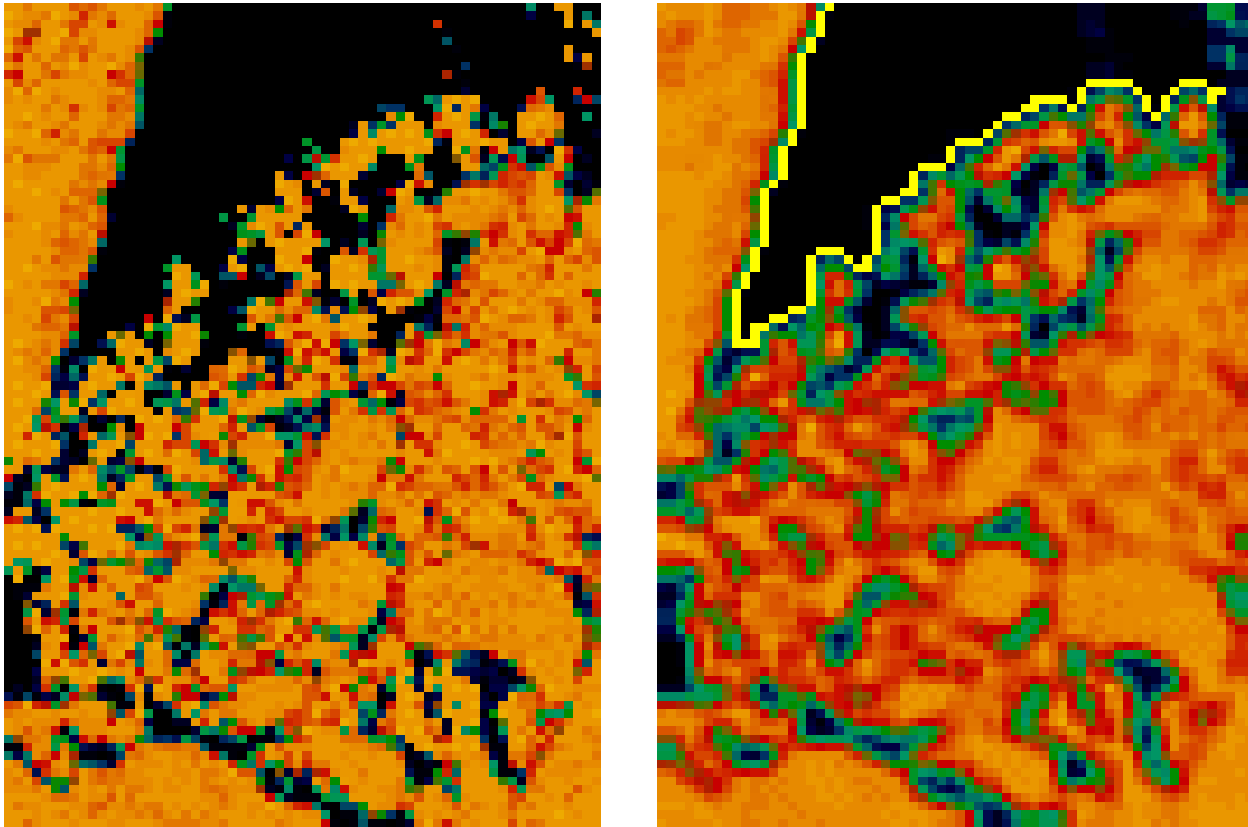
Figure 32. Illustration of ice edge location retrieval. The scene is from the FIRE-ACE campaign of the MODIS Airborne Simulator (ACE_65_3).

The ice concentration retrieval at nadir (Figure 32 left) is input to the algorithm, which produces compact and diffuse ice edge isolines (Fgiure 32 right). The isolines are superimposed on the smoothed ice concentration map used by the algorithm to derive diffuse ice edge location.

The algorithm output is also a set of latitude/longitude coordinates, derived in the vicinity of the isolines by equation 3.5.13. Ice edge location measurement uncertainty is calculated from the deviation of the retrieved edge coordinates from the coordinates of the nearest true ice edge. The mean location error for the compact edge is 0.134 km.

The error is assumed to scale with ice concentration measurement error, from equation 3.5.15. We therefore scaled our derived edge location measurement errors by the corresponding ice concentration measurement uncertainties for the different ice types, as indicated in Section 3.5.4.2.1. That is, we use the observed errors in ice concentration and ice edge location to determine the B factor for the scene, which we adopt as typical for a compact ice edge.

Geo-location errors of 0.067 km at nadir and 0.233 km at edge of scan were then applied, following our system specification for geo-location error *[SS154640-001]*.

Raytheon

The following tables show the errors stratified by scan angle and ice type. These apply to compact ice edges only. Errors for diffuse ice edges will depend on the spatial scale of ice concentration gradient.

Table 19. Ice Edge Location Measurement Uncertainty (km),
Case 1 (Clear, Nadir, SZA=60 degrees)

Ice Type	Scan Angle	
	Nadir	Edge of Scan
Young	0.266	0.690
First-Year/Multi-Year	0.144	0.396
Typical Scene	0.168	0.453

Table 20. Ice Edge Location Measurement Uncertainty (km),
Case 2 (Clear, Nadir, Night, Air Temperature = -5 Celsius)

Ice Type	Scan Angle	
	Nadir	Edge of Scan
Young	0.211	0.567
First-Year/Multi-Year	0.168	0.461
Typical Scene	0.176	0.479

Table 21. Ice Edge Location Measurement Uncertainty (km),
Case 3 (Clear, Nadir, Night, Air Temperature = -10 Celsius)

Ice Type	Scan Angle	
	Nadir	Edge of Scan
Young	0.192	0.553
First-Year/Multi-Year	0.154	0.452
Typical Scene	0.160	0.468

Typical performances at nadir are better than 0.3 km, compared with our specification of 0.4 km.

Typical performances at edge of scan are better than 0.7 km, compared with our specification of 1.0 km.

As ice edge location is derived from ice concentration, the error is similarly sensitive to the contrast between ice and water.

3.5.4.3   Error Budgets

We identify the following factors as possibly contributing to the total error budget for ice concentration:

- Tie Point errors
- Sensor noise
- Calibration

- MTF
- Band Registration

Tie Point Errors: The real variation in ice and water tie points can not be entirely accounted for with a data set of finite spatial resolution. We model these errors by comparing the retrieval of ice concentration at VIIRS resolution with the retrieval at MAS resolution. We make the reasonable assumption that the tie point errors at a resolution of 50 meters are negligible compared with the errors at a resolution of 0.4 km.

Sensor Noise: The dominant source of error in measured reflectance and/or temperature is expected to be the precision error. This error is due to sensor noise and to variations in atmospheric condition on the spatial scale of the VIIRS pixel. Our analysis shows that sensor noise will be the dominant precision error for most cases. We therefore model these errors by perturbing our "true" reflectances and temperatures by adding sensor noise to the radiances.

Calibration: Our algorithm is not expected to be sensitive to accuracy errors in reflectance and temperature, since the measured parameter, the ice tie point, and the water tie point will all be shifted by the same error. To test this hypothesis, we applied a calibration bias of 2% to the reflectance and 0.5% to the temperature.

MTF: MTF smearing of the radiances will alias real horizontal variability into errors in measured reflectance and/or temperature for a given pixel. We model these errors on our scenes by applying the sensor MTF specification to the images.

Band Registration: Band-to-band registration errors will also alias horizontal variability into measurement error. These errors only apply to a retrieval which uses more than one band. Since our performance analysis is based on single band retrieval, band registration errors were not simulated. If the retrieval were to use more than one band to enhance performance, band registration error must be considered. For now, we note that the current performance analysis can always be achieved with a single band. If a multi-band result is worse, due to the effects of band registration or non-optimum band weighting, we always have the option of using the single band.

An error budget for ice concentration is shown in Table 22.

Table 22. Error Budget for Ice Concentration

IMAGERY (ICE CONCENTRATION) Specification v3 (PDR)	Case:	Clear, Nadir, SZA = 60 degrees, Truth = 0.85-1.00, Typical Scene
	Measurement Uncertainty	Reference
Threshold	0.1000	VIIRS SRD
Objective	0.1000	VIIRS SRD
System Specification	0.1000	Raytheon VIIRS Specification v3
System Performance	0.0504	This document
System Margin	0.0864	RSS Difference of Specification and Performance
Algorithm Performance	0.0475	This document
Sensor Performance	0.0170	This document

We identify the following factors as contributing to the total error budget for ice edge location:

- Ice Concentration
- Horizontal Spatial Resolution (HSR)
- Geo-location

Ice Concentration: The algorithm uses the ice concentration image as input data. Errors in ice concentration will result in ice edge location measurement error, as can be seen from Equation 3.5.15. We model these errors by comparing ice edge location retrievals from "true" ice concentration with retrievals from ice concentration perturbed by our various error models, as described in Section 3.5.4.2.1.

Horizontal Spatial Resolution: The coarseness of the VIIRS pixel size (P in equation 3.5.15) will limit the accuracy of the interpolation of pixelized ice concentration to ice edge coordinates.

Geo-location: Errors in geo-location of the VIIRS reflectances and temperatures input to the ice concentration algorithm will propagate into error in the ice edge location derived from ice concentration.

The B factor in equation 3.5.16 is scene dependent, and depends on the compactness of the ice edge. Our errors are derived from analysis of compact edges only. The error due to non-zero P combines with the ice concentration error, so is not budgeted separately. The combined pixel resolution/ice concentration error is budgeted as "ice concentration/resolution". The error is allocated to the algorithm subsystem, as the ice concentration algorithm error is larger than the ice concentration sensor error.

Error budgets for ice edge location are shown in Tables 23 and 24.

Table 23. Error Budget for Ice Edge Location (Nadir)

IMAGERY (ICE EDGE LOCATION) Specification v3 (PDR)	Case:	Clear, Night, Air Temperature = -5 Celsius, Nadir, Typical Scene
	Measurement Uncertainty (km)	Reference
Threshold	TBD	VIIRS SRD
Objective	TBD	VIIRS SRD
System Specification	0.400	Raytheon VIIRS Specification v3
System Performance	0.176	This document
System Margin	0.243	RSS Difference of Specification and Performance
Concentration/Resolution	0.162	This document
Geo-location	0.067	Raytheon VIIRS Specification v3

Table 24. Error Budget for Ice Edge Location (Edge of Scan)

IMAGERY (ICE EDGE LOCATION) Specification v3 (PDR)	Case:	Clear, Night, Air Temperature = -5 Celsius, Edge of Scan, Typical Scene
	Measurement Uncertainty (km)	Reference
Threshold	TBD	VIIRS SRD
Objective	TBD	VIIRS SRD
System Specification	1.000	Raytheon VIIRS Specification v3
System Performance	0.479	This document
System Margin	0.510	RSS Difference of Specification and Performance
Concentration / Resolution	0.418	This document
Geo-location	0.233	Raytheon VIIRS Specification v3

3.5.4.4 Limits of Applicability

In this section, we discuss the conditions under which our specified performance can not be attained.

Cloudy: Imagery Sea Ice Data are required under clear conditions only, with clear defined as a cloud optical thickness less than 0.03. Our specification is for clear scenes only. The standard approach to minimize errors caused by clouds is to mask pixels where clouds are likely to be present in the radiance path. The VIIRS Cloud Mask *[Y2412]* will perform this function. Because no cloud mask is perfect, there will be some source of error caused by the effects of unmasked clouds. Thin clouds will perturb the upwelling surface radiance by absorption and scattering, and will also be a source of reflected radiance unrelated to the surface. There will also be error due to incorrect classification of cloud contaminated pixels as clear. There will also be effects from cloud shadows. Cloud error assessment will require an analysis of cloud masking performance over ice surfaces. It is desirable to perform tests to determine the expected size of

the retrieval errors under various conditions of cloud optical thickness and phase. Thin cirrus clouds are a particularly important case of cloud error, because they are particularly difficult for the cloud mask to detect over snow. These tests require the simulation of TOA radiances from snow surfaces with a variety of overlying cloud layers. In the absence of these tests, we cannot quantify the effect of clouds. The conditions under which the specification can not be attained may include a range of cloud optical thickness. The range will be determined by a balance between the increasing effect of clouds on the signal and the increasing probability of correct masking. The specification of this range has been deferred to future verification activity. It is expected that the VIIRS Cloud Mask, which will build on MODIS heritage and experience, will perform well enough to allow for effective operational retrieval of sea ice data from VIIRS.

Low Contrast Between Ice and Water Tie Points: The error in ice concentration scales inversely with the difference between the ice and water tie points. As this difference approaches a critical point, performance degrades rapidly. Our simulations indicate that we do not attain our specification for ice concentration measurement uncertainty when the thermal contrast between ice and water is less than 2.2K and when the reflectance differences are less than 0.14. In general, we will then not attain our specification for ice edge location measurement uncertainty. This occurs under the following conditions:

Low light or nighttime during summer: The thermal contrast between ice and open water is too low during part of the summer to allow for ice concentration derivations from thermal bands. A reliance on solar reflectance bands suffers from limitations during low light conditions.

"New" ice: Temperature and reflectance contrasts are strongly dependent on ice thickness. The contrasts are generally too low for ice with a thickness less than 0.05 to 0.1 meters, depending upon local conditions. Our specification and performance result therefore excludes "New" ice.

3.5.5 Practical Considerations

3.5.5.1 Numerical Computation Considerations

We optimized our scheme of choosing parameters in sliding window. As a result of this improvement, the requirement to retrieve ice products on a global, operational basis in a 20 minute time frame places no constraints on our algorithms.

3.5.5.2 Programming and Procedural Considerations

All procedures are automatic, to perform in the operational environment.

3.5.5.3 Configuration of Retrievals

The Imagery/Sea Ice Age algorithm expects the VIIRS Cloud Mask IP, the VIIRS Surface Reflectance IP, and the VIIRS Ice Surface Temperature IP. The imagery ice product output is needed as input ancillary data by the VIIRS Sea Ice Age/Edge Motion EDR. The NPOESS processing configuration is designed to satisfy these expectations.

3.5.5.4 Quality Assessment and Diagnostics

Quality flags will be attached to each archived result.

3.5.5.5 Exception Handling

Pixels identified by the cloud mask will be skipped. Pixels with bad quality flags will be skipped and flagged. Bands with bad quality flags will be removed.

3.5.6 Initialization and Validation

Initialization and validation activities shall be coordinated with the National Ice Center, with the purpose of assuring that the VIIRS data products can be incorporated into their strategic product.

MODIS Airborne Simulator (MAS) observations will be used to optimize cloud detection over ice surfaces. The VIIRS Cloud Mask will be applied over a series of MAS images for which there are varying types of ice to evaluate and optimize its performance.

Detection of shadows over ice covered regions will be investigated to initially flag the pixels where shadows exist. In the case of a shadow being detected the effects of the shadows need to be assessed. In the polar regions cloud shadows are quite common due to both the frequency of cloud cover, and the low sun angles. Shadows are seen as a risk which may be reduced by using both radiative transfer modeling and analyzing MAS data in which shadows are visible over snow covered regions.

Radiative transfer models will be applied to large solar zenith angle data to optimize the models for polar conditions, and to develop decision rules for solar zenith angle thresholds. MODIS data taken at solar zenith angles greater than 70 degrees will be studied to fine tune our solar zenith angle threshold for daytime conditions. The limiting factor is believed to be the reliability of atmospheric correction at larger solar zenith angles. Plane parallel radiative transfer algorithms are inaccurate for angles greater than 70-75 degrees. Development of improved radiative transfer models at larger angles will allow us to relax this constraint. To solve the Radiative Transfer Equation appropriately one would have to take into account the spherical shell atmosphere geometry (Thomas and Stamnes, 1998). It is expected that "truth" can be established from *in situ* data obtained from MODIS validation campaigns.

The plan includes sensitivity studies, analysis of simulated VIIRS data, and verification using MODIS-type data. Observations from AVIRIS, MAS, MODIS, GLI, and NPP will be used in the pre-launch phase to study the error characteristics and optimum techniques for the algorithm. It is expected that post-launch MODIS validation data will be of great value. This data is expected to include *in situ* field measurements combined with MODIS observations, MAS underflights, and low level aircraft measurements at spatial resolutions less than 10 meters. Our plan is to use this data in combination with the VIIRS sensor model to produce simulated VIIRS scenes, apply our algorithms to retrieve our ARPs, and compare our results with "truth" derived from *in situ*, aircraft, and MAS data.

Band weights will be selected during pre-launch characterization, using MODIS validation data. These weights may be seasonal, as the reflectance and thermal contrasts between ice and open water vary seasonally. The optimum weights of the 645 nm and 865 nm bands will be determined by comparison of simulated VIIRS retrievals to ground truth from MODIS validation data.

Our plan is designed to interface smoothly with post-launch validation activity. We would propose to conduct a post-launch VIIRS validation campaign similar to the MODIS validation activity. In this sense, post-launch validation will already have been simulated by the pre-launch validation activity. Following launch, we would substitute real VIIRS data for the pre-launch simulated data. We would establish "truth" by the same process.

4.0　ASSUMPTIONS AND LIMITATIONS

4.1　ASSUMPTIONS

The following assumptions apply to the algorithms described in this document:

- The reflectivities and emissivities for materials classifications used in the VIIRS simulations represent the real world.

- MODTRAN 3.7 can accurately generate upwelling radiances for clear and cloudy atmospheres, especially handling multiple scattering of clouds and highly reflective surface conditions.

The statements and conclusions pertaining specifically to automated sea ice retrieval are subject to the validity of the following assumptions:

- An effective cloud mask over snow and ice surfaces will be available from the VIIRS Cloud Mask IP *[Y2412]*.

- Surface reflectances, brought to standard conditions, will be derived from TOA radiances with errors as specified in the VIIRS System Specification *[SS154640-001]*.

- A Surface Temperature IP will be provided, with errors as specified in the VIIRS System Specification *[SS154640-001]*.

4.2　LIMITATIONS

The following limitations apply to the algorithms described in this document:

- The accuracy of cloud analysis in the manually generated cloud products of the Imagery EDR are limited to cloud features which can be detected by the VIIRS horizontal spatial resolution. The VIIRS design may not detect all sub-pixel clouds.

- The accuracy of manual analyses generated from simulated VIIRS imagery is limited by the analysts ability to create cloud, no cloud analyses with the Cloud Ground Truth Analysis (CGTA) software. Cloud edges represent the greatest challenge. However, experienced image interpreters agree within about 1-2 percent in total cloud, no cloud analyses of complex scenes.

- The capability to recommend TBD values for "obscured/not cloudy if the LOS extinction optical thickness is = 0.03 (TBD)" is limited by the standard profiles and atmospheric conditions available within MODTRAN 3.7. The software does not support small, incremental changes in aerosol LOS conditions, e.g., say stratospheric aerosol optical depths in the range of 0.010 to 0.050 at 0.005 increments.

Limitations applying specifically to the automated sea ice retrieval are:

- Clear conditions only. The definition of "clear" will be developed in coordination with the development of the VIIRS Cloud Mask IP *[Y2412]*. It will depend upon the capability of the cloud mask over snow and ice surfaces and upon the capability of radiative transfer modeling through thin clouds.

5.0 REFERENCES

Ackerman, S. A., K. Strabala, P. Menzel, R. Frey, C. Moeller, L. Gumley, B. Baum, C. Schaaf, and G. Riggs (1997). Discriminating Clear-Sky From Cloud With MODIS Algorithm Theoretical Basis Document (MOD35). Version 3.2

Allen, R. C., P. A. Durkee, and C. H. Wash (1990). Snow/cloud discrimination with multispectral satellite measurements. *J. Appl. Met.*, 29, 994-1004.

Bohren, C.F., and B.R. Barkstrom (1974). Theory of the optical properties of snow. J. Geophys. Res., 79, 4527-4535.

Bolsenga, S.J. (1983). Spectral reflectances of snow and fresh-water ice from 340 through 1100 nm. J. Glaciology, 29(102), 296-305.

Crane, R.G. and M.R. Anderson (1984). Satellite discrimination of snow/cloud surfaces. Intl. J. Remote Sens., 5(1), 213-223.

Dozier, J. (1984). Snow reflectance from Landsat-4 Thematic Mapper. IEEE Trans. Geosci. Remote Sens., 22(3), 323-328.

d'Entremont, R. P., Thomason, L. W. and J. T. Bunting, 1987: "Color composite image, processing for multispectral meteorological satellite data, *Proceedings of SPIE - The International Society for Optical Engineering*, pp. 96-106, Cambridge, MA.

Dozier, J. (1989). Spectral signature of alpine snow cover from the Landsat Thematic Mapper. Remote Sens. Environ., 28, 9-22.

Grenfell, T.C., D.K. Perovich, and J.A. Ogren (1981). Spectral albedos of an alpine snowpack. Cold Regions Sci. Technol., 4, 121-127.

Hutchison, K. D., VIIRS Risk Reduction Plan for Manually-Generated Cloud Products, Raytheon Information and Technical Systems, Version 1.0, Revision 0.1, May, 1999.

Hutchison, K. D., VIIRS Imagery Flowdown Results , EDR: Manually-Generated Cloud Products from Imagery, October, 1998.

Hutchison, K., and P. Janota, "Cloud Models Enhancement Project Phase 1 Report," The Analytic Sciences Corporation (TASC), Technical Report TR-5773-1, August, 1989.

Hutchison, K., Peterson, R., and P. Janota, "Cloud Models Enhancement Project Phase 2 Report," The Analytic Sciences Corporation (TASC) Technical Report TR-5773-2, August, 1990.

Hutchison, K. D., and J. K. Locke (1997). Snow identification through cirrus cloudy atmospheres using AVHRR daytime imagery," Geophysical Research Letters, 24, 1791-1794

Hutchison, K. D., B. J. Etherton, and P. C. Topping (1997). Validation of automated cloud top phase algorithms: distinguishing between cirrus clouds and snow in a-priori analyses of AVHRR imagery. Optical Engineering, 36, 1727-1737

Liou, K-N. (1980). An Introduction to Atmospheric Radiation. Academic Press.

Mannen, J. T. (1996). Cost and Operational Benefits Requirements Analysis Report (COBRA), NPOESS Integrated Program Office, June 12, 1996.

Scorer, R. S. (1990). Satellite as Microscope. Ellis Horwood Limited.

Thomas, G., and K. Stamnes (1998). Radiative transfer in the atmosphere and ocean. Textbook, Cambridge Atmospheric and Space Sciences Series.

Valovcin, F. R. (1978). Spectral radiance of snow and clouds in the near infrared spectral region, AFGL-TR-78-0289, Air Force Geophysics Laboratory, Hanscom AFB, MA.

Warren, S.G. (1982). Optical properties of snow. Rev. Geophys. Space Phys., 20(1), 67-89.

Warren, S.G., and W.J.Wiscombe (1980). A model for the spectral albedo of snow.II. Snow containing atmospheric aerosols, J. Atmos. Sci., 37(12), 2734-2745.

Wiscombe, W.J., and S.G. Warren (1980). A model for the spectral albedo of snow,1,pure snow. J. Atmos. Sci., 37(12), 2712-2733.

Raytheon

APPENDIX A

VIIRS USER'S GUIDE

1. INTRODUCTION

The current DMSP OLS and TIROS AVHRR sensors have limited spectral content compared to the VIIRS sensor designed by Raytheon. While MODIS will provide the research community with a significantly enhanced capability, the operational community will not fully realize the value of these data until the launch of the NPOESS VIIRS sensor. In the interim, research scientists will continue to improve the algorithm technology and MODIS-derived environmental data products (EDRs). Thus, it becomes essential that the algorithm technology and user knowledge be brought forward together in order to fully realize the value of true multispectral VIIRS measurements. The Raytheon VIIRS User's Guide is recommended as THE vehicle to convey VIIRS algorithm technology to the operational user community.

Raytheon's goal in preparing this appendix is to begin the documentation process necessary for creating a VIIRS User's Guide. Our ultimate goal is to publish a manual which (1) examines the theoretical basis for feature identification in VIIRS imagery and (2) provides users of VIIRS data with the knowledge needed to fully utilize these data to address their unique mission requirements. In addition, Raytheon plans to routinely conduct training sessions in a classroom environment to users of NPOESS VIIRS data.

2. THEORECTICAL BASIS FOR FEATURE IDENTIFICATION

As noted in the Section 3.4.3.1 of the Imagery ATBD, the ability to manually identify clouds in multispectral imagery is based upon the capability of the VIIRS imagery to maximize the contrast between the cloud and its cloud-free (surrounding) environment. This process may be described more precisely by Equation I.

$$C = I_v(0)_{cloud} / I_v(0)_{background} \tag{A-1}$$

The satellite observed radiance, $I_v(0)$, may be composed of (1) reflected solar radiation, (2) thermal radiation emitted by terrestrial features, or (3) both when observations are made in the 3-5 mm wavelength region. However, for cloud-free conditions, the monochromatic, terrestrial radiation is described by Equation II:

$$I_v(0) = \varepsilon_v B_v\left[\mathsf{T}_s\right] T_v\left(p_s\right) + \int_{p_s}^{0} B_v\left[\mathsf{T}(p)\right]\frac{f T_v(p)}{f p}\,dp + \left(1 - \varepsilon_v\right)\int_{0}^{p_s} B_v\left[\mathsf{T}(p)\right]\frac{f T_v(p)}{f p}\,dp \tag{A-2}$$

and:

$\quad\quad v \quad\quad\quad\quad\quad$ = wavenumber of emission

$\quad\quad B_v\left[\mathsf{T}(p)\right] \quad\quad$ = Planck function at wavenumber (v) for temperature (T)

ε_v = emissivity of surface at wavenumber (v)

$T_v(p_s)$ = atmospheric transmittance between pressure level (p_S) and space

$I_v(0)$ = monochromatic radiance arriving at satellite.

p_s = surface pressure

T_s = surface temperature

For imaging sensors, the atmospheric transmittance between pressure levels and space is very small and Equation (II) is closely approximated by Equation (III), which shows that the radiance arriving at the satellite sensor is a function of the emissivity of the surface, the surface temperature, and the transmission from the surface to the sensor:

$$I_v(0) = \varepsilon_v B_v \lfloor T_s \rfloor T_v(p_s) \tag{A-3}$$

Therefore, the real goal of the Raytheon VIIRS User's Guide is to provide the meteorological satellite analyst with the knowledge base to fully exploit differences between feature emissivity, feature temperature, and/or atmospheric attenuation of features in multispectral imagery in order to positively identify each feature in the VIIRS data set.

In addition to spectral signatures, some features are unique identified by spatial, textural, and thermal signatures. For example, cirrocumulus associated with strong vertical motions near the core of the jet stream may be uniquely identified by its fishbone effect when these clouds appear much like the skeleton of a fish. In addition, wind speed, direction, and the potential of severe turbulence may be assumed by the presence of wave (lenticular) clouds in the lee of a mountain range. Finally, clouds types are often distinguished only by their vertical location in the atmosphere which can be determined from the cloud top temperature. Thus, using cloud top versus cloud-free surface temperatures of neighbor pixels is often adequate to differentiate low level water clouds (e.g. stratus) from middle-level water clouds (e.g. altostratus). Given additional information from other NPOESS sensors, such as rainfall occurrence from the microwave imagery, it becomes possible to differentiate between altostratus and nimbostratus solely from satellite data.

3. VIIRS BAND SELECTION PROCESS

Bands selection for the Raytheon VIIRS sensor design is based upon the strength (strong and/or weak) of three components that make up the signatures of each feature. These components are: (a) surface radiance which includes temperature and emissivity or solar reflectivity, (b) cloud absorptivity or reflectivity, and atmospheric transmissivity. Examples of these features in several VIIRS channels are shown in Figure A-1.

The positive identification of clouds in multispectral imagery requires that the analyst understand and exploit the properties of water droplets and ice crystals, along with the spectral characteristics of different backgrounds in VIIRS imagery and imagery-assist bands. A

discussion of the phenomenology associated with the features follows along with the definition of bands selected to meet VIIRS threshold and objective requirements for the manually-generated cloud cover EDR, in Section 4.

4. PHENOMENOLOGY FOR SELECTION OF IMAGERY CHANNELS AND IMAGERY-ASSIST BANDS FOR MANUALLY-GENERATED CLOUD COVER EDR

The VIIRS SRD specifies that the spectral bandpasses required to meet the threshold requirements for the manually-generated cloud cover EDR and cloud type EDR must be at the "imagery" resolution. The flowdown of these requirements determined that only three spectral bands were required to meet the threshold requirements (Hutchison, 1998). However, the Raytheon cloud and imagery IPTs also demonstrated the use of imagery bands with imagery-assist data, collected at a more coarse resolution, to advance toward meeting objective requirements, especially for the cloud typing EDR. Therefore, this section begins with a discussion of the phenomenology associated with the selection of the VIIRS imagery channels in the Raytheon design. Subsequently, the phenomenology associated with non-imagery channels is presented for the bands which provide useful information for the manual detection of clouds and their classification by type.

Figure A-1. Reflectivity, absorptivity, and transmissivity of atmosphere, surface and clouds for several VIIRS channels.

Figure A-1 shows the band positions for VIIRS channels 1, 7, 8, and 9 (---) along with atmospheric transmissivity (---), reflectivity of vegetated (---) and bare soil (---) ice (white) and water surfaces (---), solar irradiance (gold), and imaginary components of the index of refraction for water (---) and ice (---).

4.1. VIIRS Imagery Channels

The SRD states that "At a minimum, at least one daytime visible, one daytime/nighttime visible, and one IR channel shall meet the explicit imagery requirements." The Raytheon sensor design called for the identification of the least number of imagery channels required to satisfy minimum (threshold) requirements for manually-generated cloud data product EDRs. All other VIIRS channels would be collected at the lower (non-imagery) resolution.

4.1.1 Daytime Visible Imagery Channel

The Raytheon daytime visible imagery is centered at 0.645 microns. The justification for this selection is shown in Figure 2.

Figure 2 shows the location and spectral response function for the daytime visible channel, i.e. VIIRS 5(i) imagery along with the characteristics of the Earth-atmosphere system. It is clear that the reflectivity of vegetated land is very small in this band but it begins to increase quite rapidly at ~ 0.7 microns. By limiting the width of the band between 0.6-0.7 microns, we also avoid the water vapor absorption lines in the 0.7-0.8 micron region which could cause variations in cloud and land signatures. The reflectivity of water surfaces is even lower. On the other hand, the reflectivity of clouds is much larger which means this band is particularly valuable for discriminating between clouds and vegetated land and ocean surfaces. Additionally, the reflectivity of snow is very high. Therefore, this channel is not good for differentiating between snow and clouds nor is it particularly useful for identifying boundaries between land and ocean surfaces.

Figure A-2. Phenomenology of the 645 nm band which is the daytime imagery channel of the Raytheon VIIRS design.

Examples of MODIS imagery collected in the narrow band will be included in future revisions of the document after EOS MODIS Terra data become available through the EOSDIS. Until that time, the AVHRR Channel 1 image in Figure A-3 is used to illustrate the features in this spectral band.
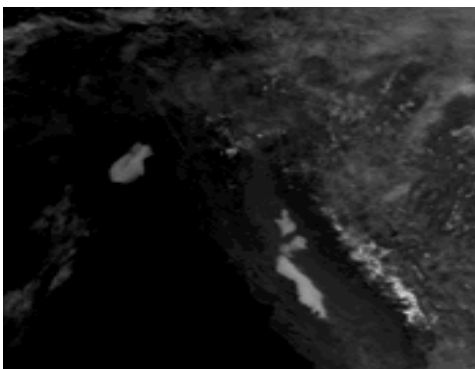
Figure A-3. AVHRR Channel 1 Imagery.

4.1.2. VIIRS Infrared Imagery Channel

Figure A-4 shows the location and spectral response function for the VIIRS infrared channel, i.e. VIIRS 12(i) imagery along with the characteristics of the Earth-atmosphere system

Examples of MODIS imagery collected in the narrow band will be included in future revisions of the document after EOS MODIS Terra data become available through the EOSDIS. Until that time, an AVHRR Channel 4 image shown in Figure 5 is used to illustrate the features in this spectral band.
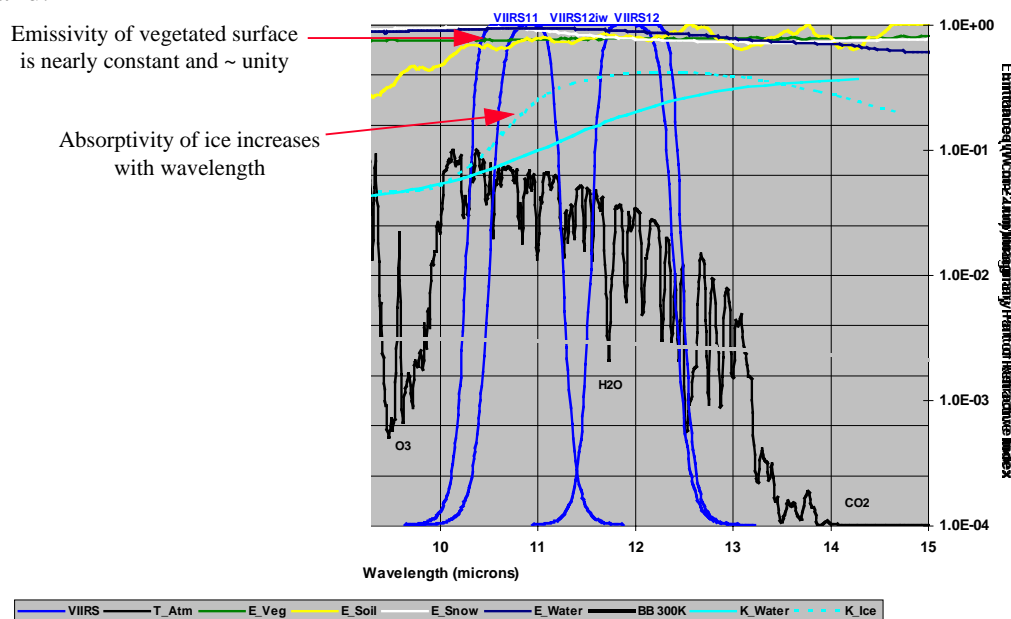
Figure A-4. Phenomenology of VIIRS 12I (imagery) channel shows water vapor absorption across band.

The VIIRS 12I (imagery) channel is valuable for estimating the true radiating temperatures of objects in the band after correcting for atmospheric water vapor attenuation, which makes the measured cloud top temperature slightly colder than its true radiating temperature. In addition, due to the high absorptivity of ice at these wavelengths, thin cirrus is often easily detected in nighttime conditions, when other VIIRS data in the 1.378 micron band are not available. The AVHRR channel 5 imagery shown in Figure A-5 shows the presence of thin cirrus in this bandpass.
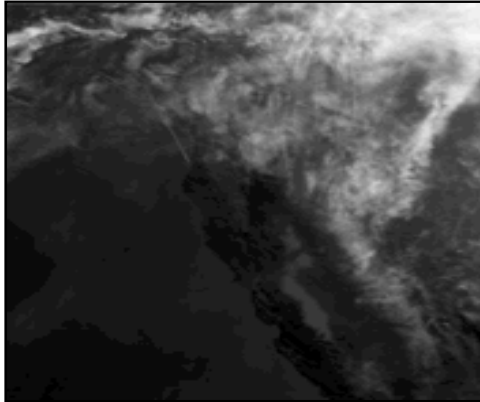
Figure A-5. AVHRR Channel 5 imagery

4.1.3. VIIRS Mid-Wave Infrared Imagery Channel

In addition to the minimum required daytime visible and infrared imagery channels, the Raytheon design includes a mid-wavelength infrared imagery channel, centered near 3.7 microns, and shown in Figure 6 for VIIRS 10(i) imagery.
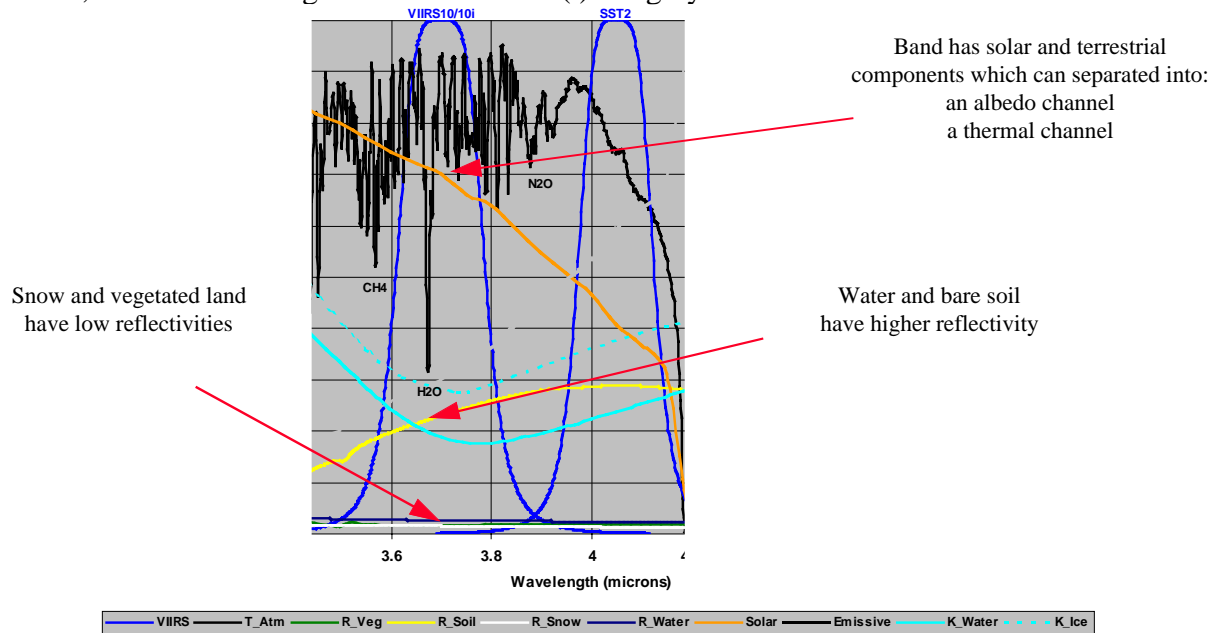
Figure A-6. Phenomenology of the 3.7 nm band which is a mid-IR imagery channel of the Raytheon VIIRS design.

Figure A-6 shows water vapor absorption lines in the VIIRS 10(i) imagery channel. It also shows that the reflectivity of snow is very low which that of clouds is much larger. It also shows that considerable solar irradiance is present while the reflectivity of bare soil is relatively large compared to snow and clouds. Therefore, the 3.7 micron channel could be useful for differentiating between snow and clouds as well as clouds and vegetated land. However, distinction between cloud and bare soil appears difficult and the presence of terrestrial energy complicates the contrast between snow and clouds.

While the daytime 3.7 micron band imagery channel contains both solar and thermal energy, the capability has been demonstrated to separated this single channel into two channels and thus improve the discrimination between features in the spectral band. This process has been described in the literature (Hutchison et al., 1997) and utilizing the derived albedo channel allows significantly enhances the contrast between snow and water clouds. In fact the procedure also sufficiently enhances the contrast between snow and cirrus (ice) clouds so that snow can be observed through overcast cirrus cloudy conditions. Furthermore, the VIIRS flowdown process demonstrated that the thermal channel proves highly effective at differentiating between water clouds and bare soil. Finally, the nighttime 3.7 micron channel image has been widely used for detection and identification of nighttime stratus, especially when couple with the VIIRS IR imagery channel.

Figure 7. Differentiating between cirrus (ice) clouds and snow is greatly facilitated in the 3.7 μm (albedo) band
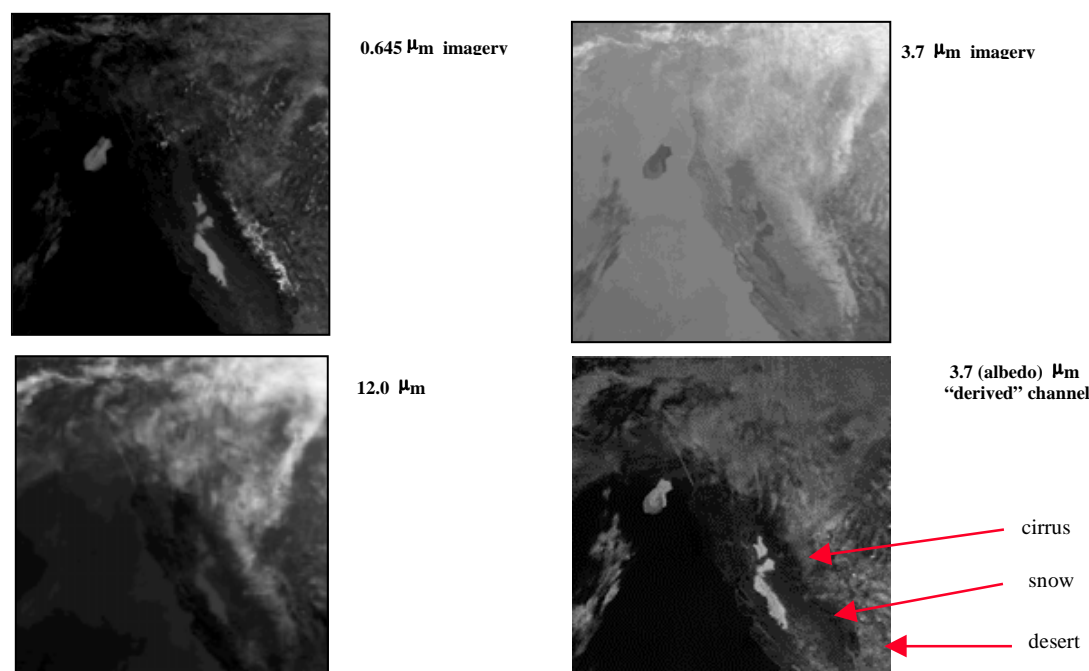
Figure A-7. Differentiating between cirrus (ice) clouds and snow is greatly facilitated in the 3.7 μm (albedo) band.

Figure A-7 shows an AVHRR scene where the 3.7 micron channel has been segregated into the albedo image to enhance the signatures of snow and cirrus clouds (Hutchison and Locke, 1997).

Notice that the snow-covered Sierra Nevada Mountains, in the lower right corner of the scene, appear bright in the 645 nm imagery channel in the upper left panel. However, this same feature appear very dark in the derived 3.7 micron albedo image located in the in the lower right corner. On the other hand, the several areas of water clouds, located to the left of a diagonal from the lower-right to the upper left corner, are unchanged in the scene. Finally, this cirrus clouds, located to the right of this same diagonal, are enhanced in the 3.7 micron albedo image, if in comparison to the 12.0 micron image. Thus, the 3.7 micron image and the derived albedo image assist in identifying nighttime stratus and daytime water clouds, snow fields, and thin cirrus clouds fields.

4.2 VIIRS Imagery-assist Channels

In accordance with VIIRS SRD, non-imagery or imagery-assist channels can be collected at a lower resolution than imagery channels. Imagery-assist channels cannot be used to satisfy minimum system requirements but may be used to press toward satisfying objective level requirements. Raytheon has demonstrated the use of imagery-assist data with imagery for satisfying objective requirements for manually-generated cloud data products (Raytheon SFR, 1999). In this section, we present the phenomenology of some key imagery-assist channels and their application toward meeting VIIRS objective requirements. A more complete description will be provided in the post-PDR era.

4.2.1 The 1.61 Micron VIIRS8 Imagery-Assist Channel

The 1.6 micron band has long been advocated for distinguishing between snow and clouds in multispectral imagery (Valvocin, 1978). Figure 8 shows the reflectivity of ice dropping sharply at ~ 1.4 and reaching a minimum near 1.5 microns before gradually increasing to another maximum at ~ 1.82 microns. At the same time, the reflectivity of water clouds remains considerably higher making the band highly valuable for snow cloud discrimination. On the negative side, the reflectivity of both vegetative land and bare soil are both relatively high with the latter being significantly higher than the former. Thus, water clouds could become misclassified in this band, especially in sparsely vegetated regions. However, as previously noted, the thermal component of the 3.7 micron imagery channel is useful for avoid such misclassifications.
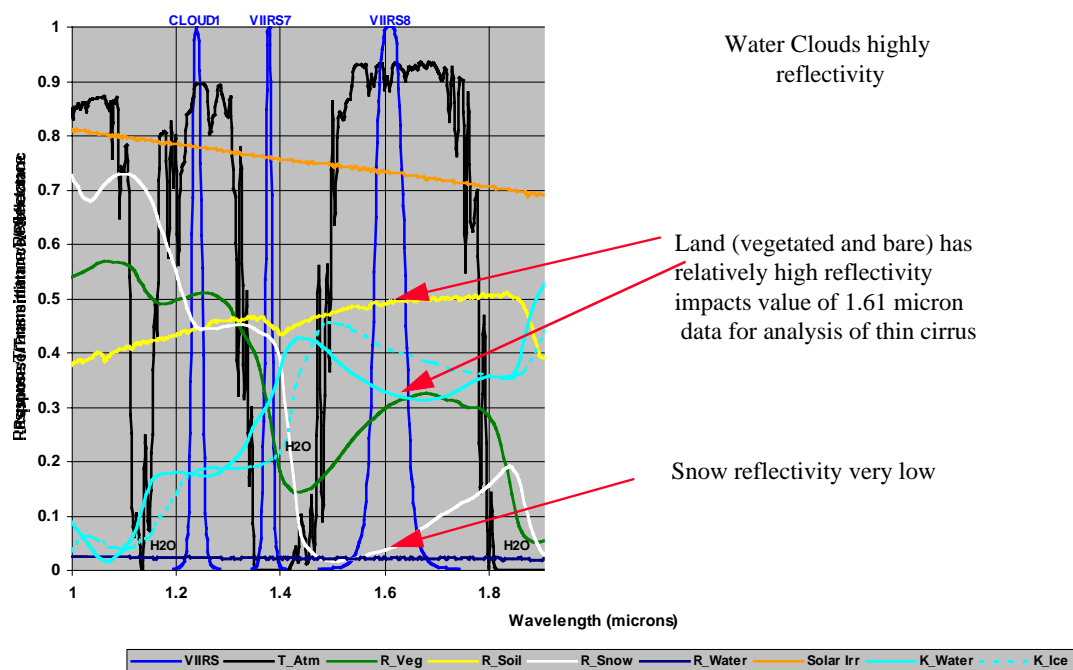
Figure A-8. Phenomenology of the 1.61 micron VIIRS Imagery-Assist Channel.

The phenomenology discussed in Figure A-8 is demonstrated in the LandSat Thematic Mapper Simulator scene shown in Figure A-9 which was collected via an aircraft flight over the Sierra Mountains. In the left panel is shown the 645 nm band while the 1.61 micron imagery is in the right panel. Notice that water clouds and snow fields are both highly reflective at the shorter wavelength. On the other hand, snow becomes very dark, indicative of its poor reflectivity, at the longer wavelength while water clouds remain highly reflective. Thus, discrimination between water clouds and snow fields becomes a trivial matter when both the 0.645 and 1.61 micron data are available.

0.645 micron TMS image   1.61 micron TMS image
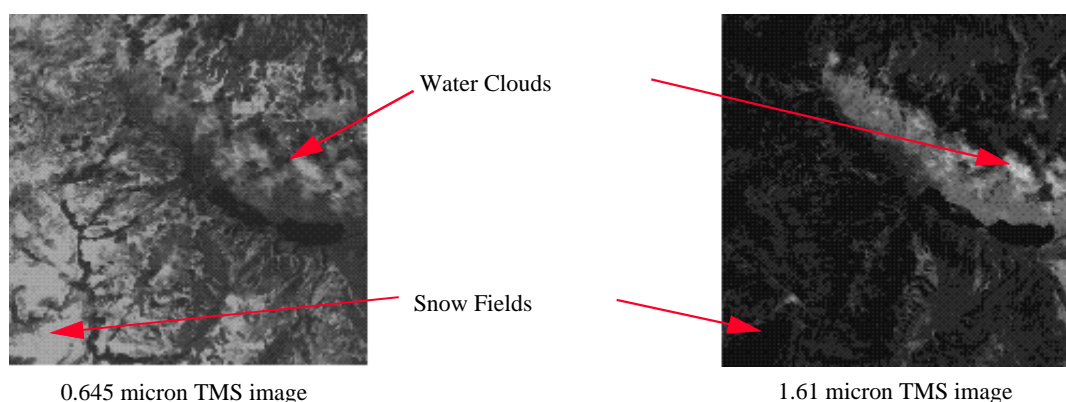
Figure A-9. Water clouds and snow appear similar in 0.645 micron band, but very different in the 1.61 micron channel.

4.2.2 The 1.378 Micron VIIRS7 Imagery-Assist Channel

Data collected in the very narrow band centered on 1.378 microns has been shown to be most valuable for the detection of this cirrus clouds in daytime imagery under most conditions (Gao et al., 1993; Hutchison and Choe, 1996). The value of these data stems from the fact that most existing methods of identifying thin cirrus clouds rely upon imagery bands where water vapor and cirrus have similar spectral signatures which means that water vapor act as noise in the detection of thin cirrus clouds (Hutchison et al., 1995). On the other hand, water vapor strongly absorbs energy at 1.378 microns, as shown in Figure 10, while most surface features, e.g. snow, bare soil, and vegetated land have about the same reflectivities. However, since water vapor density decreases exponentially with altitude in the atmosphere, reflected energy off of lower-level features will be totally absorbed under most circumstance. Thus, only middle level water and higher level cirrus clouds, which occur above the moist layers of the atmosphere, reflect enough energy to be detected by space-based observing systems.
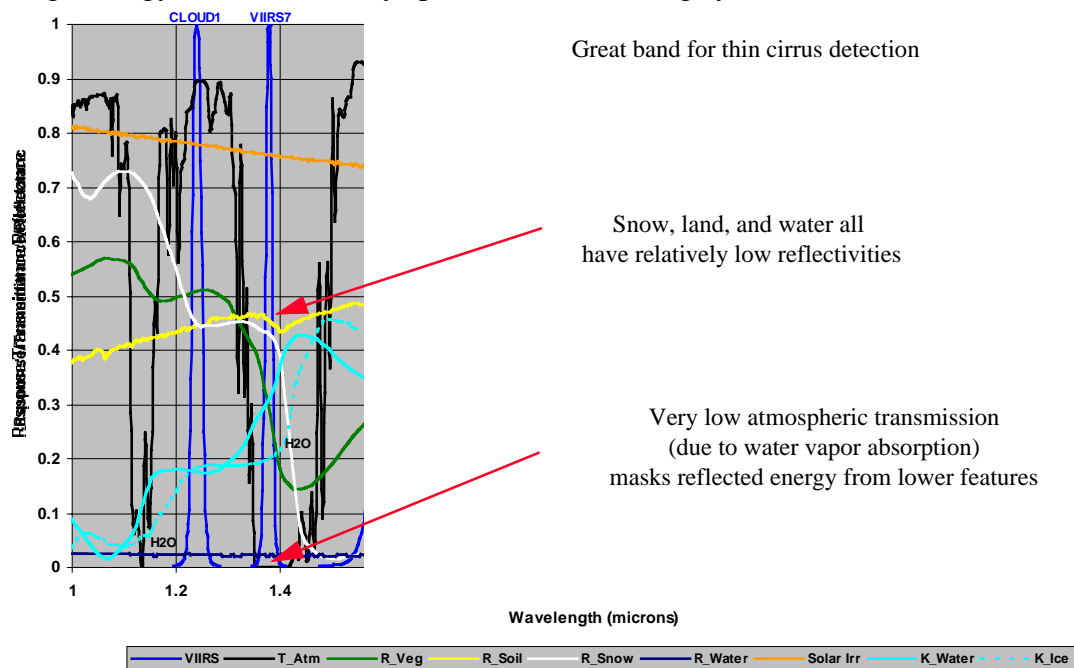
Figure A-10. Phenomenology of the 1.378 micron channel used for thin cirrus detection.

The phenomenology described in Figure A-10 is demonstrate in Figure A-11 and Figure A-12. In the first case, data collected over Coffeyville, KS shows an apparently cloud-free day based upon the 1.61 micron imagery in the left panel. However, the 1.38 micron band in the right panel shows the scene is nearly completely overcast with thin cirrus. Lidar measurements made in conjunction with NASA's First ISCCP Regional Experiment (FIRE) confirmed the presence of the cirrus clouds.

| 1.61 micron AVIRIS Channel | 1.378 micron AVIRIS Channel |
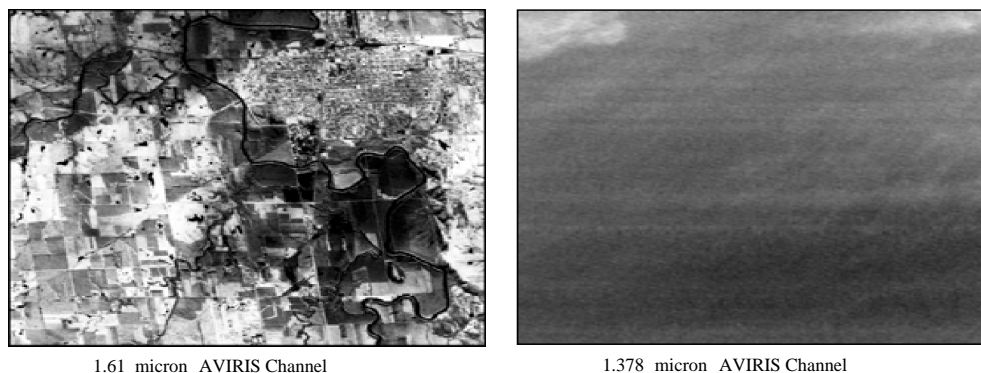
Figure A-11. Improved cirrus detection is also possible in the 1.378 micron channel over highly reflective (land) surfaces.

In Figure A-12, cirrus and lower-level water clouds appear in the 645 nm channel of Advanced Visible/InfraRed Imaging Spectrometer (AVIRIS) data collected over the Gulf of Mexico shown in the left panel. In the right panel the same scene is viewed in a 10 nm wide band centered at 1.375 microns. In this case, there is sufficient water vapor present in the atmosphere to absorb any solar energy which may have been reflected by the lower-level water clouds. Thus, only energy reflected off the cirrus clouds arrives at the detector.

| 0.645 micron AVIRIS Channel | 1.378 micron AVIRIS Channel |
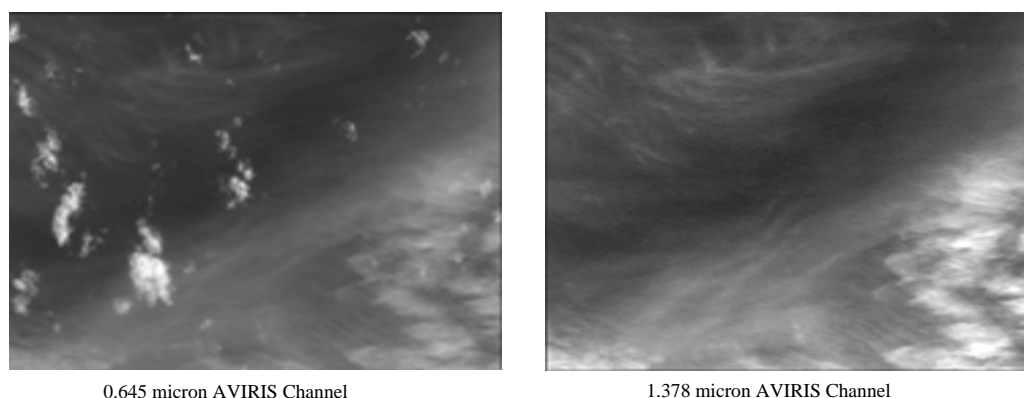
Figure A-12. Cirrus clouds are readily detected in the 1.378 micron channel, even in the presence of lower level water clouds.

4.2.3 The 865 Nanometer VIIRS6 Imagery-Assist Channel

The phenomenology associated with the 865 nm VIIRS imagery-assist channel is shown in Figure A-13. Data in this channel have been widely used with those in the 645 nm imagery band to create a vegetative index which measures the "greenness" of the Earth. The reasons are clearly shown in the figure. The reflectivity increases rapidly at wavelengths above 70 nm and becomes nearly constant between ~ 77 nm and 1.0 micron. On the other hand, the atmosphere has numerous water vapor absorption lines above 90 nm. The VIIRS6 imagery assist band is located in the region where atmospheric transmissivity is effected only slightly by atmospheric gases that have variable concentrations on a global scale. Therefore, highly accurate vegetative indices are expected.
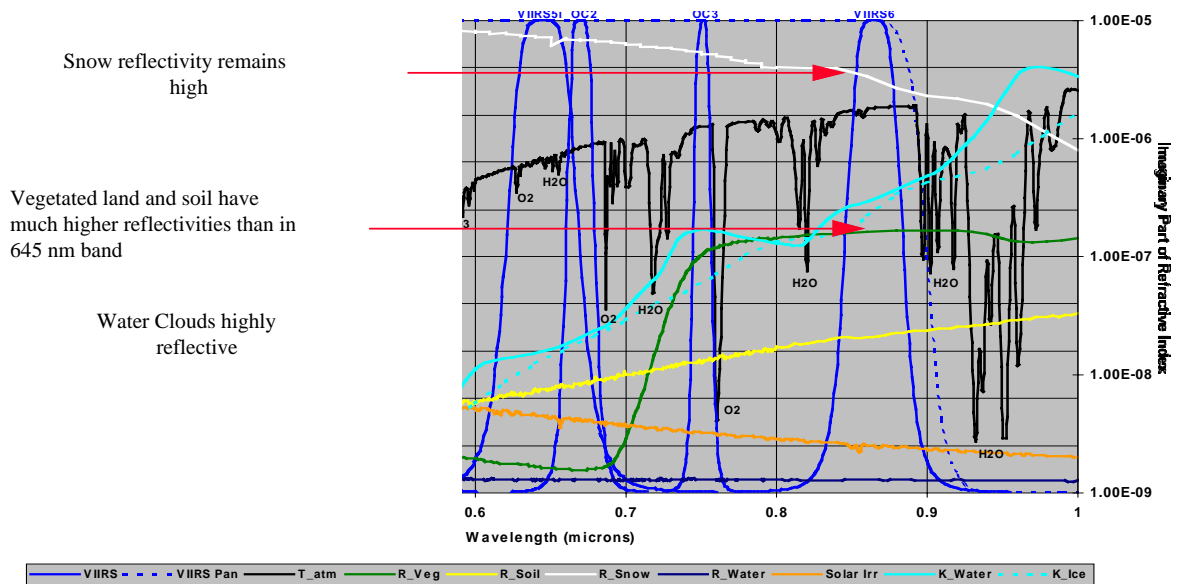
Figure A-13. Phenomenology of the VIIRS6 Imagery-Assist Channel.

The reflectivity of water remains very low in the 865 nm band which makes these data ideal for distinguishing between land and water boundaries. Meanwhile, the reflectivity of snow remains very high in this band when compared to the 645 nm imagery channel. Thus, the 865 nm channel has no value for snow cloud discrimination. Optimum snow cloud uses the 645 nm band along with the 1.61 and 3.7 micron data.

A comparison of Figure 14 with Figure 2 reveals the value of the 865 nm channel for land sea discrimination. Vegetated land and bare soil both are highly reflective in the larger wavelengths while the ocean is a poor reflector at the 865 nm wavelength. Thus, land-sea boundaries are very pronounced in the 865 nm image-assist band.
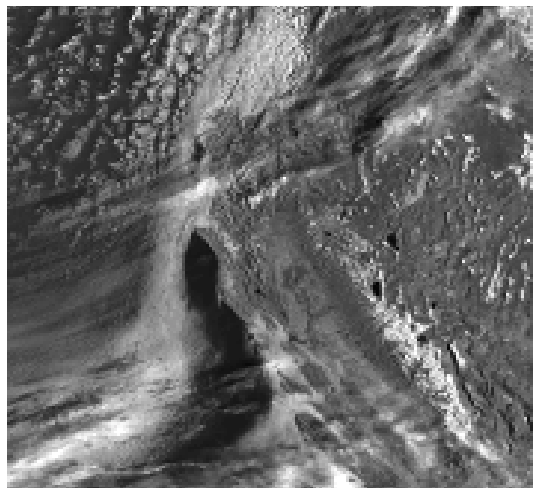
Figure A-14. Signatures in AVHRR Channel 2.

7. REFERENCES

Hutchison, K. D. and J. K. Locke, 1997: "Snow Identification through Cirrus Cloudy Atmospheres using AVHRR Daytime Imagery," Geophysical Research Letters, **24**, 1791-1794

Hutchison, K. D., B. J. Etherton, and P. C. Topping, 1997: "Validation of Automated Cloud Top Phase Algorithms: Distinguishing Between Cirrus Clouds and Snow in A-priori Analyses of AVHRR Imagery," Optical Engineering, **36**, 1727-1737

Hutchison, K. D. and N. Choe, 1996: " Application of 1.38-μm Imagery for Thin Cirrus Detection in Daytime Imagery Collected Over Land Surfaces," International Journal of Remote Sensing, **17**, 3325-3342

Hutchison, K. D., Hardy, K., and Gao, B. C., 1995: "Improved Detection of Optically-Thin Cirrus Clouds in Nighttime Multispectral Meteorological Satellite Imagery using Total Integrated Water Vapor Information," Journal of Applied Meteorology, **34**, 1161-1168

Valovcin, F. R., 1978: Spectral radiance of snow and clouds in the near infrared spectral region, Technical Report AFGL-TR-78-0289, 46 pp., Air Force Geophysics Laboratory, Bedford, MA.

APPENDIX B   RGB COMPOSITES

The following Red Green Blue (RGB) Color Composites have been selected due to their spectral content. They are useful to an analyst in Cloud Type determination as well as Cloud vs. Snow/Ice background discrimination. These RGBs have been generated using 3 MAS scenes from the SUCCESS and ARMCAS MODIS Campaigns. The features identified in each RGB are explained in the subcaption.
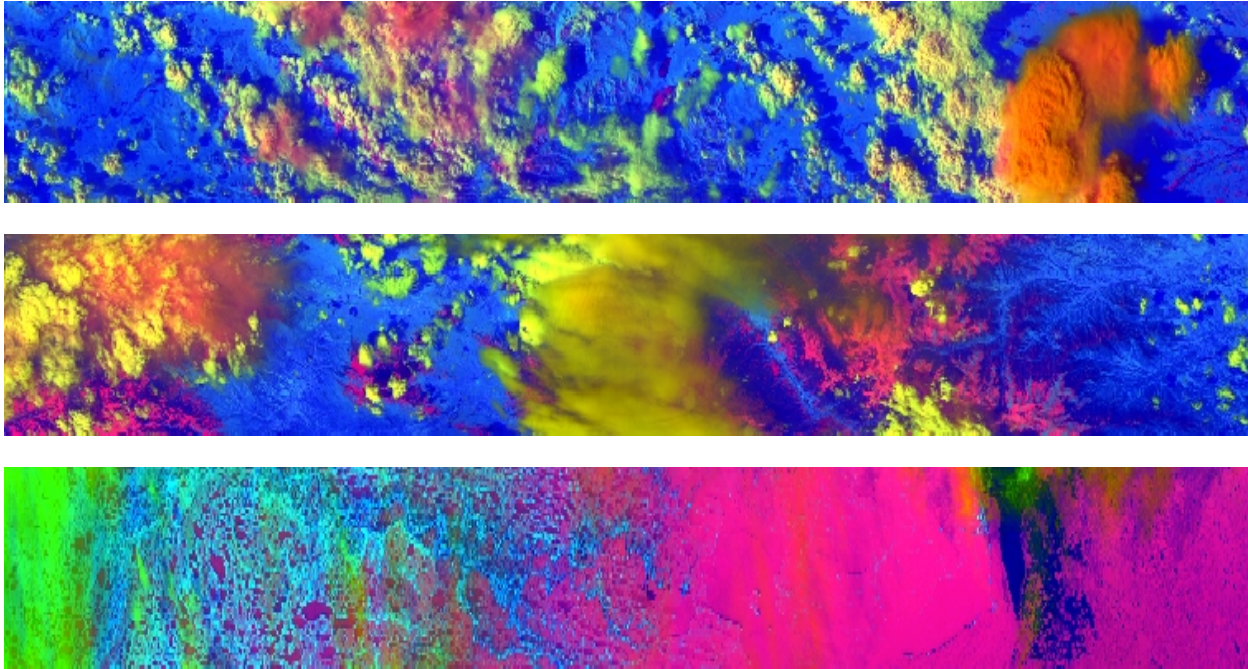
Figure B-1.   RGB (0.645, 1.61, BT10.8./BT12.0)

Using this RGB composite snow/ice surfaces are rose to purple, low clouds are yellow, high (water) clouds range from yellow to green, thin cirrus over snow/ice is orange in coloration, and vegetated land is blue. The thunder cloud in the middle scene is believed to be orange due to the high reflectance in the visible and absorption in the near IR of the ice contained at its upper levels.
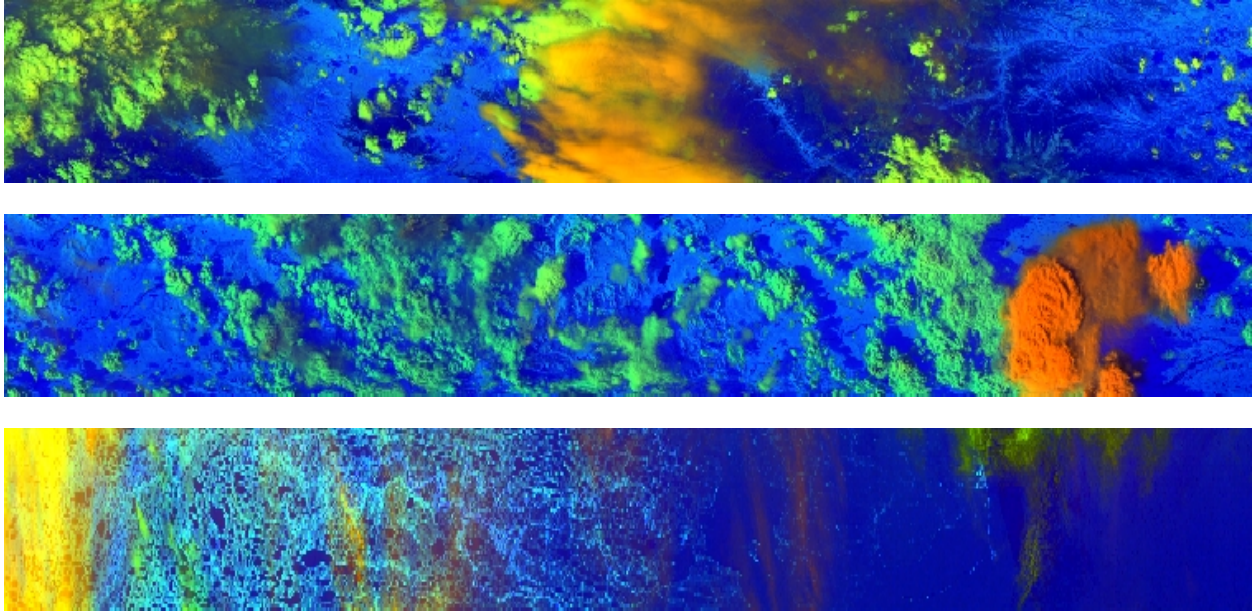
Figure B-2.   RGB (1.38[1.88], 1.61, 12.0)

Using this RGB composite masks out snow ice fields making them the same coloration as vegetated land. Land which has a low amount of vegetation tends to be aqua blue. Optically thin cirrus has a deep bluish hue, lower level water clouds appear greenish, optically thick cirrus are more golden to orange in coloration. Overshooting tops such as the thunder cloud in the middle figure appear orange in coloration..
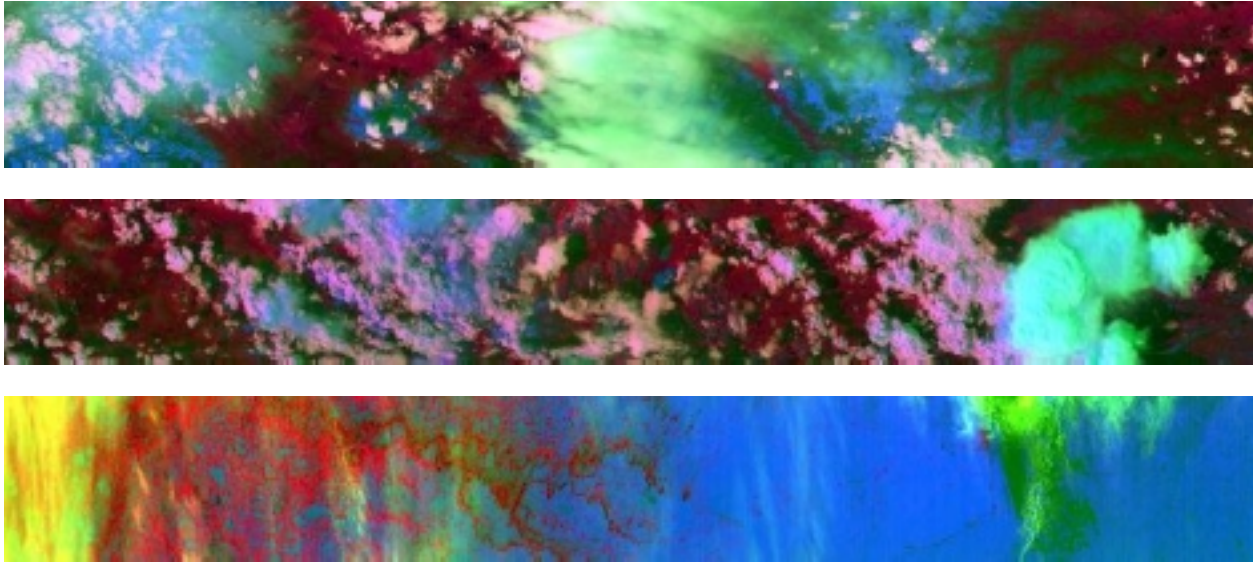
Figure B-3.   RGB (1.61, Invert BT8.6, 0.645)

Using this RGB composite one can distinguish between lower level cumulus and upper level cirrus and snow/ice fields. Snow/ice fields are blue from the 0.645 imagery. Optically-thin cirrus has a yellow-greenish-turquoise hue, lower-level water clouds are rose to white, overlaying mid-level water clouds are darker blue. Vegetated surfaces are red in coloration.
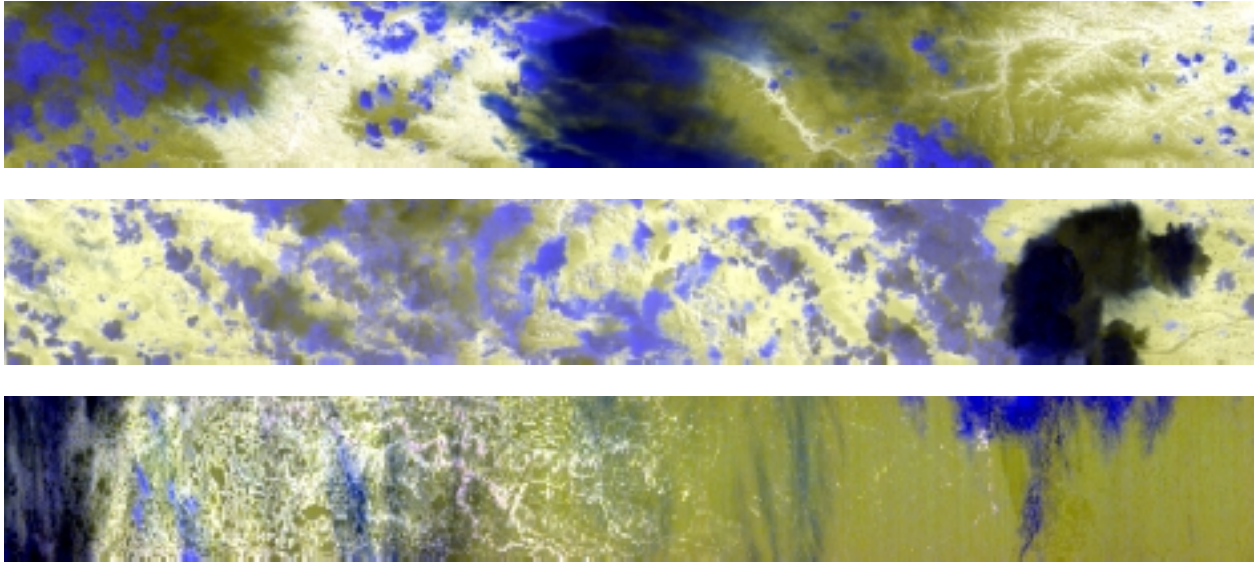
Figure B-4.   RGB (BT11, BT8.6, BT3.75)

Using this RGB composite one can distinguish between lower level Cumulus and upper level Cirrus and snow/ice fields. Snow/ice fields are olive-green, optically thin cirrus has a deep blue-blackish hue over land and blue over ice, lower level water clouds are dark blue, vegetated regions tend to be white. Overshooting tops such as the thunderstorm in the middle figure appear black with clearly defined boundaries, and cellular structure clearly visible.
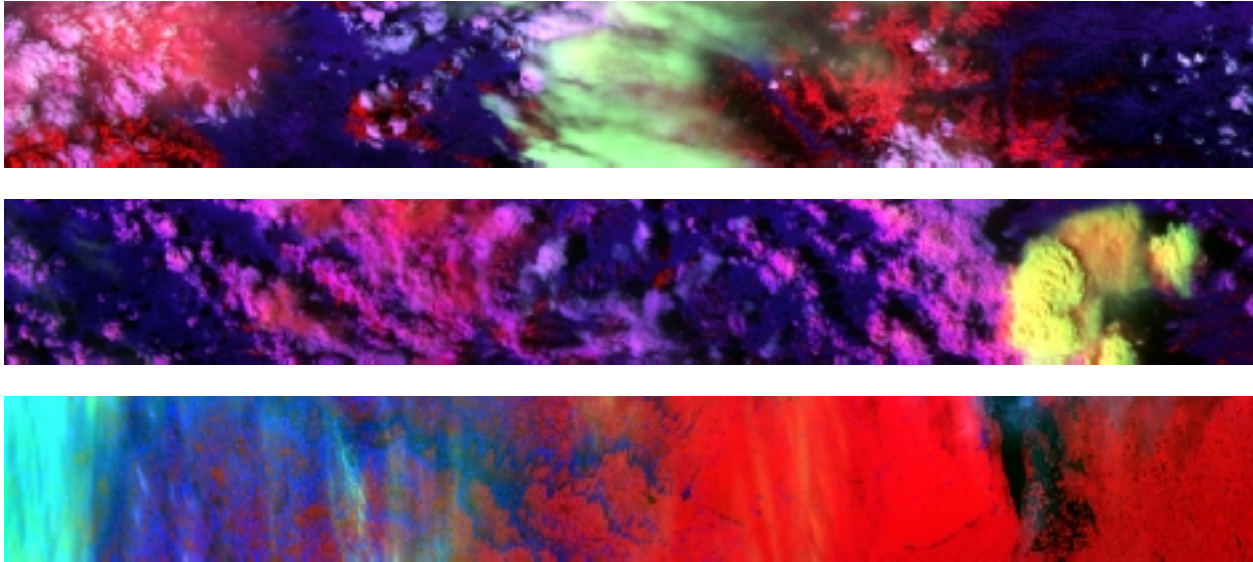
Figure B-5.   RGB (0.645, 1.38[1.88], 1.61)

Using this RGB composite allows distinction between lower level cumulus and upper level cirrus and snow/ice fields. Snow/ice fields are red in coloration, optically-thick cirrus is green in coloration and thin cirrus is aqua blue, lowest level water clouds appear dark purple, while middle level appear pin. Overshooting tops from thunderstorms, such as the middle figure, appear yellow with lower cellular structure being orange.

Raytheon
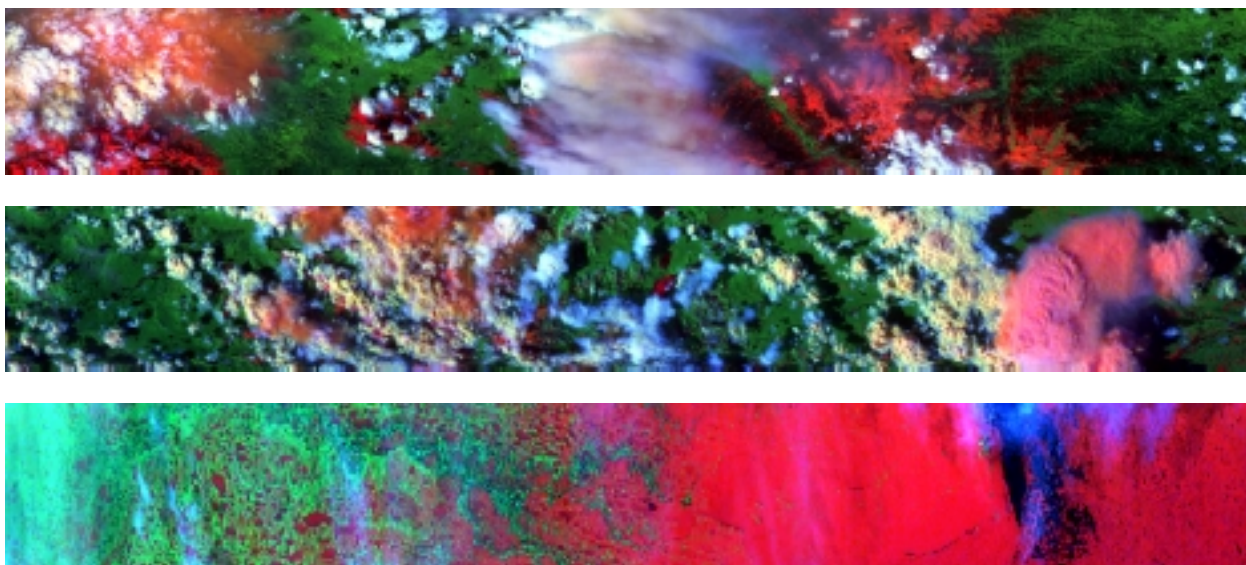
Figure B-6.   RGB (0.645, 1.61, 3.75A)

Using this RGB composite vegetated land is green, low level water clouds are white, high level cirrus are Grey blue, snow/ice is bright red, and thin cirrus over snow/ice is pink to purple, while over vegetated land it is aqua green. The thunder cloud in the middle scene is pink in coloration.
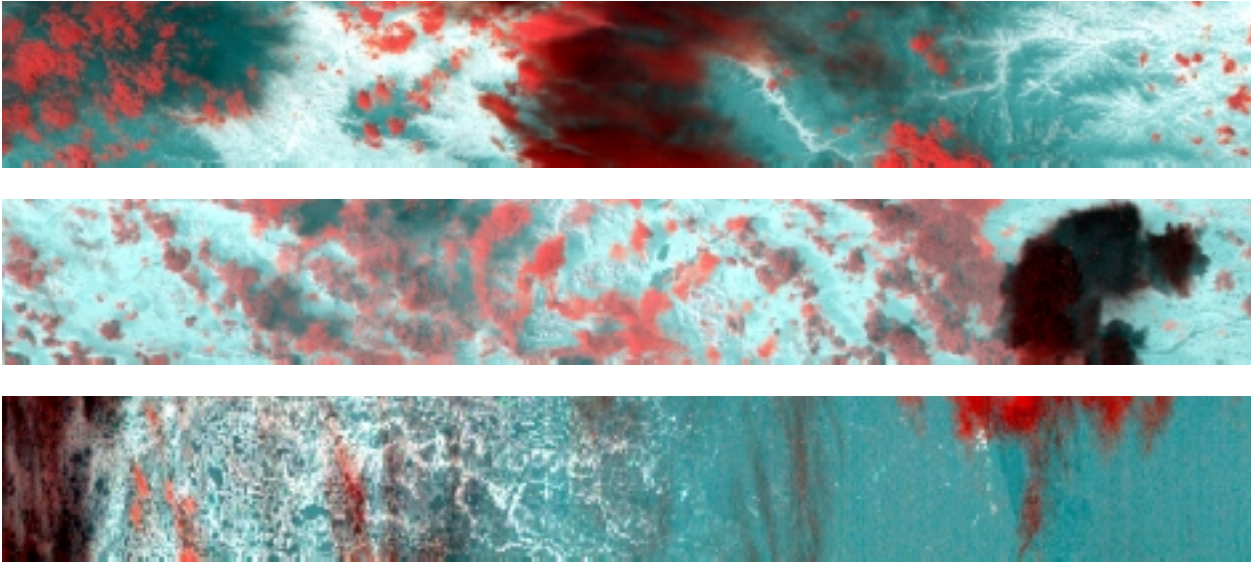
Figure B-7.   RGB (BT3.75, BT10.8, BT12)

Using this RGB composite snow/ice surfaces are blue-gray, water clouds are bright red over vegetated land, cirrus covered regions are black to gray, thin cirrus over ice is bright red, and vegetated land is white. The cells of the thunder cloud in the middle image are clearly visible.
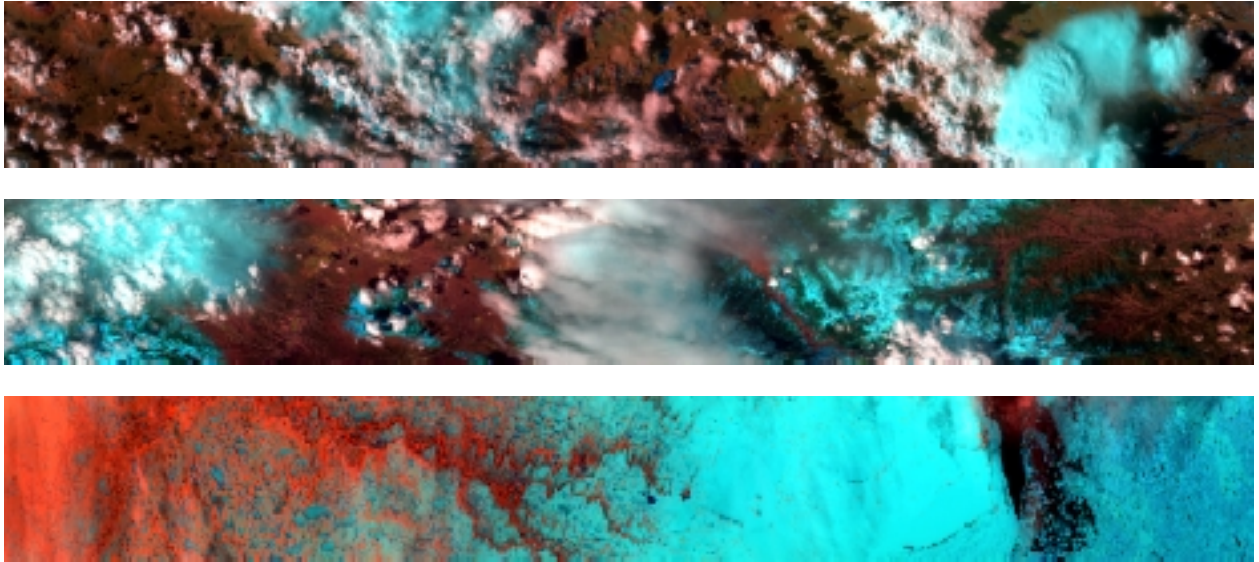
Figure B-8.   RGB (2.1/1.6, .845, .645)

Using this RGB composite snow/ice surfaces are aqua blue, clouds are white, vegetated land is red, and highly vegetated land such as irrigated regions are green. Above note the middle thunder cloud scene optically thin clouds over snow/ice surfaces and clouds that contain a large quantity of ice crystals may be blue in coloration.
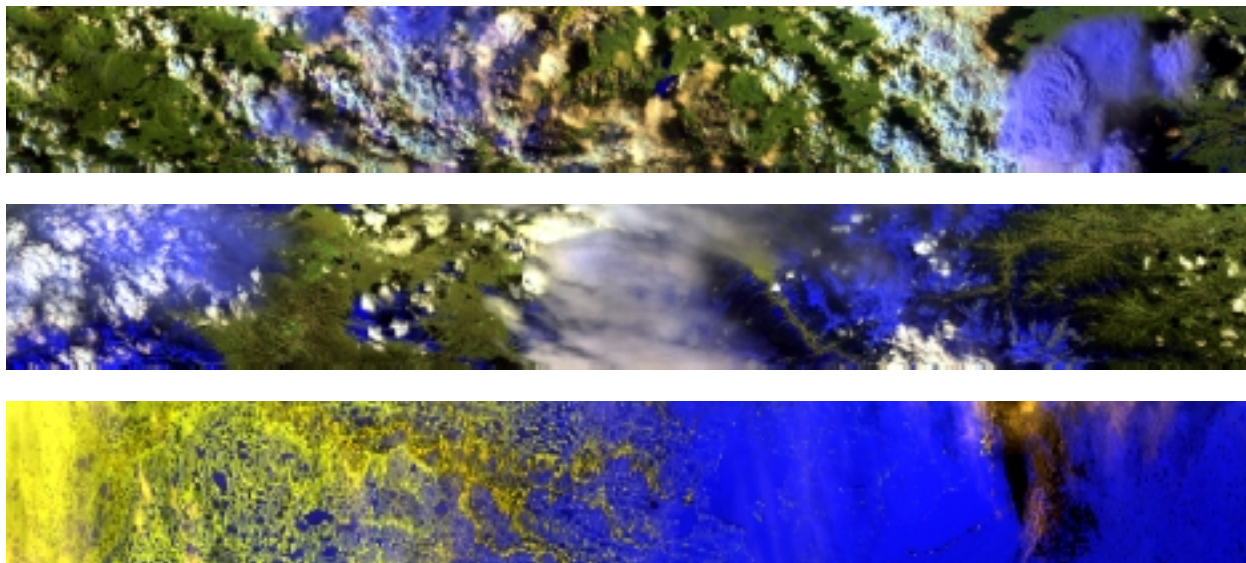
Figure B-9.   RGB (2.1, 1.6, .645)

Using this RGB composite snow/ice surfaces are dark blue, water clouds are white, vegetated land is green, and highly vegetated land such as irrigated regions are dark green. Above note the middle thunder cloud scene optically thin clouds over snow/ice surfaces and clouds that contain a large quantity of ice crystals may be blue in coloration. The vegetated regions with this RGB combination also tend to exhibit greater degrees of contrast, due to the range of reflectances that vegetated surfaces may have in the near IR bands.

Raytheon
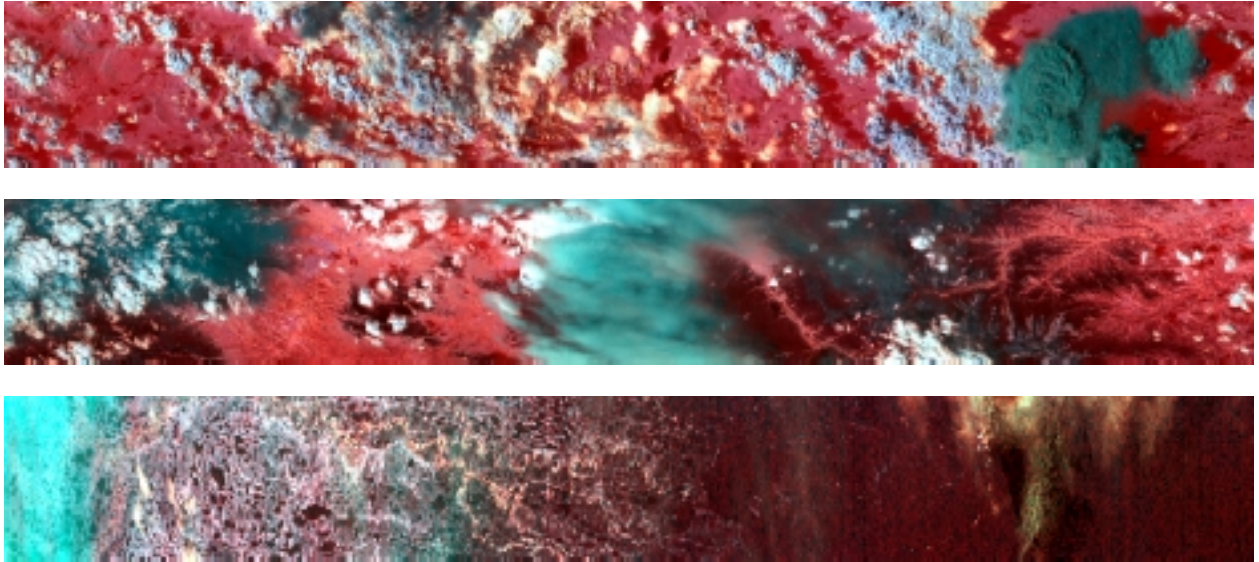
Figure B-10. RGB (BT3.75, 2.1, 1.6)

Using this RGB composite vegetated land is bright red and snow/ice surfaces are dark black. Low level water clouds are white, while higher level cirrus clouds are blue when optically thin and grayish blue when optically thick. This variation in coloration for higher and lower level clouds allows visual discrimination between them.
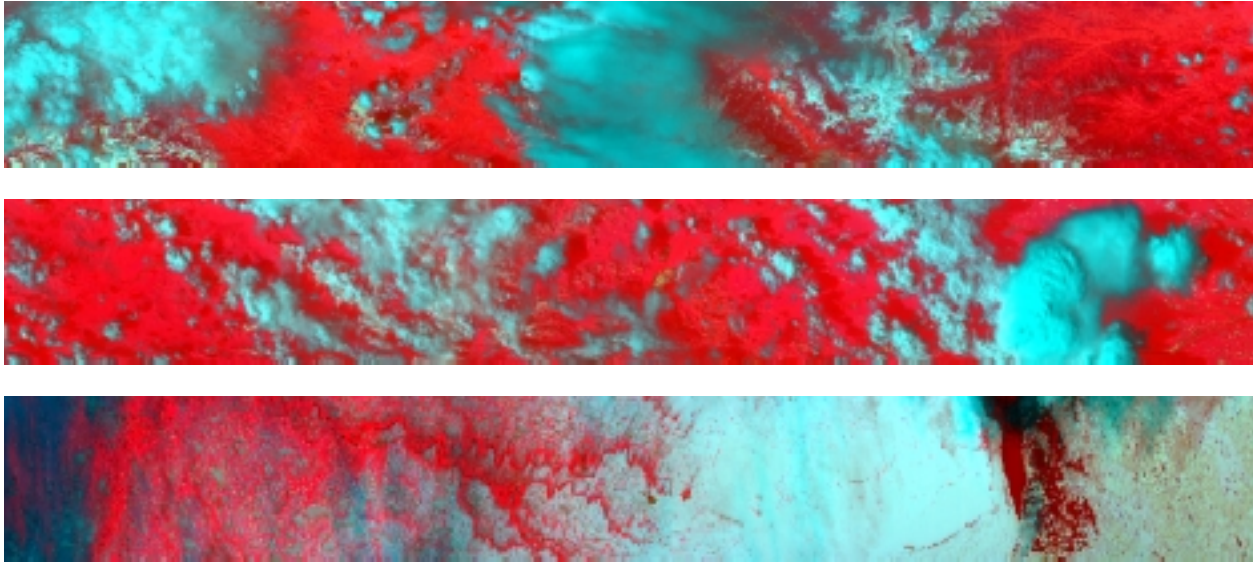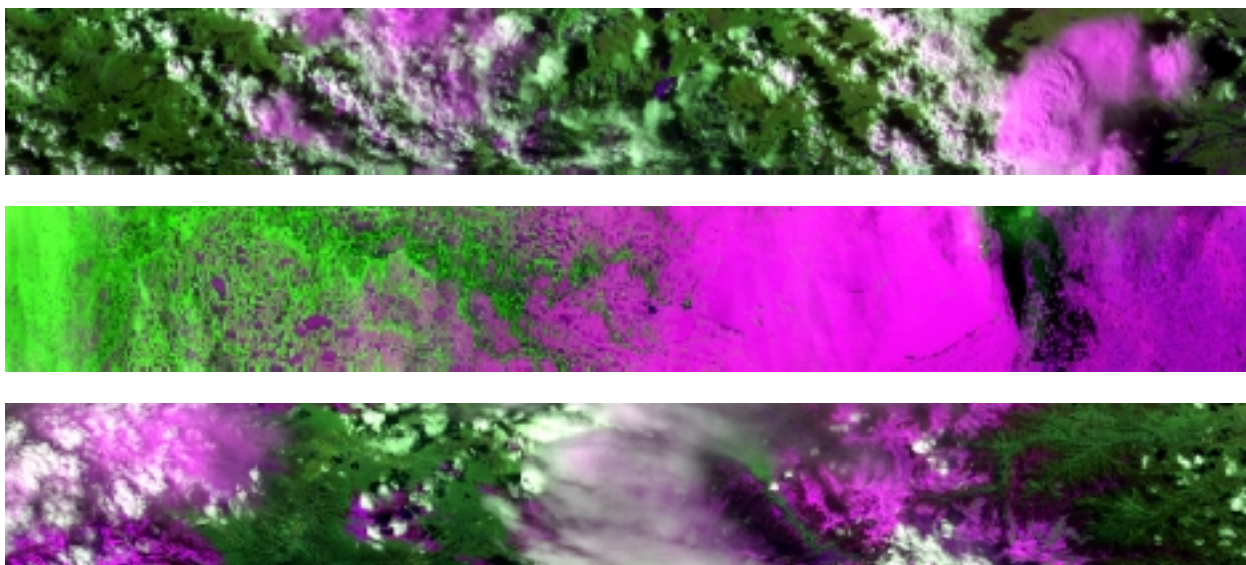
Figure B-11.   RGB (BT8.6, .645, .845)

Using this RGB composite snow/ice surfaces are aqua blue as are clouds, vegetated land is very bright red. Optically thin cirrus over vegetated land and water are purple in coloration. Optically thick cirrus tend to be grayish blue. It is possible to confuse clouds with snow/ice with this combination, caution.

Figure B-12.   RGB (.86, 1.61, .645)

Using this RGB composite snow/ice surfaces are purple, while water clouds are white, vegetated land is green.   Optically thin cirrus over land are green in coloration and tend to blur the underlying surface features. Optically thick ice clouds are purple to gray.
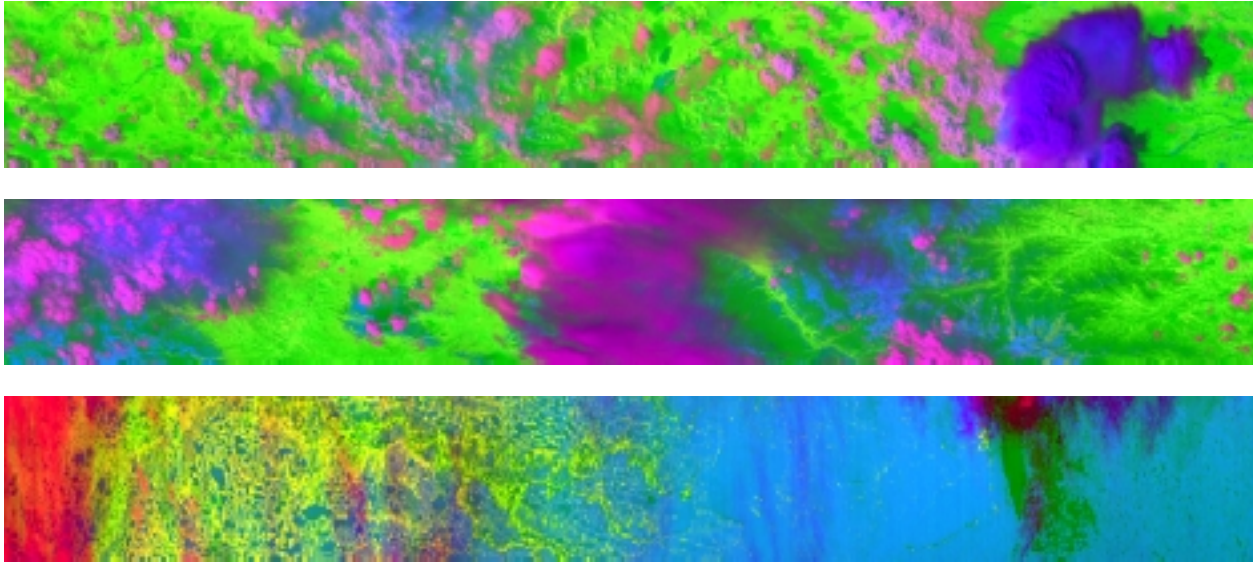
Figure B-13.   RGB (1.61, BT8.6, .645)

Using this RGB composite brings out dramatic differences within a scene. Clouds are purple to dark blue, the bluer the clouds are the more ice that they contain. Cellular structure in thunder clouds is discernable. Thin cirrus may be red in coloration over vegetated land. Snow ice surfaces are light blue, while vegetated land is bright green and sparsely vegetated land is dark green. Snow visible through clouds takes on a darker blue coloration than the clear snowy regions.
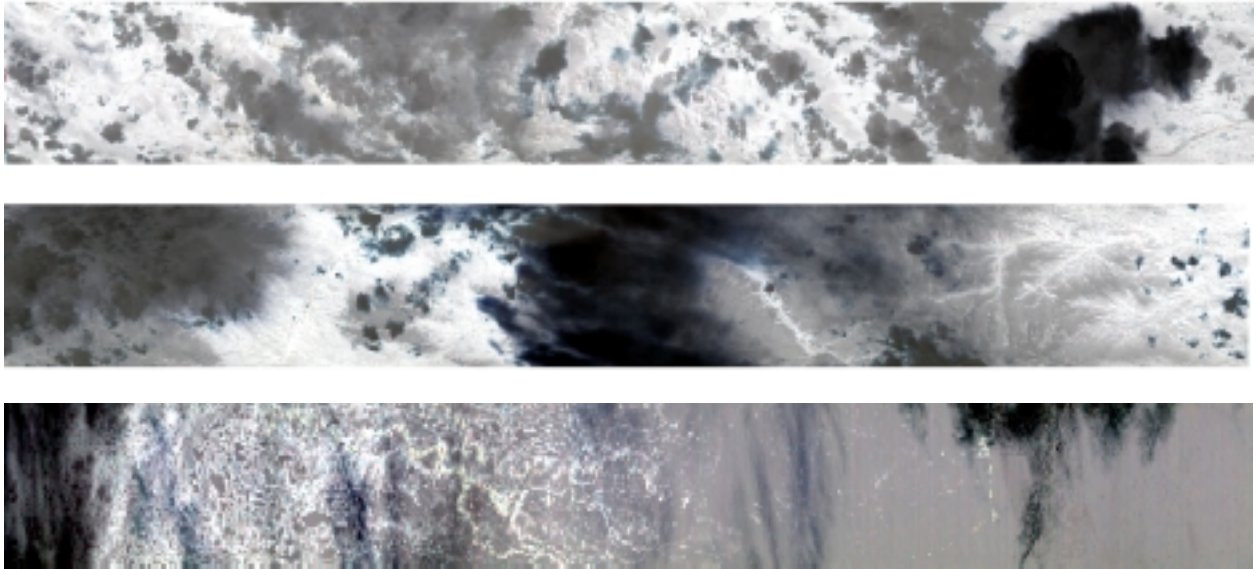
Figure B-14.   RGB (BT12, BT11, BT8.6)

Using this RGB composite generates an image that is almost greyscale at first glance. However, due to the thermal contrast of clouds over underlying surfaces an analyst can notice them. Vegetated land is white in coloration, lower level water clouds are Gray in coloration, higher level cirrus are black in coloration, snow/ice surfaces are Gray in coloration, and optically thin cirrus can have a blue hue to them. The thermal contrast in the middle scene allows one to visually separate out the cellular structure of the thunder cloud.
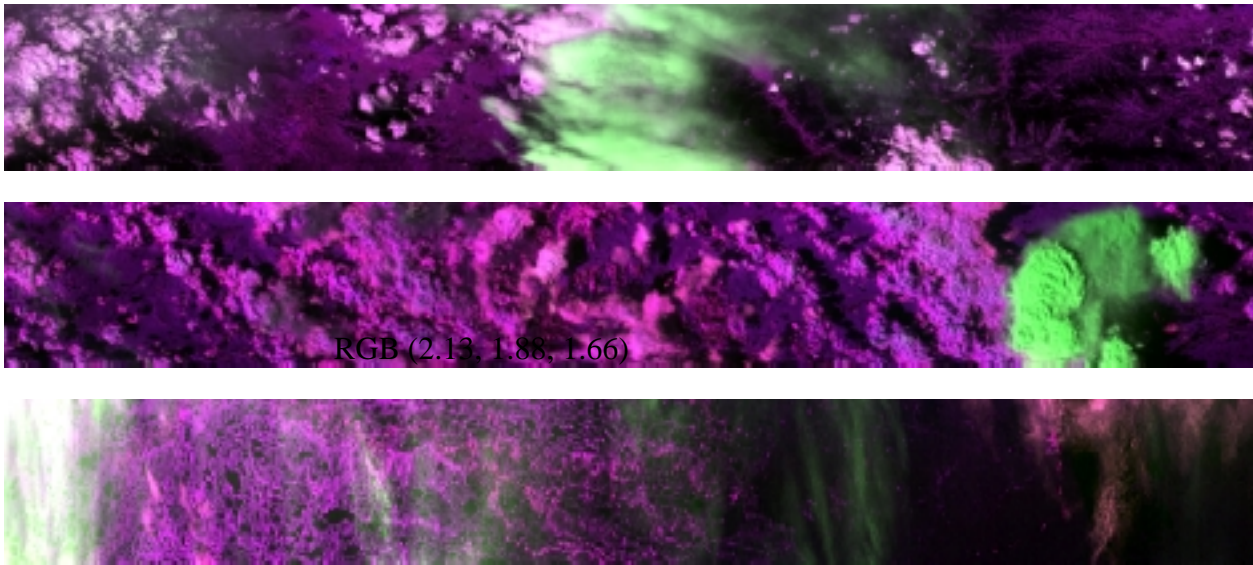
Figure B-15. RGB (2.13, 1.88, 1.66)

Using this near-IR RGB composite snow ice surfaces are black, while vegetated land is black to purple. Lower level water clouds are purple and higher clouds such as cirrus and thunder clouds tend to be from green to white in coloration. The whiter the cirrus is the more optically thin it is. This composite is good to use over an ice covered region to discern clouds from snow/ice and to look for higher cloud presence.
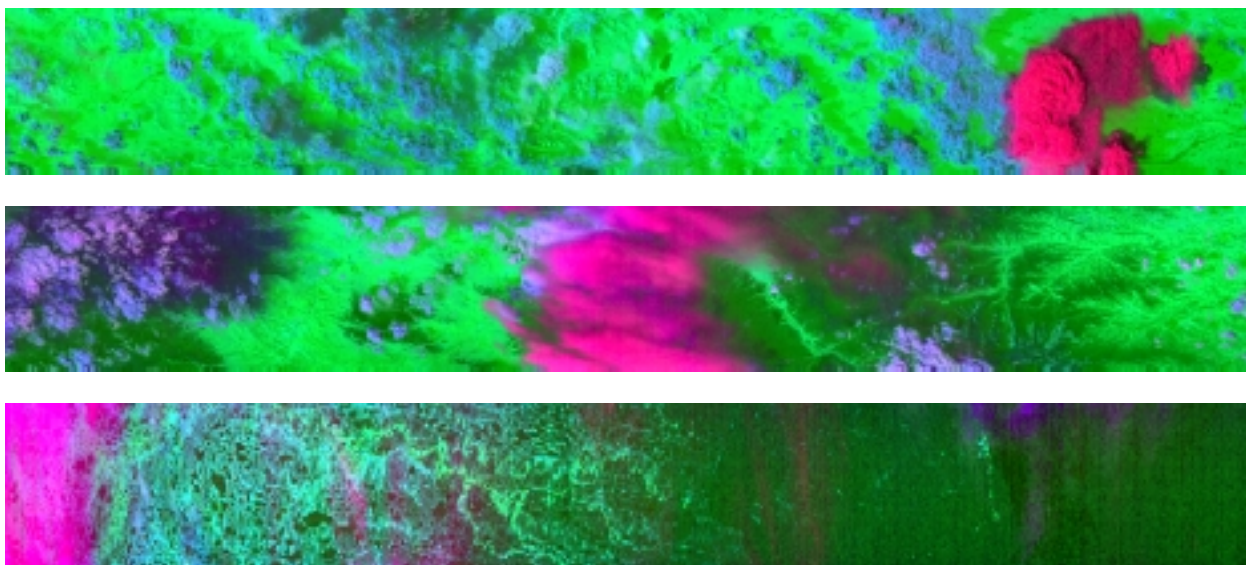
Figure B-16. RGB (1.88, BT4, 1.61)

Using this RGB composite snow/ice surfaces are dark green, lower level water clouds are light blue to dark blue, vegetated land is bright green, with less vegetated being dark green, cirrus over snow and ice is black in coloration, high level cirrus clouds are purple in coloration. Above note the middle thunder cloud scene the cellular structure and edges of this cloud is apparent and the coloration is reddish-purple.
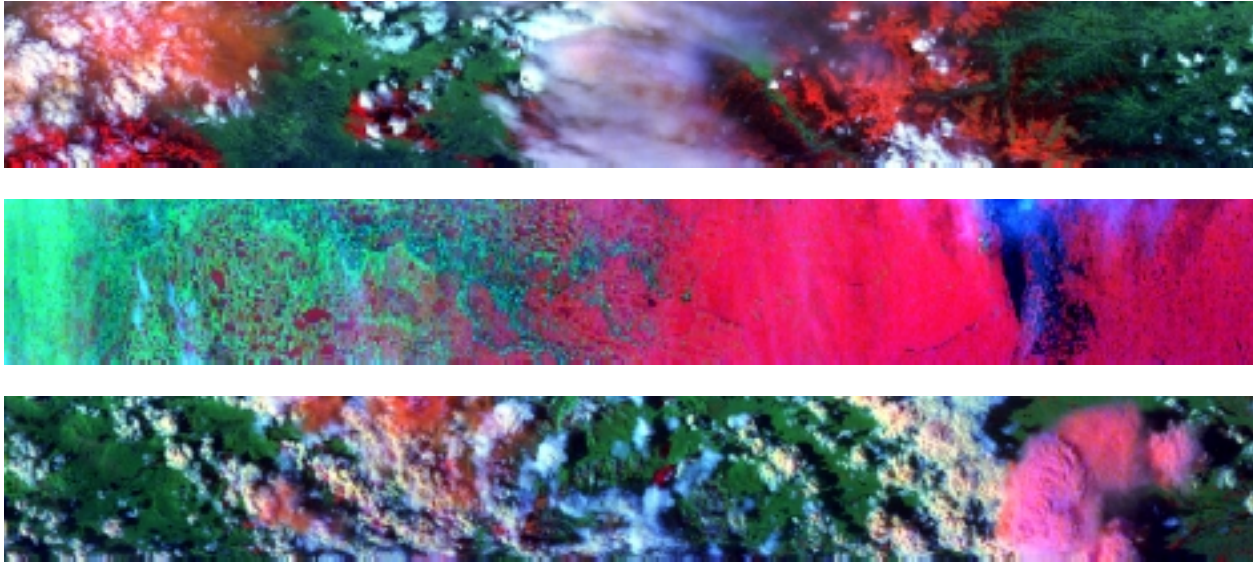
Figure B-17.   RGB (.645, 1.61, BT3.75-BT4.0)

Using this RGB composite snow/ice surfaces are red, low level water clouds are white, vegetated land is green, thin cirrus are red to Gray in coloration, however over some regions they tend to be the same coloration as the underlying surface but blur the surface features. Thin cirrus over water is blue-purple while over snow/ice it is pinkish colored. Thunder clouds tend to be pink in coloration.